



Multiscale modelling of elastic properties of non-bonded single-walled carbon nanotube polymer matrix composites

Author:

Herasati, Saeed

Publication Date:

2014

DOI:

<https://doi.org/10.26190/unsworks/2581>

License:

<https://creativecommons.org/licenses/by-nc-nd/3.0/au/>

Link to license to see what you are allowed to do with this resource.

Downloaded from <http://hdl.handle.net/1959.4/53641> in <https://unsworks.unsw.edu.au> on 2024-05-06

Multiscale Modelling of Elastic Properties of Non-bonded Single-Walled Carbon Nanotube Polymer Matrix Composites

By

Saeed Herasati

A thesis in fulfilment of the requirements for the degree of

Doctor of Philosophy



School of Mechanical and Manufacturing Engineering

Faculty of Engineering

The University of New South Wales

Sydney, Australia

March 2014

COPYRIGHT STATEMENT

‘I hereby grant the University of New South Wales or its agents the right to archive and to make available my thesis or dissertation in whole or part in the University libraries in all forms of media, now or here after known, subject to the provisions of the Copyright Act 1968. I retain all proprietary rights, such as patent rights. I also retain the right to use in future works (such as articles or books) all or part of this thesis or dissertation.

I also authorise University Microfilms to use the 350 word abstract of my thesis in Dissertation Abstract International (this is applicable to doctoral theses only).

I have either used no substantial portions of copyright material in my thesis or I have obtained permission to use copyright material; where permission has not been granted I have applied/will apply for a partial restriction of the digital copy of my thesis or dissertation.’

Signed

Date

AUTHENTICITY STATEMENT

‘I certify that the Library deposit digital copy is a direct equivalent of the final officially approved version of my thesis. No emendation of content has occurred and if there are any minor variations in formatting, they are the result of the conversion to digital format.’

Signed

Date



ORIGINALITY STATEMENT

'I hereby declare that this submission is my own work and to the best of my knowledge it contains no materials previously published or written by another person, or substantial proportions of material which have been accepted for the award of any other degree or diploma at UNSW or any other educational institution, except where due acknowledgement is made in the thesis. Any contribution made to the research by others, with whom I have worked at UNSW or elsewhere, is explicitly acknowledged in the thesis. I also declare that the intellectual content of this thesis is the product of my own work, except to the extent that assistance from others in the project's design and conception or in style, presentation and linguistic expression is acknowledged.'

Signed

Date

Acknowledgements

Foremost, I would like to thank God for blessing me during all of my life especially during my PhD career.

I would like to express my sincere appreciation and deep gratitude to my supervisor, Scientia Professor Liangchi Zhang, for his supports through this exhausting career. Joining his multidisciplinary group of Precision and Nano Processing Technologies (PNPT) has been a great opportunity and a wonderful privilege for me to increase my experiences in all aspects. Liangchi taught me how to do high quality research and helped me to think creatively. I sincerely appreciate his supports in improving my presentation and writing skills. I have been really impressed by his consistency, punctuality and hard work.

I greatly thank my first co-supervisor Dr. Bin Gu for his valuable guidance at the beginning of my PhD. Also, my great gratitude goes to my second co-supervisor Dr. Haihui Ruan. His remarkable insights into engineering and his generous character helped enormously in improving my knowledge.

With gratitude, I would like to acknowledge Kausala Mylvaganam who has been a supportive member of our group and who helped me to understand some basic concepts of atomistic simulations. I would also like to thank Saleh Mostafavi, Alireza Moridi and Asit Kumar for their valuable and friendly assistance and advice. I appreciate the friendship of my fellows in the PNPT group, Mohammad Rahman, Weidong Liu, Weixing Xu, Thai Nguyen, Chuhan Wu, Mei Liu and Dandan Cui, who were generous in sharing their experiences with me.

I would like to acknowledge financial support from the Ministry of Science, Research and Technology (MSRT) of Iran in the form of a scholarship and also the Australian Research Council (ARC) for their support with this project.

With sincere gratitude to my family members especially my mother, mother in law and father in law who have been supportive to me and in memory of my father who has supported me to continue my study at university. Finally, my special great thanks to my wife, Elham, who encouraged me to attend this PhD program. I thank her especially for her understanding, patience and support during this hard milestone. This work is dedicated to Elham and my little daughter, Avin, for their real love.

Saeed Herasati

Sydney, Australia

24 March 2014

Abstract

Extraordinary mechanical properties of single-walled carbon nanotubes (SWCNTs) have attracted great attention and produced a new generation of advanced polymer matrix composites (PMC). Nevertheless, diverse experimental reports on the elastic properties of SWCNT-PMC, have also initiated extensive theoretical investigations aimed at revealing their reinforcement mechanisms and optimizing their mechanical properties.

Due to nano-scale dimension of SWCNTs and interphase in a nano-composite, revealing their geometry and mechanical properties have attracted many research efforts. Atomistic simulation methods have been the most promising tools to expose mechanics of nano-materials. However, many criteria should be satisfied to obtain reliable results. At the beginning of this thesis, the stiffnesses of isolated SWCNTs and polymer matrices are investigated through atomistic simulations. Molecular dynamics (MD) is used for equilibration process and molecular mechanics (MM) is used to extract the stiffnesses of atomistic models. This leads to the conclusion that all elastic quantities of SWCNTs under the van der Waals (vdW) forces increase with the hydrostatic pressure rise, except the transverse Young's modulus which is not monotonic and remains almost constant for a critical SWCNT diameter. The study also confirms that MM can provide acceptable results for polymers only under specific conditions and right modelling.

It has been reported that the overall stiffness of SWCNT-PMC is significantly affected by the interphase and waviness of SWCNTs. Although the impact of a predetermined

interphase on the stiffness of SWCNT-PMC has been studied thoroughly, little is known about the elastic properties of the interphase layer. Moreover, the waviness of SWCNTs has been unrealistically assumed to be regular wave-shaped fibres. To accurately predict the elastic properties of non-bonded SWCNT-PMC, this thesis has developed a comprehensive multiscale numerical strategy to address both interphase and waviness with minimal simplifications. In Stage 1 of multiscale strategy, a cubic nanoscale representative volume element (NRVE) of a polymer matrix with SWCNT is characterized through atomistic simulations. This NRVE model consists of the bulk matrix, the dense interphase matrix and SWCNT under vdW force, represented as equivalent solid fibre (ESF). Individual constituents are characterized with the aid of atomistic simulation, and a three-phase continuum-based finite element (FE) model is developed successfully which, compare to the atomistic NRVE, give rise to a more flexibility in dimension and needs much less computational cost. Two methods are established to extract the elastic properties of ESF from atomistic NRVE and a simple model composed of SWCNT-clusters under hydrostatic pressure with much less computational cost. The study shows that the average density of the dense interphase matrix can be used as a parameter to determine its mechanical properties, and that CNT diameter and internal walls have a negligible effect on the geometry of interphase and equilibrium thickness of the vdW gap. The three-phase model predictions show a good agreement with the atomistic results.

In Stage 2, a new indicator for the waviness is defined and quantified from micrograph images. An efficient algorithm has been established to construct wavy CNTs. Using the results of three-phase model, the NRVE is used as a basic solid element for the wavy fibres

in a cubic micro-scale representative volume element (MRVE) composite. The MRVE is characterized with the aid of a finite element code. The study confirms that the models established produce results consistent with experiments, that CNT's waviness affecting the elastic properties of SWCNT-PMCs significantly but compared to the waviness, alignment of CNTs is a more influential parameter. The study concludes that ignoring the role of dense interphase or vdW gap interphase lead to unrealistic elastic properties. However, due to their opposite effect, ignoring both interphases can reduce the discrepancy, that ignoring the interphase of non-bonded SWCNT-PMC does not alter the longitudinal Young's modulus of aligned SWCNT-PMCs, and that their interphase region of 3D SWCNT-PMC can be ignored if the CNT diameter is (10, 10) or smaller.

Publications

Journal Papers

1. S. Herasati and L.C. Zhang, A new method for characterizing and modeling the waviness and alignment of carbon nanotubes in composites, *Composites Science and Technology*, 2014; 100, 136-142.
2. S. Herasati, H.H. Ruan and L.C. Zhang, A new method for characterizing the interphase regions of carbon nanotube composites, *International Journal of Solids and Structures*, 2014; 51, PP 1781-1791
3. S. Herasati and L.C. Zhang, Elastic properties of single-walled carbon nanotube clusters: Dependence on hydrostatic pressure, *Computational Materials Science*, 2014; 86, PP 93-98
4. S. Herasati, H.H. Ruan and L.C. Zhang, Effect of chain morphology and carbon-nanotube additives on the glass transition temperature of polyethylene, *Journal of nano research*, 2013;23, PP 16-23

Conference Proceedings

1. S. Herasati and L.C. Zhang, Effect of carbon nanotube additions on the mechanical properties of composites, in: *Proceedings of the 8th Australian Congress on Applied Mechanics (ACAM 8)*, Melbourne, Australia, 2015.
2. S. Herasati and L.C. Zhang, The effect of hydrostatic pressure on the elastic properties of single-walled carbon nanotube clusters, in: *Proceedings of the Second International Conference on Advanced Materials, Energy and Environments (ICMEE-13)*, Yokohama, Japan, 2013.
3. S. Herasati, H.H. Ruan and L.C. Zhang, Effect of chain morphology and carbon-nanotube additives on the glass transition temperature of polyethylene, in: *Proceedings of the 15th International Conference on Advanced Materials (AMPT. 2012)*, Wollongong, Australia, 2013.

Table of Contents

MULTISCALE MODELLING OF ELASTIC PROPERTIES OF NON-BONDED SINGLE-WALLED CARBON NANOTUBE POLYMER MATRIX COMPOSITES	I
ACKNOWLEDGEMENTS	I
ABSTRACT	III
PUBLICATIONS	VI
TABLE OF CONTENTS	VII
LIST OF FIGURES	XIII
LIST OF TABLES	XVI
LIST OF SYMBOLS AND ABBREVIATIONS	XVII
CHAPTER 1 INTRODUCTION	1
1.1 OVERVIEW	1
1.2 RESEARCH OBJECTIVES.....	4
1.3 DISSERTATION OUTLINES	4
CHAPTER 2 BACKGROUND AND STATE OF THE ART	8
2.1 INTRODUCTION.....	8
2.2 NANO-MECHANICS OF NANO-COMPOSITES.....	8
2.2.1 <i>Computational chemistry methods</i>	9
2.2.2 <i>Continuum-based atomistic methods</i>	10
2.2.3 <i>Micromechanics for nano-composites</i>	10
2.2.4 <i>Multiscale modelling</i>	11
2.3 ELASTIC MODULI OF CNTS.....	12

2.3.1	<i>Types and geometry of CNTs</i> -----	12
2.3.2	<i>Elastic moduli of free-standing CNTs</i> -----	15
2.3.3	<i>Elastic moduli of CNT-clusters</i> -----	17
2.4	PHYSICAL PROPERTIES OF POLYMERS-----	19
2.5	INTERPHASE OF CNT-COMPOSITES-----	21
2.6	WAVINESS OF CNTs-----	23
2.7	MULTISCALE MODELLING OF CNT-PMCS-----	25
2.8	SUMMARY-----	28
 CHAPTER 3 BASICS OF ATOMISTIC SIMULATION METHODS AND MATERIALS STUDIO --		30
3.1	INTRODUCTION-----	30
3.2	BASIC CONCEPTS-----	31
3.2.1	<i>ab initio quantum mechanics methods</i> -----	31
3.2.2	<i>Molecular dynamics and molecular mechanics</i> -----	32
3.3	COMPASS FORCE FIELD-----	33
3.4	PROGRESS CONTROL-----	34
3.5	ATOMISTIC TEMPERATURE-----	35
3.5.1	<i>Evaluation of temperature</i> -----	35
3.5.2	<i>Controlling temperature</i> -----	37
3.6	ATOMISTIC STRESS AND PRESSURE-----	39
3.6.1	<i>Atomistic stress evaluation</i> -----	39
3.6.2	<i>Pressure/stress control methods</i> -----	40
3.7	PERIODIC BOUNDARY CONDITIONS-----	42
3.8	NON-BONDED SUMMATION METHODS-----	44
3.9	REDUCING MD RUN TIME IN MATERIALS STUDIO-----	45
3.9.1	<i>Accuracy of MD simulation</i> -----	45

3.9.2	<i>Proper time step</i>	48
3.9.3	<i>Cell size</i>	49
CHAPTER 4 ATOMISTIC SIMULATION OF POLYMERS WITH DIFFERENT MORPHOLOGY		
AND ADDITIVES		51
4.1	INTRODUCTION	51
4.2	MODELLING	52
4.2.1	<i>Polyethylene</i>	53
4.2.2	<i>Polyvinyl chloride</i>	56
4.2.3	<i>Polystyrene</i>	56
4.3	ATOMISTIC EQUILIBRATION	57
4.4	STRESS-STRAIN ANALYSIS	59
4.5	RESULTS AND DISCUSSION	62
4.5.1	<i>Density</i>	62
4.5.2	<i>Dilatometric graphs</i>	63
4.5.3	<i>Stress-strain analysis</i>	69
4.6	CONCLUSION	71
CHAPTER 5 ELASTIC PROPERTIES OF FREE-STANDING SWCNTS AND SWCNT-		
CLUSTERS		73
5.1	INTRODUCTION	73
5.2	MODELLING	74
5.2.1	<i>Free-standing SWCNT</i>	74
5.2.2	<i>SWCNT-cluster</i>	75
5.3	ATOMISTIC SIMULATION	77
5.3.1	<i>Collapse pressure of SWCNT-cluster</i>	78

5.3.2	<i>Elastic moduli of SWCNT-clusters</i>	78
5.3.3	<i>Elastic moduli of free-standing SWCNTs</i>	79
5.4	RESULTS AND DISCUSSION	81
5.4.1	<i>Collapse pressure of SWCNTs</i>	81
5.4.2	<i>Elastic moduli of SWCNT-clusters</i>	82
5.4.3	<i>Elastic moduli of free-standing SWCT</i>	90
5.5	CONCLUSIONS	91
CHAPTER 6	ELASTIC PROPERTIES OF NANO-REPRESENTATIVE VOLUME ELEMENT: A THREE-PHASE MODEL	94
6.1	INTRODUCTION	94
6.2	MODELLING	95
6.3	ATOMISTIC SIMULATIONS	96
6.4	DEVELOPMENT OF THREE-PHASE NRVE MODEL	96
6.4.1	<i>Phase 1-ESF</i>	98
6.4.2	<i>Phase 2 - Dense interphase</i>	99
6.4.3	<i>Phase 3-Bulk matrix</i>	101
6.5	RESULTS AND DISCUSSION	102
6.5.1	<i>Stress analysis of atomistic NRVE</i>	102
6.5.2	<i>The properties of ESF and a simplified CNT-cluster approach</i>	103
6.5.3	<i>The interphase</i>	109
6.5.4	<i>The comparison between the three-phase model and MM simulation</i>	111
6.6	CONCLUSIONS	116
CHAPTER 7	CHARACTERIZING AND MODELING THE WAVINESS AND ALLIGNMENT OF CNTS AND THE EFFECT ON THEIR COMPOSITES	118

7.1	INTRODUCTION-----	118
7.2	MODELLING OF WAVY CNTS-----	119
7.3	VALIDATION OF TECHNIQUE WITH EXPERIMENTAL RESULTS-----	122
7.3.1	<i>Data scanning</i> -----	122
7.3.2	<i>Data analysis</i> -----	123
7.3.3	<i>Constructing wavy CNTs</i> -----	124
7.3.4	<i>Accuracy analysis</i> -----	129
7.4	STRESS ANALYSIS USING FE-----	131
7.4.1	<i>Mesh generation</i> -----	131
7.4.2	<i>Local coordinates of CNT-fibre elements</i> -----	132
7.4.3	<i>Stress-strain analysis</i> -----	133
7.5	RESULTS AND DISCUSSION-----	134
7.6	CONCLUSIONS-----	137
CHAPTER 8	THE EFFECT OF INTERPHASE ON THE MACROSCOPIC ELASTIC	
	PROPERTIES OF NON-BONDED SWCNT-PMCS-----	139
8.1	INTRODUCTION-----	139
8.2	MULTISCALE MODELLING-----	140
8.2.1	<i>Elastic properties of S-NVRE</i> -----	142
8.2.2	<i>Elastic properties of MRVE</i> -----	143
8.3	RESULTS AND DISCUSSION-----	145
8.4	CONCLUSION-----	149
CHAPTER 9	CONCLUSION AND FURURE DIRECTIONS-----	152
9.1	CONCLUDING REMARKS-----	152
9.1.1	<i>Characterization of composite constituents (Chapters4 and 5)</i> -----	152

9.1.2	<i>Elastic properties of NRVE (Chapter 6)</i>	153
9.1.3	<i>Waviness of CNTs (Chapter 7)</i>	154
9.1.4	<i>The effect of interphase (Chapter 8)</i>	154
9.2	FUTURE DIRECTIONS	155
9.2.1	<i>The effect of large deformation on the overall elastic properties of SWCNT-PMCs</i>	155
9.2.2	<i>Analytical solution for the elastic properties of ESF</i>	155
9.2.3	<i>The efficiency of MWCNTs vs. SWCNTs</i>	156
9.2.4	<i>Close contact of CNTs</i>	156
REFERENCES		157
APPENDIX		171
APPENDIX 1. STIFFNESS MATRIX		171
APPENDIX 2. ENERGY TERMS OF COMPASS FORCE FIELD		172

List of Figures

Fig. 2.1 Different types of CNTs: (a) SWCNT with open ends, (b) SWCNT with spherical capes, (c) MWCNTs, and (c) CNT clusters.	13
Fig. 2.2 A sample graphene sheet and associated parameters with the chirality of CNTs.	14
Fig. 2.3 Sample CNTs with different chirality and close diameters: (a) armchair SWCNT (10, 10), (b) zigzag SWCNT (17, 0), and (c) chiral SWCNT (15, 5).	15
Fig. 3.1 Maxwell-Boltzmann distribution of water with temperature variation.	37
Fig. 3.2 Front view of a SWCNT-PMC: (a) non-periodic boundary, and (b) periodic boundary.	43
Fig. 3.3 Run time against quality of MD calculation	47
Fig. 3.4 Average cell volume against quality of MD calculation	47
Fig. 3.5 Sample stress-strain graphs of pure PVC for different MM qualities.	48
Fig. 4.1 A typical graph of polymer strength as a function of molecular weight	53
Fig. 4.2 Polyethylene and its composite schemes: a) fully amorphous PE, b) semi-crystalline with linear amorphous PE chains, c) semi-crystalline with branched amorphous, d) a composite with short-capped CNTs and linear PE chains, and e) a composite with infinitely-long CNTs and linear PE chains. Hydrogen atoms are shown in green and carbon atoms are dark gray or purple.	55
Fig. 4.3 Fully amorphous polymers: (a) polyvinyl chloride scheme, and (b) polystyrene scheme.	56
Fig. 4.4 Specific volume change of amorphous PE with $n=400$ against time in the equilibration process.	59
Fig. 4.5 Sample stress-strain relation of pure PVC (<i>Scheme 2</i>) in two cycles.	62
Fig. 4.6 Specific volume change of amorphous and semi-crystalline PE with temperature.	64
Fig. 4.7 Specific volume against temperature change. a) Short-capped CNT-composite b) Infinite CNT-composite.	66
Fig. 4.8 Specific volume changes of different schemes.	66
Fig. 4.9 Unidirectional morphology of PE around CNT.	67
Fig. 4.10 Specific volume against temperature change of amorphous PVC.	68
Fig. 4.11 Specific volume against temperature change of amorphous PS.	68
Fig. 5.1 Free-standing SWCNT scheme.	75
Fig. 5.2 The concept of an SWCNT-cluster: (a) the SEM image of some SWCNT-clusters [110], and (b) an SWCNT-cluster scheme in a periodic cell, involving image atoms out of cell.	76

Fig. 5.3 Collapse pressure of some SWCNT-clusters: (a) variation of the normalized cell volume with pressure, and (b) variation of the collapse pressure with SWCNT diameter.	81
Fig. 5.4 Variation of elastic properties with the external pressure applied when the SWCNT diameter changes: (a) longitudinal Young's modulus, and (b) transverse Young's modulus.	83
Fig. 5.5 (a) Longitudinal Young's modulus, E_{zz} , at the absolute zero pressure compared with the results of Lu [74], Popov <i>et al.</i> [118] and Liu <i>et al.</i> [119], and ΔE_{zz} at 2000 MPa when the SWCNT diameter varies, and (b) ΔE_{zz} as a function of pressure.	83
Fig. 5.6 (a) Variation of the transverse Young's modulus, E_{xx-0} and $\Delta E_{xx-2000}$, and (b) ΔE_{xx} as a function of pressure.	84
Fig. 5.7 Variation of normalized vdW and bond portions of strain energy with pressure.	87
Fig. 5.8 (a) Out-of-plane Poisson's ratio, ν_{xy} , and (b) $\Delta \nu_{xy}$ as a function of pressure.	88
Fig. 5.9 (a) Variation of the in-plane Poisson's ratio, ν_{zx} with SWCNT diameter, and (b) $\Delta \nu_{zx}$ as a function of pressure.	89
Fig. 5.10 (a) Variation of out-of-plane shear modulus, G_{zx} , and (b) ΔG_{zx} as a function of pressure.	90
Fig. 6.1 CNT-PVC composite schemes, (a) the SWCNT-PVC composite, and (b) the MWCNT-PVC composite, where the dark gray balls represent carbon atoms, the green ones indicate chlorine atoms, and the white ones stand for hydrogen atoms.	95
Fig. 6.2 The three-phase NRVE model, phase 1- ESF, phase 2- dense interphase, phase 3- bulk matrix.	97
Fig. 6.3 Strain state on the SWCNT-PVC scheme, (a) tensile, and (b) pure shear strain.	99
Fig. 6.4 (a) Concentric cylinders to explore the local density of the matrix, and (b) the variation of the local density in the matrix with the radial thickness of the matrix.	100
Fig. 6.5 The SWCNT-cluster model in a periodic cell involving some image atoms out of cell.	104
Fig. 6.6 The elastic constants of (5, 5) SWCNT-cluster normalized by those of ESF from the (5, 5) SWCNT-PVC scheme.	106
Fig. 6.7 Variation of the proper external pressures on SWCNT-clusters with SWCNT diameter.	106
Fig. 6.8 Elastic constants of PVC against density: (a) Young's modulus, and (b) Poisson's ratio.	110
Fig. 6.9 Two FE models: (a) three-phase model, and (b) two-phase model.	112
Fig. 7.1 The schematic diagram of the random walking chains.	119
Fig. 7.2 The algorithm flowchart for generating endpoints of segments of wavy cords in a cubic RVE.	121
Fig. 7.3 Waviness characterization of the CNTs with a diameter of 30 nm, (a) original image, and (b) selected datapoints.	123
Fig. 7.4 Histogram of the deflection angle from the scanned data.	124

Fig. 7.5 The 1D-Scheme samples including aligned CNTs with the CNT volume fraction of 0.5 and waviness angles of (a) $\theta_{\max}=0^\circ$, (b) $\theta_{\max}=25^\circ$, and (c) $\theta_{\max}=55^\circ$	125
Fig. 7.6 Local RVE defined to generate 1D-Scheme samples.	125
Fig. 7.7 Front and top views of the 2D-Scheme samples with the CNT volume fraction of 0.5 and waviness angles of (a) $\theta_{\max}=0^\circ$, (b) $\theta_{\max}=25^\circ$, and (c) $\theta_{\max}=55^\circ$	126
Fig. 7.8 The 3D-Scheme samples with the CNT volume fraction of 0.5 and waviness angles of (a) $\theta_{\max}=0^\circ$, (b) $\theta_{\max}=25^\circ$, and (c) $\theta_{\max}=55^\circ$	127
Fig. 7.9 (a) An algorithm-generated cubic RVE with the CNT volume fraction of 1%, θ_{\max} of 25° and side length of $5\ \mu\text{m}$, and (b) the top view of a thin layer from the upper region of the RVE.....	128
Fig. 7.10 Histogram of θ of the long CNT segments from Fig. 7.9b.	128
Fig. 7.11 A comparison of an algorithm-generated 2D-Scheme sample with the experimentally observed CNT distribution (CNT volume fraction = 0.5% and $\theta_{\max}=25^\circ$). (a) the algorithm-generated RVE, and (b) the TEM image [9].	129
Fig. 7.12 Distribution of the algorithm-generated angles of a 3D-Scheme sample with $\theta_{\max}=25^\circ$. (a) histogram of θ , (b) normal probability of θ , and (c) histogram of ψ	130
Fig. 7.13 Sample mesh generation of (a) 3D distribution of CNTs, and (b) matrix.	132
Fig. 7.14 The local coordinate system of each element is oriented to be tangent to the neutral axis of a CNT-fibre.....	133
Fig. 7.15 The relative Young's moduli of the composite to the matrix with different waviness angles (θ_{\max}) (volume fraction = 0.5%; 2D-Scheme).....	135
Fig. 7.16 Effect of CNT-alignment on the variation of E_C/E_M with the CNT waviness angle.	136
Fig. 8.1 A schematic diagram of the multiscale modelling strategy for characterizing SWCNT-PMCs from the atomistic scale NRVE to the micro-scale MRVE. The MRVE is ready to be used for an efficient FE analysis but with all the atomistic and interphase effects counted.....	141
Fig. 8.2 1D and 3D-Schemes of SWCNT-PMCs with a volume fraction of 0.5% and waviness angles of (a) $\theta_{\max}=0^\circ$, (b) $\theta_{\max}=30^\circ$, and (c) $\theta_{\max}=50^\circ$	145
Fig. 8.3 The Young's moduli of CNT-PMCs, E_c , normalised by that of the PVC matrix, E_M , (a) with SWCNT(10,10), and (b) with a variety of SWCNTs from SWCNT (5, 5) to (15, 15) under a given $\theta_{\max}=30^\circ$. The SWCNT volume fraction is 0.5%.	147
Fig. 8.4 The relative Young's modulus of the composite with aligned SWCNTs. (a) using SWCNT(10,10) but varying θ_{\max} , and (b) using $\theta_{\max}=30^\circ$ but varying SWCNT diameters.	148
Fig. 8.5 Variation of the relative transverse Young's modulus of composites with aligned SWCNTs. (a) with SWCNT (10, 10), and (b) with the change of SWCNT diameters.....	149

List of Tables

Table 2.1 The initial and normalized longitudinal Young's modulus and wall thickness of CNTs	17
Table 3.1 Accuracy of different parameters under four quality settings	46
Table 4.1 Physical parameters, obtained from atomistic simulations and compared to experimental results ..	70
Table 5.1 Five elastic properties of free-standing SWCNT as a solid cylinder.....	91
Table 6.1 Elastic constants of (5, 5) SWCNT-PVC evaluated from Eq. 6.1 and Eq. 6.2.....	103
Table 6.2 Five elastic constants, (A) ESF with PVC-SWCNT composite, (B) ESF with SWCNT-cluster scheme, and (C) free-standing SWCNT as a solid cylinder.....	108
Table 6.3 Variation of the dense interphase density with SWCNT dimension.	109
Table 6.4 Molecular mechanics and FE results for elastic constants of different NRVEs.....	114
Table 7.1 Definitions of the algorithm parameters.....	120
Table 8.1 Elastic properties of transversely isotropic 3P-NRVEs containing SWCNTs of different diameters	143

List of Symbols and Abbreviations

CNT	carbon nanotube
SWCNT	single walled carbon nanotube
MWCNT	multi walled carbon nanotube
R_{CNT}	radius of CNT
vdW	van der Waals
QM	quantum mechanics
CG	coarse-grained
MD	molecular dynamics
MM	molecular mechanics
PMC	polymer matrix composite
ESF	equivalent solid fiber
MRVE	micro representative volume element
NRVE	nano representative volume element
FE	finite element
COMPASS	Condensed-phase Optimized Molecular Potentials for Atomistic Simulation Studies
PS	polystyrene
PE	polyethylene
PVC	polyvinyl chloride
TEM	transmission electron microscope
SEM	scanning electron microscope
PBC	periodic boundary condition
ρ	density
ν	Poisson's ratio
ε	strain
σ	stress
C_{ij}	stiffness matrix components
E_{ij}	Young's moduli components
G_{ij}	Shear moduli components
N	number of atoms
T	temperature
P	pressure
V	volume
NPT	ensemble of constant N, P and T

NVT	ensemble of constant N, V and T
T_g	glass transition temperature
α_v	volumetric coefficients of thermal expansions
α_L	linear coefficients of thermal expansions
h	vdW gap distance
ρ_i	density of the dense interphase
ρ_o	bulk PVC

Chapter 1

Chapter 1

Introduction

1.1 Overview

During recent decades, an extensive research effort has been made to develop high performance lightweight polymers for a wide range of applications such as spaceships, vehicles and buildings. However, compared to metal alloys, polymers have modest mechanical properties [1] which confine them to low risk applications.

For many years polymers have been composed of high performance microfibres, such as glass and carbon fibres, to improve their mechanical properties [2]. Alternatively, due to their superior mechanical properties, many novel nano-materials such as nano-fibres, CNT and graphene have been used as the reinforcement in a wide range of nano-composites. Among nano-materials, CNTs [3] are well known due to their high strength (greater than steel), great stiffness (double that of tungsten), small density (lighter than aluminium), and high conductivity (greater than copper) [4].

Due to the great intrinsic properties of CNTs, their high specific surface area [5] and high aspect ratio of length to diameter, theoretically, a few percentages of CNT additives are expected to enhance elastic properties of materials significantly. However, the experimental conclusions in the published literature are diverse [5, 6]. Some investigations confirm a great improvement (e.g., [6-11]), but some others reported that CNT additives could even downgrade the mechanical properties of the matrix (e.g., [11, 12]), which in turn have

attracted more extensive research efforts to understand the interaction mechanisms between CNTs and the matrix and to improve the CNT-PMCs properties.

The elastic properties of CNT-PMCs have been the subject of many experimental [7, 13-16] and theoretical [17-19] studies over the past two decades. It has been found that the overall elastic moduli of CNT-PMCs are affected by many factors such as CNT waviness [20, 21], dispersion [22, 23], functionalization [24-26], vdW interaction [27] and CNT-matrix interphase [28, 29]. To clarify these issues, experimental means, such as the examination and analysis by transmission electron microscopy [16] and macroscopic mechanical testing [15] have frequently been used. However, the experimental methods can only evaluate the performance of a CNT-PMC [7, 13, 15] after its fabrication, rather than reveal the mechanisms of reinforcement or provide a way to optimize the mechanical properties. Therefore, theoretical means are necessary to shed light on the unknown parameters.

The prominent classic continuum approaches of micromechanics [30] have been used extensively to predict elastic properties of CNT-PMCs. However, these approaches are still based on the continuum assumption, which cannot vividly capture the interactions between the CNTs and the matrix. The most controversial issues associated with the continuum methods are the properties and geometry of the nano-inclusions and the interphase regions, which cannot be properly accommodated or approximated by the micromechanics or the FE treatments directly.

Atomistic simulation methods have been used most frequently to explore the detailed reinforcing mechanisms of CNT-PMCs, such as the effects of CNT-matrix interphase [31], the bonding and functionalization [19, 24, 32-34], and the stress-strain properties of nanoscale molecular mechanisms [19, 35-39]. However, due to the high computational cost, the atomistic methods are confined to small models of only a few nanometers. The time scale is also limited to some nano-seconds. As a result, such modelling is incapable of predicting the macroscopic properties of a CNT-PMC. The most appropriate solution is to define a small NRVE containing the matrix and the reinforcement. The NRVE concept takes into account all the controversial issues associated with CNT-matrix interactions. Meanwhile it is small enough to be analyzed by atomistic simulations. In a multiscale strategy, the NRVE can be implemented in a continuum-based MRVE which due to the tiny scale of SWCNTs is sufficient to obtain the macroscopic properties of their composites. The most important concerns with the micro-scale analysis are waviness and agglomeration of CNTs [40]. Although, extensive multiscale models for CNT-PMCs have been developed (e.g. Ref. [41-43]), there still remains an uncertainty at both nano- and micro-scale.

This dissertation addresses the significant question of how to predict the elastic properties of non-bonded SWCNT composites accurately with minimum simplifications. To this end, the constituents and the interphase of the composite are characterized individually by the aid of atomistic simulation and are integrated in a continuum NRVE. Furthermore, a novel algorithm and technique are proposed for characterizing and modelling of the waviness of CNTs at micro-scale. The nano- and micro-scale models are then integrated as a

comprehensive numerical multiscale method. The effect of interphase, waviness and alignment of SWCNTs on the overall elastic properties of their composites are then studied.

1.2 Research objectives

The main objective of this thesis is to develop a numerical multiscale method to predict elastic properties of non-bonded SWCNT-PMCs with an affordable computational strategy and a satisfactory accuracy. The detailed aims of this thesis are:

- Understanding the criteria for an atomistic simulation to give acceptable results for pure polymers
- Characterizing the elastic properties of pure polymer, free-standing SWCNTs and SWCNT-clusters under a variety of conditions
- Characterizing the elastic properties of NRVEs at nanoscale and obtaining the geometry and properties of their interphase
- Developing a method for characterizing the macroscopic properties of SWCNT-PMCs in a multiscale process and studying the impact of the interphase on their overall elastic properties

1.3 Dissertation outlines

The structure of this thesis is outlined in eight chapters include the current introduction *Chapter 1*.

Chapter 2, consisting of seven major sections, provides a sufficient background and review on the most important subjects related to this thesis. Appropriated nano-mechanics tools to predict the elastic properties of CNT-PMCs are discussed. The numerical studies are considered more specifically and their challenges are addressed. The studies on the constituents of CNT-PMCs and two important factors of interphase and waviness are reviewed and the gaps are highlighted. Eventually, the necessity and the challenges of multi-scale modelling of CNT-PMCs are explained.

Chapter 3 includes the basics of atomistic simulations. Although the atomistic simulation is relatively new for engineering applications, sufficient background on molecular dynamic (MD) and molecular mechanic (MM) techniques is provided and the associated energy terms relating to the potential Condensed-phase Optimized Molecular Potentials for Atomistic Simulation Studies (COMPASS) force field are explained for the subsequent discussion. methods by which the Materials Studio software can evaluate and control the temperature and the stress of atomistic models will be explained. At the end, the parameters of Materials Studio are properly justified and the methods to minimize the run time with adequate accuracy are considered.

In *Chapter 4* the challenges associated with modelling, equilibration and stress-strain analysis of polymers with the aid of atomistic simulations are studied. Important physical parameters such as density, glass transition and elastic properties of a few commercial thermoplastic polymers are studied to examine the proposed procedure and to discuss the conditions under which atomistic simulations bring about acceptable results. Furthermore, by the aid of MD, the effect of structural morphology of polymer and the influence of

SWCNT additives on the thermal behaviour of polyethylene (PE) are studied through dilatometric graphs.

Chapter 5 is focused on the elastic properties of free-standing SWCNTs and their clusters. The effect of hydrostatic pressure on the elastic properties of SWCNT-clusters is studied with MM simulations.

Chapter 6 characterizes the fundamental element for the multiscale strategy. Molecular structure of a cubic NRVE, including SWCNT and the surrounding matrix, is constructed and equilibrated by the aid of MD, then characterized with the aid of MM simulation. The interphase is characterized and an equivalent-continuum-based three-phase FE scheme is developed and examined.

Chapter 7 is focused on the waviness of CNTs. A method is proposed for characterizing and modelling wavy CNTs. The method is validated with experimental results.

In *Chapter 8* the methods that were developed in Chapter 6 and Chapter 7 are integrated in a multiscale modelling to study the effect of interphase, waviness and alignment of SWCNT on the macroscopic elastic properties of non-bonded SWCNT-PMCs.

Chapter 9 summarizes main conclusions and provides the future directions for this research.

Chapter 2

Chapter 2

Background and state of the art

2.1 Introduction

This research aims to develop a computational method to predict elastic properties of polymer non-bonded SWCNT-PMCs. Due to the nano-scale diameter of SWCNTs, special tools and methods are necessary to analyze their composites. In this chapter, a sufficient background on the available methods and tools relevant to this study is provided. A literature review on the characterization of CNT-PMCs and their constituents is also provided to highlight the research gaps to be filled in this thesis. However, it is obvious that a comprehensive review is beyond the capacity of this thesis and only the most important areas relative to this study have been reflected.

2.2 Nano-mechanics of nano-composites

During the last two centuries, extensive continuum-based models have been developed for analyzing the mechanical behaviour of materials assuming a continuous mass instead of discrete atoms. This assumption provided a great opportunity for mathematicians and engineers to develop highly accurate models for macro-scale materials. However, recent development of nanoscale materials which deal with atomic-scale nano-structures such as nano-particles, nano-rods and CNTs, give rise to new problems beyond the capacity of classic continuum mechanics. Therefore, during last two decades much research has been done to extend the classic continuum mechanics for nano-materials. To this end, statistical

mechanics, material science, solid-state physics and quantum chemistry have been employed to establish a new branch of science, called nano-mechanics [44, 45].

2.2.1 Computational chemistry methods

A variety of computational chemistry methods such as *ab initio* quantum mechanics (QM), MD, MM and coarse-grained (CG) methods have been developed to predict mechanical properties of nano-materials. Among them, QM is the most accurate method which is based on the solving the quantum-mechanical equations of Schrodinger for motion of individual atoms [46]. As a rule of thumb, method that is more accurate computationally is more expensive. Furthermore, the accuracy of QM is not necessary to extract the bulk properties of materials. In fact the bulk properties of materials are affected by the statistical location of atomic nuclei and the details of electronic motion are vanished in the averaging the statistical results [47]. QM is the most appropriate method to discuss problems such as developing new atomic force fields [48] and bond formation [49] for a small number of atoms. More appropriate approaches for characterizing mechanical properties of materials are MD, MM and CG methods. Although the CG method is much less time consuming than the MD method [50], due to low accuracy, is not able to provide detailed interaction of molecules and atoms, and is not suitable for atomistic stress-strain analysis. A sufficient background about computational chemistry methods will be provided in the next chapter.

2.2.2 Continuum-based atomistic methods

It is beyond the scope of continuum mechanics to deal with nanoscale materials that are made of a finite number of discrete particles. To gain remarkable features of continuum mechanics, atomistic continuum methods have been developed by substituting atomic interactions with equivalent-continuum elements such as rods, beams, trusses, shell and plates. The properties of each continuum element could be extracted from MM relations. The elements are then integrated and characterized analytically (e.g. Ref. [51]) or numerically with FE software (e.g. Ref. [52, 53]). For example, Shokrieh and Rafiee [52] developed an FE model of CNT-PMC with the carbon-carbon bonds represented by beam elements, and the vdW interactions between the CNT atoms and adjacent matrix by nonlinear springs. Tadmor *et al.*[54] introduced a quasi-continuum method using the classical Cauchy–Born rule for crystal lattice of materials. Odegard *et al.* [55] developed an equivalent continuum method to link the solid mechanics and the computational chemistry by replacing discrete molecular structures with equivalent-continuum models. To this end the potential energy of a molecular system equating with the strain energy of an equivalent solid continuum system the elastic properties of the system. However, some key parameters and the way to demarcate different regions cannot be properly accounted for by the micromechanics or the FE treatments directly.

2.2.3 Micromechanics for nano-composites

The continuum micromechanics are the most famous bridge method from micro to macro-scale. Micromechanics models have been developed for micro-scale inclusion-composites

which have been explained thoroughly by Nemat Nasser and Hori [30]. Micromechanics has been used extensively for CNT-PMCs [30]. However, these approaches are still based on the continuum assumption, which cannot vividly capture the interactions between the CNTs and the matrix. Moreover, it is also beyond the capacity of the classic micromechanics to grasp certain important behaviours of nano-inclusions such as vdW bonding and interphase region between the CNTs and the matrix. However, to improve the applicability of micromechanics, significant efforts have been made to develop the interphase modelling techniques, such as the thin shell interphase treatment [29, 56, 57]. Although, the properties of the transient regions in the treatment still need the application of other methods such as MD and MM analyses [58]. At the same time, some strong assumptions and simplifications must be used to make the micromechanics applicable.

2.2.4 Multiscale modelling

An objective of computational material science is to predict mechanical properties of materials on a wide range of length scales from atomic to macroscopic. Selecting the proper tool for modelling a material depends on the scale of the material and the physical parameter under study. QM is more accurate than MD and also MD is more accurate than CG. However, a more accurate method needs longer calculation time. For example, QM has been used to predict the formation of likely chemical bonding between a few atoms [26] with many details that are not feasible in MD simulations. In the case of atomistic stress-strain analysis, such details of QM vanished, meanwhile, MD can give sufficient accuracy with much less computational cost.

As a practical solution for the problem above, multiscale modelling methods have been introduced and extensively developed [59] in which an accurate technique for nano-scale is integrated with a quick response method for macroscopic scale [60, 61]. For example, Odegard *et al.* [58] proposed an equivalent-continuum approach in which MD was used to obtain equilibrium structure of atomistic model of a CNT-PMC fibre. They used MM relations to calculate the properties of an equivalent continuum fibre applicable for macroscopic analysis with the aid of micromechanics. More reviews on the multiscale analysis of CNT-PMCs are discussed in Section 2.7.

2.3 Elastic moduli of CNTs

After the discovery of CNTs by Iijima [3], an extensive research effort has been made to characterize their mechanical properties. In this section, different types of CNTs are introduced and the studies on their characterization are reviewed.

2.3.1 Types and geometry of CNTs

Carbon nanotubes are nanoscale structures with hollow cylindrical shape. Their shell is constructed of a single-atom thin wall which theoretically rolled up from graphene sheet [62]. The simplest structure of CNTs, called SWCNT, includes one single shell with and without hemispherical capes at the ends as shown in Fig. 2.1.

Carbon nanotubes might be synthesized as multi concentric tubes separated with non-bonded vdW interactions (Fig. 2.1c), called multi-walled CNT (MWCNT). Due to vdW

interaction, CNTs lean to hold together and align as clusters within vdW equilibrium distance (Fig. 2.1d), called CNT-cluster hereafter.

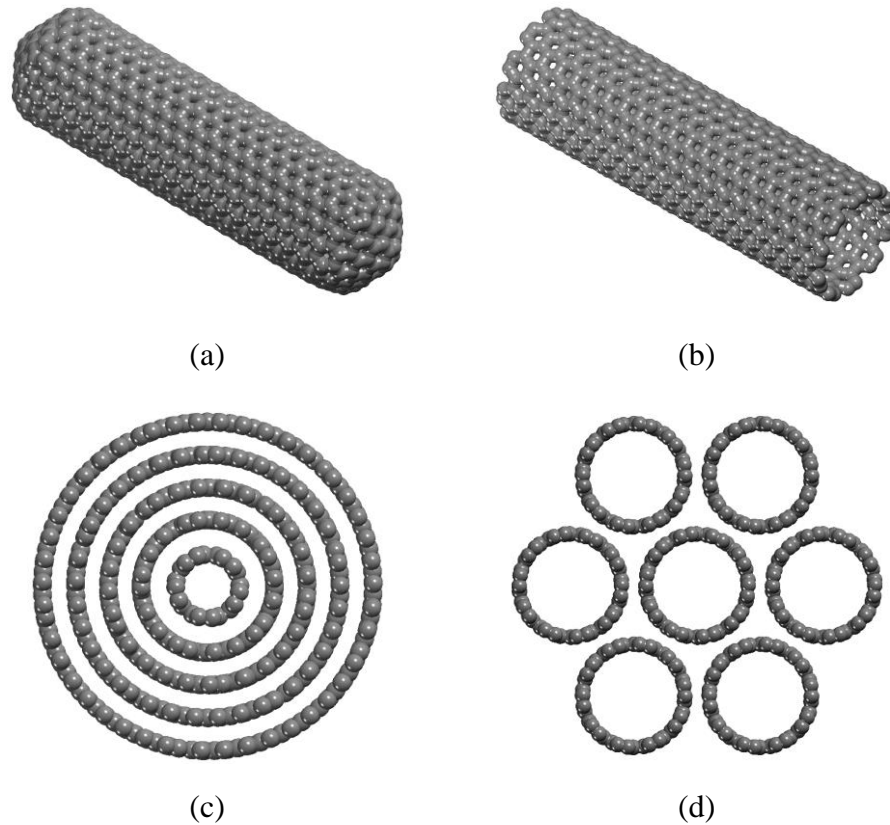


Fig. 2.1 Different types of CNTs: (a) SWCNT with open ends, (b) SWCNT with spherical caps, (c) MWCNTs, and (d) CNT clusters.

Since CNTs are theoretically rolled up from graphene sheet [62], their structure depends on the rolling direction of graphene sheets. If the graphene sheet in Fig. 2.2 is cut through two arbitrary dashed lines and rolled up around tube axis line such that the points A and B are connected, then a CNT (n, m) is formed. The chiral vector is represented by $C_h = n a_1 + m a_2$ in which a_1 and a_2 are unit vectors of graphene as shown in Fig. 2.2. The angle of rolling called chiral angle (θ_{ch}) which is an effective parameter on the physical properties of CNTs

[63-69]. If $m=0$ (i.e. $\theta_{ch}=0$) then the constructed CNT is a zigzag type with the green line chiral vector in Fig. 2.2. If $m=n$ (i.e. $\theta_{ch}=30^\circ$) then an armchair type CNT with the red line chiral vector is formed.

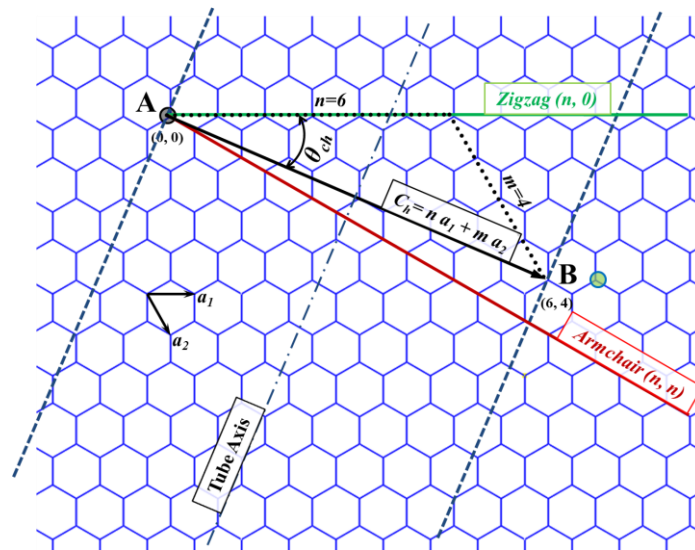
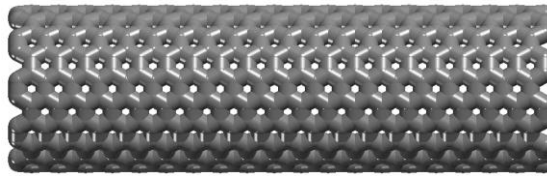


Fig. 2.2 A sample graphene sheet and associated parameters with the chirality of CNTs.

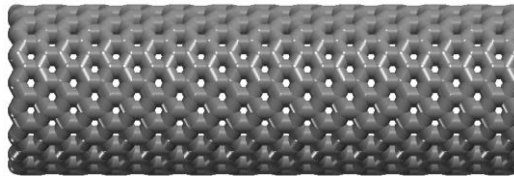
Theoretically, infinite types of CNTs can be constructed. For example, a sample chiral vector for CNT (6, 4) is shown in Fig. 2.2 which is an addition of two vector components of $n=6$ in a_1 direction and $m=4$ in a_2 direction. Three sample CNTs with different chirality and approximately the same diameter are shown in Fig. 2.3.

Due to the tiny size of CNTs, their geometric parameters such as diameter and thickness have been controversial issues that are still open matters for research [70, 71]. There are diverse reports about the wall thickness of CNTs (e.g., Ref. [70-72]) which are mainly due to their thin single-atom wall. In fact, each atom is surrounded with a cloud of electrons which bring about uncertainties [73]. Extensive studies assumed a wall thickness of 3.4 \AA for CNTs which is equivalent to the distance between graphite sheets [74-77]. However,

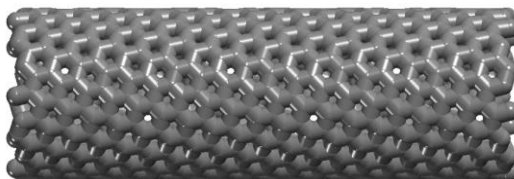
other studies reported much smaller thickness [70, 78-83]. For example, Wang and Zhang [72] studied the different choices of the CNT thickness in literature and concluded that the most appropriate one is 0.617 \AA [70]. Nevertheless, for the composite applications, CNTs can be treated as a solid cylinder with anisotropic properties [31] without concern about their wall thickness.



(a)



(b)



(c)

Fig. 2.3 Sample CNTs with different chirality and close diameters: (a) armchair SWCNT (10, 10), (b) zigzag SWCNT (17, 0), and (c) chiral SWCNT (15, 5).

2.3.2 Elastic moduli of free-standing CNTs

Carbon nanotubes have been treated as isotropic fibres in a composite (e.g. [84, 85]). However, it has been shown that CNTs are transversely isotropic materials with five

independent elastic parameters [86-88]. The longitudinal Young's modulus of CNTs has been measured experimentally through studying the amplitude of thermal vibration of CNTs by the aid of transmission electron microscope (TEM) [89, 90]. Furthermore, simple tensile tests [91-93] and bending tests [94-96] manipulated using the tip of an atomic-force microscope bring about extremely diverse results between 0.4 to 4.15 TPa [97]. Experimental methods have their limitations and yet, are not able to characterize all elastic parameters of CNTs such as transverse Young's modulus, Poisson's ratio and shear moduli which in turn has encouraged researchers to expand many theoretical models [97]. There are extensive theoretical works in literature exploring the longitudinal Young's modulus and Poisson's ratio of CNTs, however little exists on all five elastic parameters (e.g. [31, 87]) and further studies need to be provided.

The longitudinal Young's modulus of CNTs from different studies have been collected by Huang *et al.* [71], showing a vast range of $E=0.97\sim 5.5$ TPa with a variety of CNT wall thickness as listed in Table 2.1. The Young's modulus can be normalized to a unique thickness of 3.4 Å,

$$E_{norm} = E \frac{t}{3.4}, \quad \text{Eq. 2.1}$$

where E is the Young's modulus and t is the CNT wall thickness, assumed in each study. Normalizing the Young's modulus gives rise to a narrow range of $E_{norm}=0.88\sim 1.24$ TPa as listed in Table 2.1.

Table 2.1 The initial and normalized longitudinal Young's modulus and wall thickness of CNTs.

Authors	Method	Wall		
		thickness (Å)	E (TPa)	E_{norm} (TPa)
Lu [74]	MD simulation	3.4	0.97	0.97
Hernández <i>et al.</i> [75]	Tight binding MD simulation	3.4	1.24	1.24
Li and Chou [76]	Structural mechanics	3.4	1.01	1.01
Jin and Yuan [77]	MD simulation	3.4	1.24	1.24
Yakobson <i>et al.</i> [78]	MD simulation	0.66	5.50	1.07
Zhou <i>et al.</i> [79]	Tight-binding model	0.74	5.10	1.11
Kudin <i>et al.</i> [80]	<i>Ab initio</i> computations	0.89	3.86	1.01
Tu and Ou-yang [81]	Local density approximation	0.75	4.70	1.04
Panatano <i>et al.</i> [82]	Continuum shell modelling	0.75	4.84	1.06
Wang <i>et al.</i> [83]	<i>Ab initio</i> calculation	0.665	5.07	0.99
Vodenitcharova and Zhang [70]	Ring theory continuum mechanics	0.617	4.88	0.88

Due to the atomic scale of CNTs, numerical tools used extensively to obtain elastic moduli of CNTs involve MD (e.g. [77, 98-103]), MM (e.g. [51, 65, 104]) and *ab initio* calculations (e.g. [80, 105-108]). More studies have been reviewed by Shokrieh and Rafiee [97].

2.3.3 Elastic moduli of CNT-clusters

Isolated CNTs could be used directly in some applications such as AFM tips [109]. However, to obtain a balanced combination of mechanical and electrical properties of CNTs for some specific applications, it is often desirable to synthesize CNT arrays with a parallel axis to form a cluster with a honeycomb-like structure [110]. These include their applications as springs [111], field emission displays [112], energy storage [113] and

electrical interconnection [114]. A CNT-cluster has a two-dimensional triangular lattice constant, and has a plane of symmetry. Thus, in a sense, it is similar to a crystalline material, and may be approximated to be transversely isotropic [115, 116].

With regard to their applications, CNT-clusters might be used under hydrostatic pressure. Even in CNT-PMCs local hydrostatic pressure can be increased. Extensive investigations on the mechanical properties of such CNT-clusters have been associated with the atmospheric pressure [74, 117-121]. For example, using an empirical force-constant model, Lu [74] extracted bulk and Young's modules of CNT-clusters. They concluded that CNT-clusters show a soft behaviour in the basal plan. Popov *et al.* [118] used an analytical method based on lattice dynamical model [122] to calculate four elastic parameters C_{11} , C_{12} , C_{13} and C_{33} in the atmospheric pressure. Saether *et al.*[116] discussed all five elastic parameters for CNT (12, 0) clusters. Due to the small diameter of CNT (12, 0), the CNT was assumed to be rigid and the vdW interaction was considered to be the only dominant parameter. Liu *et al.* [119] presented a hybrid atomistic/continuum model to study the bulk elastic properties of CNT-clusters in atmospheric pressure, and calculated five independent elastic parameters. In obtaining the out-of-plane shear modulus, however, they assumed that the CNTs were rigid. Nevertheless, there are only a few experimental works to characterize the elastic properties of CNT-clusters. For example, Salvetat *et al.* [94] characterized the elastic and shear moduli of CNT ropes composed with SWCNTs with a diameter of 1.4 nm. Their rope diameter ranged between 3 and 20 nm. They concluded that CNT ropes had a low shear modulus of $G \approx 1$ GPa. Most experimental studies under a high pressure have been conducted with the aid of the Raman spectroscopy [123]. Some specific quantities, such as collapse pressure [124] and phase transformation leading to the shape

deformation of polygonization, ovalization or racetrack [115, 125] have been investigated. Some theoretical studies based on atomistic simulations have also been performed to examine the pressure effect on the phase transformation [125-127] or bulk modulus [128] of a CNT-cluster. Nevertheless, the understanding of five elastic properties of CNT-clusters under a high pressure has been shallow and needs more study.

2.4 Physical properties of polymers

Long molecules of polymers are composed of repeated sub-unites called monomers. Compare to metals, polymers are extremely light and, depending on their molecular structure, can provide a wide range of mechanical properties. Polymers are categorized in different ways. There are two types of thermoplastics and thermosetting polymers. Thermoplastics can be melted and reshaped without chemical decomposition; however, thermosetting polymers cannot be melted even at high temperature. Instead their chemical structure decomposes beyond a certain temperature. Furthermore, polymers might have a fully amorphous structure (e.g., polystyrene [PS] and all thermoset polymers) or semi-crystalline structure (e.g., PE and polyvinyl chloride [PVC]) which are partially crystalline [1, 129].

Physical properties of bulk polymers such as elastic moduli, transition temperatures, density, viscosity and melting point of polymers are dependent on a variety of parameters such as molecular weight, the length of backbone chain and the architecture of their molecular structure. For example, a PE crystal is friable while a fully amorphous PE is a viscous fluid at room temperature. A combination of both morphologies renders a tough

and resilient material as it is [129]. Although, interatomic chemical bonds in one single polymer chain are very strong [130], overall properties of polymers are mainly affected with the chain entanglements and weak vdW interactions which keep the polymer chains close together. As a result, longer chains have less mobility and can resist changing their position under mechanical and thermal loads [131].

Pure bulk polymers are often isotropic materials which can be characterized experimentally similar to any conventional material. However, developing new polymers or improving the interaction between polymer and nano-inclusions required understanding of the internal interactions and mechanisms. To do so, MD has been frequently used to study the dynamic parameters of polymers such as glass transition [132-134] and stress-strain analysis of polymers (e.g. Ref. [39]). Furthermore, due to simpler analysis and smooth results, the static method based on MM theories has been a popular method to predict stress-strain behaviour of polymers. However, this method is valid only for small strain and under specific conditions which has been explained in detail by Theodorou and Suter [135].

One of the most important parameters for amorphous and semi-crystalline materials is their glass transition temperature, T_g , in which the physical behaviour changes from glassy to rubbery or liquid-like. Based on the dilatometric methods, any turning point in the slope of specific volume-temperature curve is indicated as a transition. Due to the existence of crystalline parts in some polymers, they exhibit several turning points which make it hard to find their T_g . For example semi-crystalline PE has three turning points corresponding to three relaxation processes indexed by so-called α , β and γ [136], in which the α process is due to the morphology change of the crystalline portion of PE, and the β and γ processes

are attributed to the amorphous fraction. It was argued that the β process was dominant in a branched PE and was insignificant for a linear PE [137-139]. In their MD simulation of an amorphous PE, Han *et al.* [134] showed that the relaxation process for the amorphous PE was mainly the β process which resulted in the T_g of 250 K. Some other MD simulations of fully amorphous PE reported that T_g is equal to 230 K [134, 140]. Experimental characterizations found, however, that the three turning points are diverse: the γ transition was between 143 K to 173 K; the α transition was in a wider range between 283 K to 343 K; and the β transition was approximately at 253 K [129].

2.5 Interphase of CNT-composites

CNT-matrix interphase is a transient region between the external surfaces of CNTs and the bulk matrix of a CNT-PMC. Compared to the small diameter of a CNT, the thickness of the interphase is considerable. Reynaud *et al.* [141] argued that the volume fraction of an interphase with 1 nm thickness is approximately 0.3%; however, it can reach to 30% in the case of CNT-composites. The interphase region bonds the CNTs to the matrix and plays an important role in determining macroscopic properties of the composite [18, 142]. In the case of a non-bonded CNT-PMC, there are two distinct interphase regions. One is the vdW interphase, which is the gap distance between the CNT atoms and those in the internal surface of the matrix surrounding the CNT. The other is the adsorption layer interphase, which often has a greater density than the bulk matrix [42, 143], hence is called a dense interphase. Some researchers assumed that the vdW gap between the CNT and the matrix was the only interphase region [31, 52, 144] with certain thickness and mechanical properties. However, considering that the vdW interactions may alter the properties of both

CNT and the transition matrix phase, these three-phase models are insufficient to resolve all the details. The effect of the vdW interphase on the nano-composite properties have been investigated to a certain extent. For example, Tan *et al.* [27] studied analytically and reported that the vdW interphase debonds and weakens the composite when the material is subjected to a large strain. Shokrieh and Rafiee [52] used spring elements in a FE analysis to treat the vdW interactions between the CNT atoms and the surrounding matrix. They claimed that the CNT-PMC would have a nonlinear behaviour under a large strain. Using the atomistic simulation, Tsai *et al.* [31] characterized the vdW interphase considering the non-bonded energy between a SWCNT and a matrix. They found that the interphase has a major effect on the transverse Young's modulus of aligned SWCNT-PMCs. The role of the dense interphase has also been studied. Odegard *et al.* [142] developed a continuum-based elastic micro-mechanical model and concluded that the interphase influence would diminish if the radius of a nano-filler is greater than 100 nm. Wang *et al.* [145] developed an FE code to include the interphase effect on the overall properties of nano-composites with different inclusion shapes. They concluded that the interphase is effective when the nano-filler radius is less than 10 nm. In their micro-mechanical model, Yang *et al.* [42] treated the combined vdW gap and SWCNT as an inclusion, but the combined dense interphase and matrix as a new matrix. They reported that a weaker interphase would make the elastic modulus smaller, except that in the longitudinal direction of the SWCNTs.

Extensive work has been done on the multi-phase modelling to investigate the impact of a predetermined interphase on the overall mechanical properties of nano-composites [146, 147]. Nevertheless, very little is available on the characterization of the elastic properties of the interphase layer. Using a micromechanical approach, some relations have been

developed for elastic properties of the interphase (e.g. [57, 148, 149]), which still needs atomistic simulations or experimental tests to determine their key parameters. Alternatively, combined methods of atomistic/molecular simulation and micromechanics were proposed [42, 142, 150] to characterize the “effective interface”. The micromechanics part in this way, however, has a limited capacity and accuracy. Because of these, some researchers have proposed to characterize the interphase directly from atomistic/molecular simulations. For example, Papakonstantopoulos *et al.* [151] used stress fluctuation in the Monte Carlo simulation and Frankland *et al.* [152] used configuration energy in MD simulation to calculate the local elastic properties of the matrix involving the interphase, as a function of the radial distance from the CNT external surface. Yet more investigation is needed to characterize the properties of dense interphase in a simpler way.

2.6 Waviness of CNTs

It has been shown experimentally that most of CNTs are highly wavy in the matrix [8, 9, 23, 153] which is mainly because of low bending stiffness of CNTs. It has been shown that the waviness of CNTs reduces the stiffness of CNT-PMCs [20, 21, 40, 154-160], nonetheless, Pantano and Cappello [154] reported that in the case of poor-bonding CNT-PMCs, waviness can increase the stiffness of CNT-PMCs through the bending energy instead of axial stiffness and energy of the CNTs. To characterize the morphology of wavy fibres and understand the effect of wavy microfibrils or CNTs on the elastic properties of composites, extensive experimental [161] and theoretical works based on micromechanics theories [20, 40, 156, 158, 159], FE methods [154, 160, 162] and a hybrid of FE-micromechanical methods [21, 155] have been used.

Most of the micromechanical works on the waviness of CNTs are based on the Mori-Tanaka method [163]. Since the Mori-Tanaka method was developed for straight inclusions there have been some attempts to modify the method for wavy CNTs. The most controversial subject is to obtain the concentration tensor for the inclusions with different geometries. For example, Bradshaw *et al.* [155] used FE to find dilute stress concentration tensor of wavy CNT of a cubic or wavy RVE. The concentration tensor then was used in the Mori-Tanaka method for aligned or randomly oriented fibres. Although Mori-Tanaka method gives rise to acceptable results for micro scale fibres with simple waviness, still finding the right concentration tensor for random geometry fibres is a matter of research. Furthermore, there are some simple relations based on the Halpin-Tsai equation [164] to fit the experimental data. For example Yeh *et al.* [165] and Omidi *et al.* [14] modified the Halpin-Tsai equation by adopting some additional factors such as orientation factor, shape factor and waviness factor. However, these equations are not able to catch all complicated mechanisms of CNT-PMCs.

In the most of the works explained above the CNTs are treated as uniform wavy fibres with a sinusoidal wave shape [21, 84, 154, 166] or simple bow-wave shape [156, 159] that is suitable for woven microfibres which have a regular fibre shape. Meanwhile, technically it is very hard to produce nano-composites with regular CNT shape. More reliable results for such complicated morphology of wavy CNTs need to use some techniques to characterize the real CNT morphology in the composites. For example Clark *et al.* [161], used the two-dimensional (2D) cross-sectional image of fibres in a composite to figure out the three dimensional (3D) structure of fibres. In a recent work, Bhuiyan *et al.* [167] characterized the probability distribution functions of CNT diameter, orientation, dispersion and

waviness through image analysis. Also, with the aid of some techniques such as voltage-contrast SEM, it is feasible to monitor the sub-surface CNT network up to approximately 250 nm [168]. With those techniques it is feasible to model more real morphology of wavy CNTs with more reliability.

2.7 Multiscale modelling of CNT-PMCs

To characterize the elastic properties of CNT-PMCs, over the past decades, various theoretical methods aiming to understand the dynamic process of CNT-matrix interactions and to predict the mechanical properties of CNT-PMCs have been developed [5, 169, 170]. Most of them, however, are based on the concept of an RVE containing the matrix and the reinforcement to be used in multiscale micromechanics or FE treatments.

The CNT-PMCs have been analyzed with the atomistic simulations [24, 36, 42, 58], the continuum micromechanics [171], the FE method [172] and the semi-continuum FE approach [52, 173]. Atomistic methods have been frequently used to explore the detailed reinforcing mechanisms of CNT-PMCs, such as the effects of CNT-matrix interphase [58], the bonding [19, 174] and the stress-strain properties of nano-scale molecular mechanisms [36, 38]. However, due to the high computational cost, an atomistic method is confined to a small model size of a few nanometers in dimension and a time scale of a few nano-seconds. As a result, such modelling is highly demanding in predicting the macroscopic properties of a CNT-PMC. To overcome the barriers in both length scale and time scale, proper ways have been explored to extract useful information from a limited number of atomistic simulations.

With the time and length restrictions of atomistic methods, the continuum approaches of micromechanics [30] and FE methods have been used extensively. However, these approaches are still based on the continuum assumption, which cannot capture all the interactions between the CNTs and the matrix. However, to improve the applicability of micromechanics significant efforts have been made to develop the interphase modelling techniques, such as the thin shell interphase treatment [29, 56, 57]. Although, the properties of the transient regions in the treatment still need the application of other methods such as MD and MM analyses [58]. At the same time, some strong assumptions and simplifications must be used to make the micromechanics applicable.

Besides directly using FE method to obtain a more accurate solution of the stress field, efforts have also been made to construct complicated FE model of CNT-PMC. Shokrieh and Rafiee [52] establish the FE model of CNT-PMC with the carbon-carbon bonds represented by beam elements (originally developed by Li and Chou [76]) and the vdW interactions between the CNT atoms and the adjacent matrix by nonlinear springs. They proposed that the region occupied by CNT and the equilibrium vdW gap may be considered as a single solid phase. In their study some important factors, such as the non-local effect of the vdW forces and the transition region in the matrix, were ignored.

The controversial issues associated with the continuum and semi-continuum methods are the determination of the properties and the geometries of the nano-inclusions and the interphase regions. As a result, these properties and geometries cannot be properly accounted by the micromechanics or the FE treatments directly. For example, a semi-continuum FE approach treats the vdW interaction as spring elements to connect a

continuum matrix to the CNT atoms and constructs the CNT interatomic bonds as beam elements. This approach is convenient as it can integrate all simulations in a single FE code commercially available and is appropriate to study regular structures such as MWCNTs [175]. However, the spring element simply connects the internal surface of the matrix, without taking into account the fact that the vdW interaction is non-local and that each atom of CNT interacts with several atoms of the matrix and the CNT within the cutting radius. Moreover, compared to the atomistic methods this kind of treatment is unable to predict the equilibrated location of atoms of the amorphous matrix adjacent to the CNT.

A sensible solution is multiscale modelling of CNT-PMCs including a continuum model of composites with essential parameters determined from atomistic simulations. For instance, Odegard *et al.* [58] proposed a semi-continuum approach. They used MD to equilibrate the atomistic model and then established an equivalent truss system describing the inter-atomic interactions. The equivalent truss model was then applied to calculate the properties of an equivalent-continuum fibre applicable in micromechanics. Tsai *et al.* [31] also developed a combined modelling method using atomistic simulation and micromechanics. In their analysis, a composition of the CNT (as a solid fibre though), the equilibrium vdW gap, and the bulk matrix was established. They treated the vdW gap as a solid phase with the elastic properties quantified from MD simulation. The multiscale treatment can integrate the accuracy of atomistic simulations with the efficiency of continuum-mechanics methods. Many multi-scale models have been developed, yet a reliable method with minimum simplification in nano- and micro-scale needs to be developed.

2.8 Summary

In this chapter, the background on the available characterizing methods for CNT-PMCs was discussed and a sufficient literature review was provided. It was argued that multiscale modelling methods are the most suitable methods for characterizing CNT-PMCs which an accurate technique for nano-scale is integrated with a quick response method for macroscopic scale. The literature review revealed following gaps in knowledge that need further studies.

- i) There exist a little theoretical works on characterizing all five elastic parameters of CNTs and CNT-clusters especially under a high pressure.
- ii) Although there exist extensive studies on the impact of a predetermined interphase on the overall mechanical properties of nano-composites, yet the studies on the characterization of the elastic properties of the interphase layer is shallow.
- iii) Extensive studies on the effect of waviness on the elastic properties of CNT-PMCs have been done, nevertheless, in most of them wavy CNT have been treated as sinusoidal wave shape or simple bow-wave shape. A technique should be developed to generate more real CNT morphology in a composite.
- iv) A multi-scale method with minimum simplification in both nano- and micro-scale needs to be developed.

Chapter 3

Chapter 3

Basics of atomistic simulation methods and Materials Studio settings

3.1 Introduction

Computational chemistry methods such as QM, MD, MM and CG provide the theoretical platform to study the dynamics of atomistic and molecular structures aimed at improving their properties or to design new materials. With improving power of computers during the last few decades, an extensive range of software tools have been developed to carry out atomistic simulations. Materials Studio [176], developed by the Accelrys company, is one of the most powerful software packages for simulating and modelling of materials. Materials Studio includes several modules involving a vast range of quantum, atomistic and molecular simulation tools. In this thesis, the Forcite module was used for all MD and MM simulations. Forcite is an advanced classical mechanics tool, which, in conjunction with the modelling and simulation environment of Materials Studio, provides a powerful platform for energy calculation, MD simulation and geometry optimization with the aid of MM.

Compare to the classic continuum mechanics, atomistic simulation methods are almost new for engineering applications. This chapter provides a sufficient theoretical background regarding this research. Eventually, the Materials Studio settings are adjusted for a higher efficiency. The manual of Materials Studio [176] has been used to expand some sections of this chapter.

3.2 Basic concepts

3.2.1 *ab initio* quantum mechanics methods

Ab initio quantum mechanics is based on the accurate solution of the Schrodinger equation [46],

$$H \Psi(R, r) = E \Psi(R, r), \quad \text{Eq. 3.1}$$

where H and E are Hamiltonian and energy of the wave function (Ψ), respectively. In Eq. 3.1, Ψ is a function of the coordinates of the nuclei (R) and of the coordinates of the electrons (r). The Schrodinger equation is very complex to solve. Since the electrons are several thousand times lighter in weight and faster in velocity than nuclei, Born and Oppenheimer [177] proposed an approximation that the motion of electrons can be decoupled from the motion of nuclei giving rise to two independent equations. The first one represents the electronic motion, defined as

$$H \Psi(r; R) = E \Psi(r; R). \quad \text{Eq. 3.2}$$

This equation can be solved directly with the *ab initio* codes giving rise to an energy function, called *potential energy surface*, that is a function of nuclei coordinates (R). The second equation describes the nuclear motion on the *potential energy surface*, defined as

$$H \Phi(R) = E \Phi(R). \quad \text{Eq. 3.3}$$

This equation is important when the time evolution of atomic model is desired.

3.2.2 Molecular dynamics and molecular mechanics

To study the dynamics of an atomistic system, Eq. 3.2 should be solved as a prerequisite for Eq. 3.3. However, a massive computational effort is necessary to solve Eq. 3.2. Thus, to reduce the calculation cost, a lot of effort has been made to fit a function to the *potential energy surface* called a “force field” (V). To date, there is not a versatile force field applicable for all materials. Each force field can be parameterized for a small group of elements with a high accuracy or for a vast range of elements by sacrificing the accuracy. A powerful force field is able to cover a vast range of elements with a reasonable accuracy. Since nuclei are relatively heavy objects for simplicity their quantum mechanical effects are ignored and Eq. 3.3 is represented with Newton's equation of motion,

$$F = -\frac{dV}{dR} = m \frac{d^2R}{dt^2}, \quad \text{Eq. 3.4}$$

where F and m are interatomic force and atomic mass. Alternatively, Eq. 3.4 can be defined for each atom i as,

$$f_i = -\frac{\partial V}{\partial r_i} = m_i \frac{d^2 r_i}{dt^2}, \quad \text{Eq. 3.5}$$

To study the dynamics of an atomistic system in an MD simulation, the initial velocities of all atoms at $t = 0$ are assigned randomly with a Maxwell-Boltzmann distribution. The same as any ordinary differential equation, Eq. 3.5 for all atoms are assembled and solved numerically with the finite difference method. The position and velocity of each atom is

then evaluated after a time step Δt and repeats for the next steps at $t + \Delta t$. Ignoring the time evolution part of Eq. 3.5 (right-hand side term), leads to an MM simulation. Usually, dynamics concepts such as melting point and glass transition temperature of materials are evaluated with MD simulations, whereas the static problems such as relative structural energy and equilibrium structures can be treated by MM. Depending on the material structure and loading conditions, both MM and MD have been used for stress analysis [178-180]. It is noted that theoretically, MM is performed in absolute zero temperature.

In a regular MD, the equations of motion for all atoms are integrated that give rise to detailed information about each atom. However, such details are not necessary to study some physical properties such as variation of morphology, and equilibration of large molecules of proteins or polymers. In those cases, a group of atoms is replaced with a bead to reduce the number of equations, known as coarse-grained molecular dynamics (CG), which reduces the computational run time by two to three orders of magnitude compared to all atom MD simulations [181]. Nevertheless, some processes such as stress-strain analysis need more details through all atoms MD and MM simulations.

3.3 COMPASS force field

In atomic force fields, atoms are treated as single balls and their interatomic interactions are represented with different single or combined mechanical springs such as torsion, stretch and bend. A force field represents an expression of potential energy surface of a particular atomistic structure as a function of its atomic coordinates, and load terms such as bond angle, bond distance and torsion.

In this study, an *ab initio* second-generation force field, COMPASS (Condensed-phase Optimized Molecular Potentials for Atomistic Simulation Studies), is applied to describe inter- and intra-atomic interactions. COMPASS belongs to the “consistent force fields” family, those with the same functional form but different parameter values. Using *ab initio* simulations and a wide range of experimental observations, COMPASS was originally developed and parameterized by Sun [47, 48]. It is one of the most suitable force fields for investigating organic molecules, inorganic small molecules, and polymeric composites (*e.g.*, [24, 150, 182-186]). The functional form of COMPASS is general and flexible which can be parameterized accurately for a wide range of materials. In the consistent force fields, the total potential energy of an atomistic system is expressed as a summation of three interaction energies: bond or valence ($E_{valence}$), cross-coupling terms ($E_{cross-term}$), and non-bonded ($E_{non-bond}$) energies.

$$E_{total} = E_{valence} + E_{cross-term} + E_{non-bond} \quad \text{Eq. 3.6}$$

A great feature of the second-generation force fields is their higher accuracy due to involving the cross-coupling terms [24], which account the bond or angle changes, caused by the nearby atoms. Each term of Eq. 3.6 has been expanded in Appendix 2.

3.4 Progress control

Newton’s equations of motion for all atoms can be integrated to predict the dynamics of atomistic systems with a conserved level of energy. However, the overall energy of the atomistic system is changed with the variation of pressure or temperature. Therefore, some progress control algorithms are essential to control the level of statistical conditions of

pressure and temperature. Different algorithms have been developed to keep a constant state for variables such as temperature (T), pressure (P), Stress (σ), volume (V), enthalpy ($H=E+PV$), and number of atoms (N). Moreover, several thermodynamic ensembles have been developed to keep a group of parameters constant. For example, NPT ensemble states a constant number of atoms (N), pressure (P), and temperature (T). Four thermodynamic ensembles of NPT, NVT, NVE, and NPH are supported by Materials Studio. It is noted that, the number of atoms of all ensembles are kept constant.

In this thesis, only two ensembles of NPT and NVT are used. It depends on the application of MD simulation to select one of the ensembles above. For example, volumetric coefficient of thermal expansion is obtained experimentally by recording the volume of a sample in each temperature state, while pressure is constant. This process numerically is equivalent to NPT ensemble. The NVT ensemble called *canonical ensemble*, can fix the cell dimensions during MD simulation and does not care about the pressure fluctuations. In this thesis, the NVT ensemble is used for the last stage of equilibration process before the stress analysis.

3.5 Atomistic temperature

Temperature is a thermodynamic quantity which is a function of average kinetic energy of the atomistic system.

3.5.1 Evaluation of temperature

The quantity of temperature is calculated through the Equipartition theorem [187] that is

$$\left\langle \sum_i^N \frac{P_i^2}{2m} \right\rangle = \langle K \rangle = \frac{N_f k_B T}{2}, \quad \text{Eq. 3.7}$$

where P_i is the momenta of atom i with mass m in an atomistic system involving N atoms. Furthermore, K , N_f , T , and k_B are kinetic energy, number of degrees of freedom, temperature of atomistic system, and Boltzmann constant, respectively. The terms inside $\langle \rangle$ are statistically averaged for a while. A more convenient way to define an instantaneous kinetic temperature is

$$T_{inst} = \frac{2K}{N_f k_B}. \quad \text{Eq. 3.8}$$

Thermodynamic temperature is an average of instantaneous temperature of Eq. 3.8 for a moment. It is noted that, at a certain temperature the atoms of the system do not follow the same velocity pattern. However, X , Y and Z components of velocity for atoms have a probability distribution which are represented with Maxwell-Boltzmann equation, i.e.,

$$f(v) = 4\pi v^2 \left(\frac{m}{2\pi K_B T} \right)^{3/2} \exp \left(-\frac{mv^2}{2K_B T} \right). \quad \text{Eq. 3.9}$$

The velocity (v) of atoms depends on their mass and the temperature of the system. A schematic Maxwell-Boltzmann distribution has been shown in Fig. 3.1. The graph shows that for a lower temperature most of the atoms are slow; however, the number of high velocity atoms increases with temperature rise.

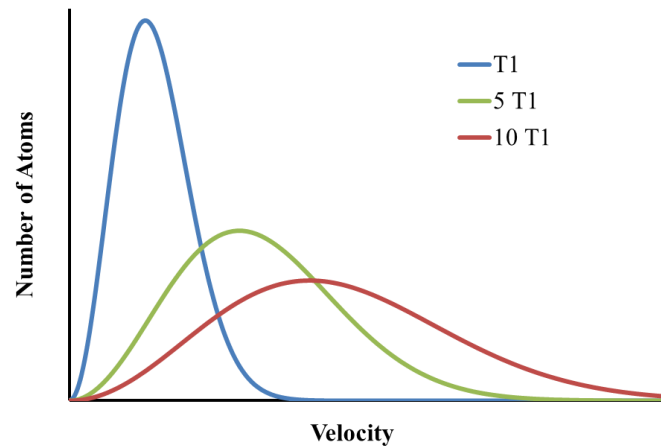


Fig. 3.1 Maxwell-Boltzmann distribution of water with temperature variation.

3.5.2 Controlling temperature

The initial velocities of atoms in an MD process are set based on the Maxwell-Boltzmann distribution function. However, at the beginning, the atomistic structure is not in a global minimum energy state. In other words, there are some local high potential energy spots, which release their energy at the beginning of MD simulation. As a result, the kinetic energy and subsequent temperature of the atomistic system is artificially increased. The same disturbance happens right after applying a sudden external load to the atomistic system. To remedy this problem, some algorithms have been developed to keep the desired temperature constant by tuning the statistical velocity distribution of atoms. In Materials Studio there are four methods to control the temperature that include direct velocity scaling, Berendsen, Nosé, and Andersen. In the direct velocity scaling method, the velocity of all atoms (V_{old}) are simply scaled to adjust the target temperature (T_{target}).

$$\frac{T_{Target}}{T_{System}} = \left(\frac{V_{new}}{V_{old}} \right)^2, \quad \text{Eq. 3.10}$$

Where T_{System} and V_{new} are current temperature of atomic system and velocity of atoms. In the Berendsen method the simulated system is coupled to an external bath with a constant temperature [188]. The velocity of each atom is then scaled by a proportional factor of λ ,

$$\lambda = \left[1 + \frac{\Delta t}{\tau_T} \left(\frac{T_0 - T}{T} \right) \right]^{1/2}, \quad \text{Eq. 3.11}$$

where Δt is the time step size, τ_T is the temperature coupling time constant, T_0 is the target temperature and T is the instant temperature. Nosé method also known as Nosé-Hoover method, adds an additional degree of freedom to the atomistic system which represents the interaction of system with heat bath. More detail is beyond the scope of this thesis and can be reviewed in Refs. [189-191]. In the Andersen method, the velocity of all atoms are randomized periodically to keep a constant temperature. We examined all four methods above with a polymer sample and realized that the Berendsen method is superior one in aspects of both convergence and stability. In Berendsen method, the coupling time constant, τ_T , is an important factor which has been recommended to be between 0.1 to 0.4 ps [188]. Our simulations show that reducing τ_T gives rise to a fast convergence of temperature with a noisy kinetic energy. Selecting a very low τ_T can threaten the stability of MD system and stop the progress after a few iterations. In this study, MD is used mainly for equilibration of atomistic systems in which the fluctuation of energy is not an important issue. After a few numerical tests for polymers and CNT-PMCs, a small $\tau_T = 0.005$ was selected which showed a stable system with a discrepancy of temperature less than 2% in 300K.

3.6 Atomistic stress and pressure

In continuum mechanics, stress is defined as the average interaction force between the particles of either sides of an imaginary cutting plane per unit area. Based on the Cauchy stress definition, three-dimensional stresses on the surfaces of an infinitesimal cube of a body are defined as a symmetric tensor with six independent components [192],

$$\sigma = \begin{bmatrix} \sigma_{11} & \sigma_{12} & \sigma_{13} \\ \sigma_{21} & \sigma_{22} & \sigma_{23} \\ \sigma_{31} & \sigma_{32} & \sigma_{33} \end{bmatrix} = \begin{bmatrix} \sigma_{xx} & \sigma_{xy} & \sigma_{xz} \\ \sigma_{yx} & \sigma_{yy} & \sigma_{yz} \\ \sigma_{zx} & \sigma_{zy} & \sigma_{zz} \end{bmatrix} \equiv \begin{bmatrix} \sigma_x & \tau_{xy} & \tau_{xz} \\ \tau_{xy} & \sigma_y & \tau_{yz} \\ \tau_{xz} & \tau_{yz} & \sigma_z \end{bmatrix}, \quad \text{Eq. 3.12}$$

where $\sigma_{12} = \sigma_{21}$, $\sigma_{13} = \sigma_{31}$, and $\sigma_{23} = \sigma_{32}$. The stress tensor includes both normal stress ($\sigma_x, \sigma_y, \sigma_z$) and shear stress ($\tau_{xy}, \tau_{xz}, \tau_{yz}$) components.

3.6.1 Atomistic stress evaluation

The same concept of continuum mechanics has been statistically used to calculate stress components on a surface at atomistic scale known as Lagrangian atomic stress [180, 193]. However, the most popular method has been the virial equation [194]. According to the virial equation, the instantaneous stress tensor with the same notation of Berendsen *et al.* [188] is defined as

$$\sigma = -\frac{1}{V} \left[\left(\sum_{i=1}^N m_i (v_i v_i^T) \right) + \left(\frac{1}{2} \sum_{i=1}^N \sum_{j=1}^N r_{ij} f_{ij}^T \right) \right], \quad \text{Eq. 3.13}$$

where m_i and v_i are respectively the mass and velocity vectors of the i^{th} atom, and r_{ij} and f_{ij} are relative position vectors and interatomic force vectors between i^{th} and j^{th} atoms,

respectively. Eq. 3.13 indicates the instantaneous average stress of the atomistic system involves N atoms with a total volume of V . As an alternative, the components of average virial stress can be expressed as [195],

$$\sigma_{lm} = -\frac{1}{V} \sum_{\alpha=1}^N \left[m^{\alpha} (v_l^{\alpha} v_m^{\alpha}) - \frac{1}{2} \sum_{\beta=1}^N r_l^{\alpha\beta} f_m^{\alpha\beta} \right], \quad \text{Eq. 3.14}$$

where l and m take values in x , y and z directions, m^{α} , v_l^{α} , and v_m^{α} are the mass, and the velocities of atom α in the l and m directions, respectively. $f_l^{\alpha\beta}$ and $r_m^{\alpha\beta}$ are the interatomic force and the relative position between atom α and atom β , respectively.

Pressure is another thermodynamics state variable which is a type of stress with hydrostatic conditions (i.e., $P = \sigma_x = \sigma_y = \sigma_z$ and $\tau_{xy} = \tau_{xz} = \tau_{yz} = 0$). In the non-hydrostatic conditions, a mean instantaneous pressure is calculated as the average trace of the stress tensor (i.e., $P = (\sigma_x + \sigma_y + \sigma_z) / 3$). In Materials Studio, both stress and pressure are evaluated through virial stress equations.

3.6.2 Pressure/stress control methods

In Materials Studio, the pressure of an atomistic system under NPT ensemble can be controlled with scaling the cell volume. In this study, two methods of Brendsen [188] and Parrinello-Rahman [196] are used. The Brendsen method changes the cell dimensions with the same ratio giving rise to a non-homogeneous stress for solid materials. However, the Parrinello-Rahman method can control both stress and pressure by changing the cell shape and dimensions independently.

The Brendsen method couples the atomistic system with a pressure bath to adjust the pressure by changing the virial of the system through scaling the inter-atomic distances and the cell dimensions [188]. The scaling factor is

$$\mu = \left[1 + \frac{\Delta t}{\tau_p} (P - P_0) \right]^{1/3}, \quad \text{Eq. 3.15}$$

where Δt , P , P_0 , and τ_p are the time step, the instantaneous pressure, the target pressure, and the pressure-time constant respectively. In Materials Studio, the pressure-time constant is 0.1 by default. The smaller τ_p gives rise to a faster convergence with more instability. Since the Brendsen method is not able to change the MD cell dimensions independently, it is not suitable for studying solid materials especially anisotropic ones. In our simulations, τ_p was set to 0.05 which showed a stable system with a low fluctuation of pressure.

The Parrinello-Rahman method was extended based on Andersen's method [197] to allow both the size and the shape of the MD cell to be changed. In this method an arbitrary shape of the MD cell is defined by a set of three vectors a , b , and c that spans the edge. The vectors are arranged in a 3×3 matrix of $h = \{a, b, c\}$ which involves nine cell variables. An MD system consists of N particles that are defined with a set of $3N$ variables of coordinates. In the Parrinello-Rahman method the time evolution of all $3N+9$ variables including particles and cell parameters, under hydrostatic pressure, are obtained from the Lagrangian equation,

$$L = \frac{1}{2} \sum_{i=1}^N m_i \dot{s}_i^T G \dot{s}_i - \sum_{i=1}^N \sum_{j>i}^N \phi(r_{ij}) + \frac{1}{2} W \text{Tr}(\dot{h}^T \dot{h}) - p_{ext} V, \quad \text{Eq. 3.16}$$

where m_i is the mass of atom i , s_i is the fractional coordinate of atom i , tensor G is defined as $G=h^T h$, ϕ is the interaction potential, r_{ij} is the interatomic distance (i.e., $r_{ij} = |r_j - r_i|$), P_{ext} is the external pressure on the system, V is the MD cell volume (i.e., $V = \det h$), and W is a mass-like user-defined variable to adjust the rate of volume/shape variation. The dots above some parameters indicate the time derivative. The first two right-side terms of Eq. 3.16 are the kinetic and potential energies respectively which represent the Lagrangian of the original system. The third term of Eq. 3.16 is the kinetic energy associated with the variation of the cell parameters and the last term represents the elastic energy relating to the external target pressure and the cell volume. The equation of motion for atoms and cell vectors could be derived from Eq. 3.16 which has been discussed in detail by Parrinello and Rahman [196].

The mass-like user-defined variable, W , is an important variable to adjust the variation rate of volume/shape. The proper quantity of W depends on the cell size and material properties. A large quantity of W gives rise to a slow variation of the cell vectors which is suitable for small-structure and liquid-like materials. In contrast, small W leads to a fast variation of cell dimensions that can reach to the desired shape very soon; however, it can threaten the stability of systems as well. After several numerical tests for polymers and CNT-PMCs, the appropriate W was set to 10 amu, which shows a stable and gentle behaviour.

3.7 Periodic boundary conditions

In computer simulation of materials, it is not possible to simulate a large system of materials. Therefore it is preferable to select a small unit cell of material far from the edges

which theoretically is equivalent to a unit cell surrounded by replicas of itself in a periodic boundary condition (PBC) that simulates an element inside bulk material without any artificial surface energy. In a PBC, when an atom leaves the cell through one face, it substitutes from the opposite faces with the same velocity, keeping a constant number of atoms. The size of the unit cell should be small enough to reduce the computational cost, yet large enough to avoid artificial effects. For example, Fig. 3.2a shows a CNT-PMC, including a SWCNT embedded in a polymeric matrix with a non-periodic boundary. However, in a PBC the central CNT is surrounded by polymer chains from other image cells as well (see Fig. 3.2b).

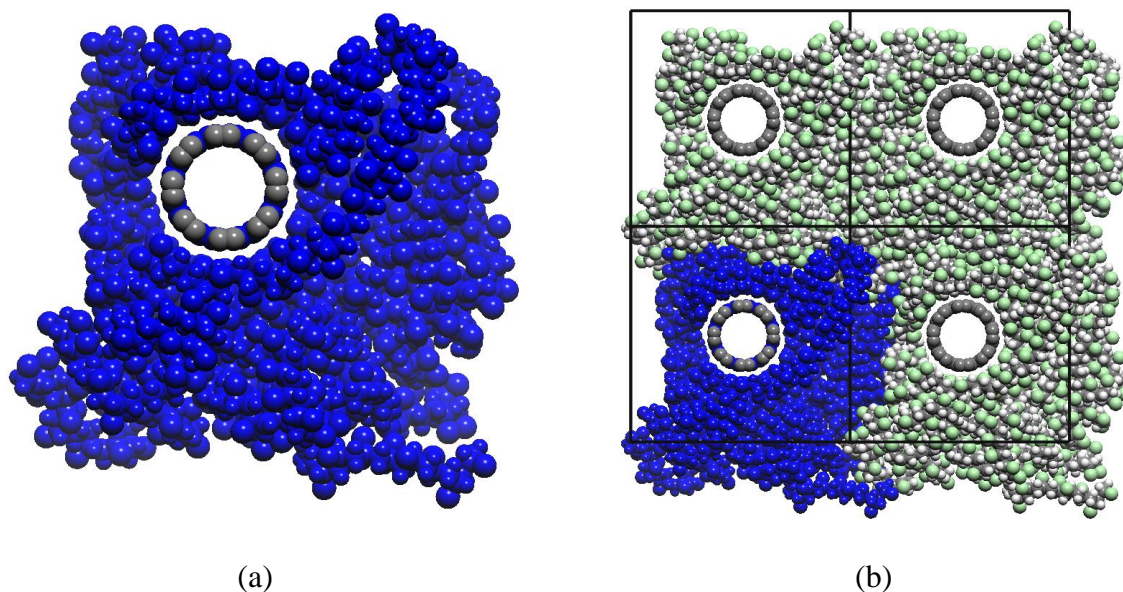


Fig. 3.2 Front view of a SWCNT-PMC: (a) non-periodic boundary, and (b) periodic boundary.

It is straightforward to construct crystalline or gas materials under PBC; however, it is challenging to generate random-walk amorphous polymer chains in a PBC cell. For example, a part of a long-chain polymer may lie in the image cells and vice versa, as shown in Fig. 3.2b. To avoid coincidence between atoms of the parent molecules with the image

ones, in this thesis, the Amorphous cell package of Materials Studio is used to generate random-walk chains of polymers based on the work of Theodorou and Suter [198].

3.8 Non-bonded summation methods

The evaluation of the non-bond interactions, including electrostatic and vdW interactions, are the most time-consuming part of atomistic simulations. To reduce the calculation load, different summation methods have been developed to ignore or approximate non-bonded interactions between far distant atoms. With the Forcite modulus of Materials Studio, there are three summation methods of atom-based cut-offs, group-based cut-offs and Ewald sums.

In atom-based cut-offs or direct method, the non-bond interactions between one atom and surrounding atoms within a spherical region with a certain radius (cut-off radius) are calculated. The biggest fault associate with this method is the energy jumping which is caused when an atom moves in or out of the spherical boundary. The energy jumping can be reduced by increasing the cut-off radius; however, it should be noted that the simulation run time increased proportional to the fourth order of the cut-off radius.

In the group-based cut-offs method, the entire molecule or charge groups with net charge of zero are involved in the cut-off region. Using the same cut-off distance, this method is faster than atom-based cut-offs method and gives rise to more accurate results for electrostatic interactions.

The Ewald method [199, 200] is favourable for calculating the non-bonded energies of crystalline solid structures, however, the method is applied to amorphous solids and

solutions. It has been reported that, compared to atom-based cut-offs, the Ewald method has a lower computational cost for an equivalent accuracy. The Ewald summation method in Materials Studio is based on the work of Karasawa and Goddard [201]. Due to its accuracy, in this thesis, the Ewald method has been selected as the summation method.

3.9 Reducing MD run time in Materials Studio

The most important drawback of MD simulations is their high computational cost, which has restricted both time and length scale of MD simulations. The run time of MD simulations are scaled by $O(N^2)$, which N is the number of atoms. The run time can be reduced in different ways such as by reducing the accuracy of MD simulation, increasing time step, reducing the MD cell size or selecting a proper summation method. However, minimum requirements should be satisfied to obtain acceptable results. The optimum quantity of a parameter can be determined through sensitivity tests in which the parameter is adjusted until the results are stabilized.

3.9.1 Accuracy of MD simulation

Higher accuracy of MD simulations gives rise to a longer run time. Therefore, it is necessary to explore the optimum accuracy for a simulation. In Materials Studio, the accuracy of each parameter can be tuned manually; however, there are four predefined options to adjust the accuracy of all parameters as shown in Table 3.1.

Our simulations show that the most time-consuming part of atomistic simulation of amorphous polymers is the equilibration process and characterizing the dilatometric graphs

of a material. As an example, a single molecule of PE with a polymerization number of $n=100$ in a PBC with Ewald summation method was examined for a period of 1 ns with a time step of 1 fs. The total simulating run time hours have been shown in Fig. 3.3. The results show that the total run time for ultra-fine quality is 10 times that of coarse quality.

Table 3.1 Accuracy of different parameters under four quality settings

	Coarse	Medium	Fine	Ultra-fine
Electrostatic/vdW cut off distance (Å)	9.5	12.5	15.5	18.5
Ewald accuracy (kcal/mol)	0.01	0.001	0.0001	0.00001
Energy (kcal/mol)	0.002	0.001	0.0001	0.00002
Max. force (kcal/mol/Å)	2.5	0.5	0.005	0.001
Max. stress (GPa)	2.5	0.5	0.005	0.001
Max. displacement (Å)	0.05	0.015	0.001	0.00001

However, Fig. 3.4 shows that the average cell volume has not been affected much by the quality. Since the dilatometric graphs are a function of the cell volume in different temperature states, the results indicate that the coarse quality is enough for equilibration process and to determine dilatometric graphs.

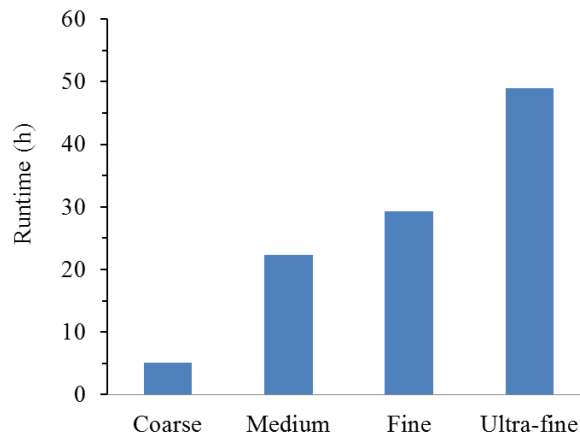


Fig. 3.3 Run time against quality of MD calculation

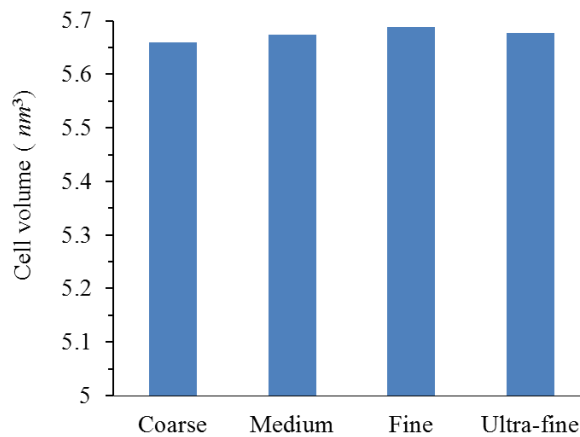


Fig. 3.4 Average cell volume against quality of MD calculation

One important aim of this thesis is to evaluate the elastic properties through stress-strain analysis with MM simulations. To understand the minimum quality requirement, a simple tensile test on a sample amorphous polymer was examined with different qualities. Fig. 3.5 shows that coarse and medium qualities are not able to obtain linear stress-strain graphs and that the reliable qualities are fine and ultra-fine. For more trustworthy results, in this study,

the quality for stress-strain analysis was set to ultra-fine . More details about stress-strain analysis of polymers will be explained in the next chapter.

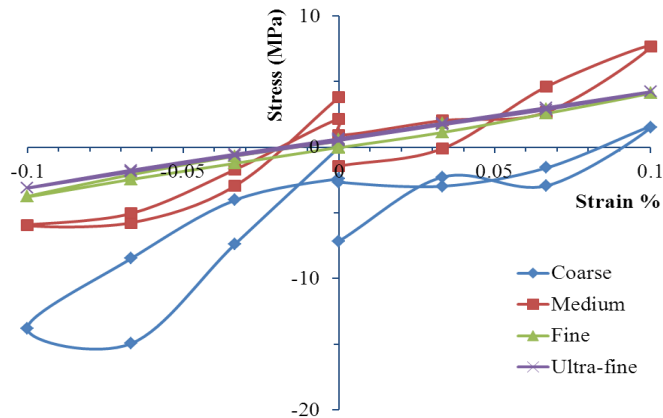


Fig. 3.5 Sample stress-strain graphs of pure PVC for different MM qualities.

3.9.2 Proper time step

The MD time step (Δt) should be small enough to avoid discretization error, and large enough to reduce the computational cost. Usually, the time step should be a fraction of the smallest vibrational period of the system and is in the order of 1 femtosecond (10^{-15} s). In the equilibration process of polymers, which is the most time-consuming part of our atomistic simulations, increasing the time step can reduce the computational cost. Our simulations of polymers at room temperature showed that the time step for polymers can be increased up to 2.5 fs. However, with this time step, the atomistic system is not stable at high temperature. For more consistency, in this thesis, a time step of 1 fs was set for all MD simulations.

3.9.3 Cell size

The run time of an MD simulation of an atomistic system including N atoms is in the order of N^2 (i.e., $O(N^2)$). For instance, if cell sizes are doubled, the volume or the number of involved atoms increases by eight times, and the run time rises to 64 times that of original cell. Therefore, it is desirable to minimize the cell size as much as possible although the cell size should be big enough to avoid any artificial effect. For example, bulk amorphous polymers are often known as isotropic materials. However, a very small cell involving a short chain of polymer (though with random distribution) is highly orthotropic, which obviously is not a proper representative volume element of bulk material. In this thesis, a few samples of amorphous polymers with different cell sizes were examined which showed acceptable isotropic properties for cubic samples of 30 Å in dimensions and beyond that. In the case of CNT-PMC samples, the cell dimensions were increased to avoid any close contact between CNTs which are discussed in more detail in Chapter 6.

Chapter 4

Chapter 4

Atomistic simulation of polymers with different morphology and additives

This chapter is based on: *“Effect of chain morphology and carbon-nanotube additives on the glass transition temperature of polyethylene”* by S. Herasati, H.H. Ruan and L.C. Zhang, published in *Journal of nano research Volume 23, 2013, Pages 16-23.*

4.1 Introduction

Mechanical properties of bulk polymers can be extracted with macroscopic experimental methods. Furthermore, some tools such as atomic force microscopes and nano-indenters have been developed to characterize nano-scale properties. However, it is still beyond the capacity of experimental tools to reveal detailed mechanisms of materials or provide a way to optimize their mechanical properties.

The atomistic simulations methods developed during recent decades are powerful tools for characterizing nano-scale materials; however, it is essential to select a proper force field and to make an accurate model to obtain reliable results. A variety of parameters such as density, glass transition temperature and elastic properties of commercial polymers were characterized many years ago [1] and can be used as criteria to examine the atomistic models and the pertinent force fields.

In this chapter, a procedure of atomistic simulation and the COMPASS force field is validated for a variety of thermoplastic polymers and as a general case, the effect of chain

morphology of PE and CNT additives on the T_g , as a fundamental parameter, is considered. Also, the capability of the static method, based on MM simulation, to predict the elastic properties of polymers is explored.

4.2 Modelling

In this study, only thermoplastic polymers with both amorphous and semi-crystalline structures are discussed. To this end, PE is selected as sample semi-crystalline polymers and PS and PVC as amorphous polymers. Molecules of polymers are composed of multiple repeating monomer units which, in the case of solid polymers, are often in the order of several thousand units. However, because of the massive computational cost of MD and MM simulations, it is not feasible to simulate polymers in a real size. Thus, it is desirable to construct atomistic models as small as possible. However, the mechanical properties of polymers such as tensile strength, hardness and stiffness are a function of their molecular weight [202], defined as

$$S = S_{\infty} + \frac{C}{w}, \quad \text{Eq. 4.1}$$

where S and S_{∞} are mechanical quantity at a certain molecular weight (w) and for an infinitely large molecule, respectively, and C is a constant which depends on the material and the physical property under study. The schematic diagram of Fig. 4.1 shows that, strength/stiffness of polymers raise sharply with increasing molecular weight and approaches their extreme value of S_{∞} . The same behaviour is expected for the other mechanical properties.

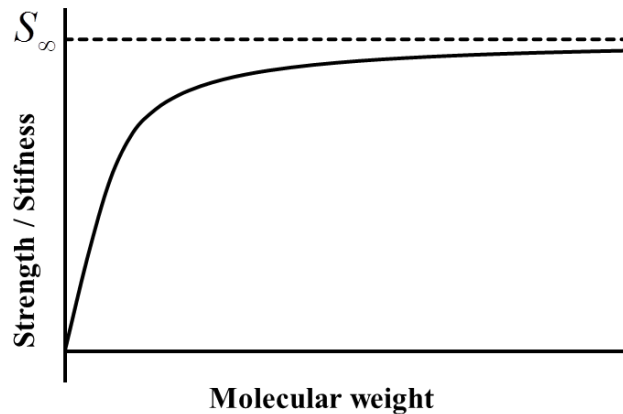


Fig. 4.1 A typical graph of polymer strength as a function of molecular weight

With reference to the argument above, the molecular weight of solid polymers in the atomistic models should not be smaller than a certain quantity. For example, a pure PE consists of alkanes with the formula $C_{2n}H_{4n+2}$, where n is the degree of polymerization. Some MD simulations have been on the pure amorphous PE chains with $n < 50$ (viz. molecular weight less than 1,400) [203, 204]. However, it is known that in reality PE chains are very long with several thousands of atoms, and that PEs with chains of less than 1,400 molecular weight are waxy solids and cannot carry any load [129]. Therefore a representative atomic model of PE should have more than 100 carbon atoms in each chain. To clarify different issues relating to polymers overall, three polymers are modelled as detailed below.

4.2.1 Polyethylene

PE chain could be a simple linear one or include one or more branches and include a crystalline part. Although there are many experimental studies on the T_g of PE [136, 138], and some atomistic simulation on the fully amorphous PE [140, 204], the atomistic

mechanisms of the effect of the polymer chain branches and their crystallinity, and the influence of reinforcements are still unclear. In this study, all PE chains have more than 100 carbon atoms for more reliable results. In addition to pure PE, CNT reinforcements were also examined, which have been investigated overwhelmingly recently [25, 38, 39, 205-207]. To study the effect of crystallinity, polymer branches and CNT additives on the T_g of PE, five schemes are considered as below.

PE scheme 1 is a fully amorphous PE cube with $n = 400$ (Fig. 4.2a).

PE scheme 2 is a semi-crystalline linear PE (no branches) (Fig. 4.2b), consisting of an orthorhombic crystal of PE of 180 carbon atoms and random-walk PE chains with $n = 200$ surrounding the crystal.

PE scheme 3 has the same crystal structure as PE scheme 2 (Fig. 4.2c) but the surrounding PE chain has six branches with $n = 8$. This scheme represents a realistic PE which contains both crystallinity and branched chains.

PE scheme 4 is a PE composite consisting of a short-capped CNT (10, 10) of 360 carbon atoms (Fig. 4.2d). The PE has linear amorphous chains with $n = 400$.

PE scheme 5 is also a PE composite reinforced by CNT (10, 10) which in respect to the periodic boundary has theoretically an infinite length. There are 485 carbon atoms in the simulation cell (Fig. 4.2e).

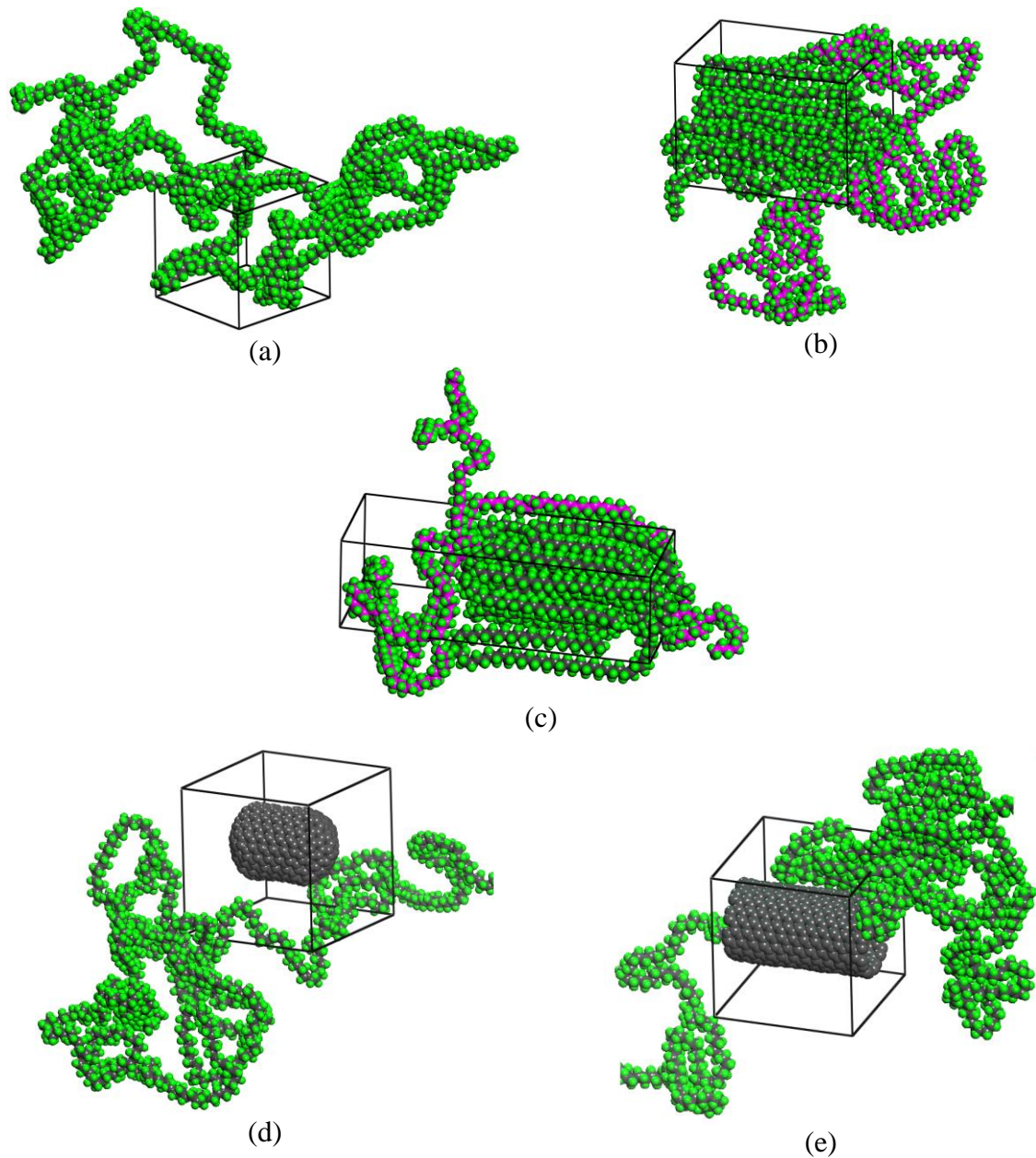


Fig. 4.2 Polyethylene and its composite schemes: a) fully amorphous PE, b) semi-crystalline with linear amorphous PE chains, c) semi-crystalline with branched amorphous, d) a composite with short-capped CNTs and linear PE chains, and e) a composite with infinitely-long CNTs and linear PE chains.

Hydrogen atoms are shown in green and carbon atoms are dark gray or purple.

Both CNT-PMC schemes (i.e., **PE Schemes 4** and **5**) have the same CNT volume fraction of 10%. In reality, the crystalline part of PE varies from merely 4% for very low density

polyethylene (VLDPE) to 82% for high density PE (HDPE) [129]. In this study, the semi-crystalline PE schemes initially contain 45% crystallinity and based on the final density, it changes to nearly 50% after the equilibration process at room temperature.

4.2.2 Polyvinyl chloride

The PVC scheme (Fig. 4.3a), is a pure and linear chain of commercial head-to-tail PVC which is composed of monomer vinyl chloride and has a molecular formula of $(C_2H_3Cl)_n$ with $n=400$.

4.2.3 Polystyrene

The PS scheme (Fig. 4.3b), is an atactic pure and linear chain composed of styrene monomer with molecular formula of $(C_8H_8)_n$ and head-to-tail direction with $n=200$.

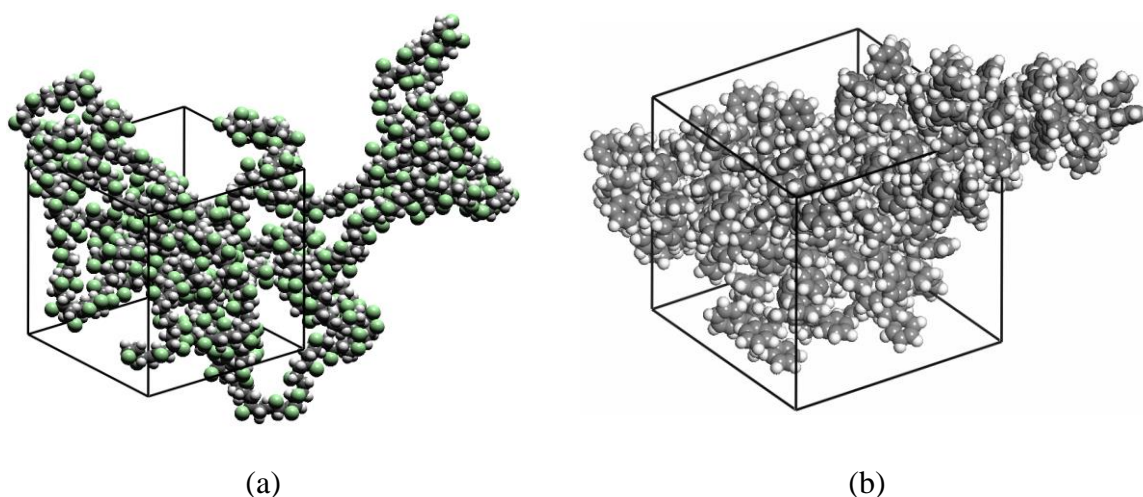


Fig. 4.3 Fully amorphous polymers: (a) polyvinyl chloride scheme, and (b) polystyrene scheme.

The Accelrys Amorphous Cell module [176] was used to generate random-walk polymer chains for amorphous part of each scheme. This package allows to generate random-walk

polymer chains based on the implementation of the method proposed by Theodorou-Suter [198] and Meirovitch [208]. In order to avoid free surface effect, periodic boundaries were applied to all schemes above.

4.3 Atomistic equilibration

The atomistic simulation was conducted using Materials Studio, Forcite modules [176]. The COMPASS force field [48], was used to model the atomic interactions. Molecular dynamics was employed to equilibrate the atomistic systems and to extract dilatometric graphs. Different methods were examined to construct initial homogeneous molecular structures without any artificial void, leading to the following procedure.

Each scheme above was initially generated with a low density of 0.2 g.cm^{-3} and then densified and cooled down in a stepwise manner with the aid of MD simulation. The cell dimensions were reduced by 2% for every 50 ps relaxation at 650 K, a temperature higher than its melting point, until the density reached that of the bulk polymer at room temperature. The atomic system was then equilibrated for 1 ns at the temperature of 650 K and the pressure of 1 Atm (i.e., under the NPT ensemble). Finally, the atomic system was cooled down with a step of 50 K for every 2.5 ns relaxation under the NPT ensemble, corresponding to the cooling rate of 20 K/ns, which was found sufficient to approach a stable average volume for dilatometric graph. The cell dimensions/volume were averaged for the final one nanosecond of each equilibrium process. The averaged cells were homogenized by equilibrating one more nanosecond under NVT ensemble, ready for stress analysis.

The quality of MD simulation was set to *Coarse* which is suitable for equilibration process as discussed in Sec. 3.9.1. The time step was 1 fs and the Brendsen algorithm [188] was employed to keep the temperature constant with a decay constant of 0.005 ps. The Parrinello and Rahman [196] algorithm was used to control the cell pressure. This method is able to change the cell dimensions and angles independently, keeping a homogeneous internal stress. The cell time constant was set to 0.5 ps which gives a reasonable fluctuation of pressure with dynamic stability.

Since the high temperature will destroy the crystalline structure of PE scheme 2~3, the amorphous PE chain surrounding the crystallinity were generated by the Amorphous Cell module of Materials Studio [176] and was equilibrated for 4 ns at room temperature to obtain stable volume/density. The equilibrated system was then cooled down stepwise from room temperature to 50 K or was heated up from room temperature to 500 K to obtain the transition point at the volume-temperature curve.

Recall that the pressure control method of Parrinello-Rahman is able to change the cell dimensions and angles independently to keep a homogeneous internal stress. However, especially in higher temperatures in which the polymers exhibit a liquid-like behaviour, the cell geometry is not stable and the cell might flatten after a few picoseconds of MD simulation. To overcome this problem, a script file was developed to keep the angles of cell to 90° constant.

A sample detailed volumetric relaxation process at different temperatures for the amorphous PE is shown in the Fig. 4.4, where the data points represent the averaged volumes in every 100 ps. To provide a better comparison with the experimental

dilatometric graphs in the following sections, the cell volume was normalized to specific volume. It is noted that at higher temperature, the system approaches an equilibrium state faster and a smaller equilibration time (e.g. 2 ns) is enough. Our studies on the PVC and PS revealed that for those materials, the relaxation time should be increased to 3.5 ns for reliable results.

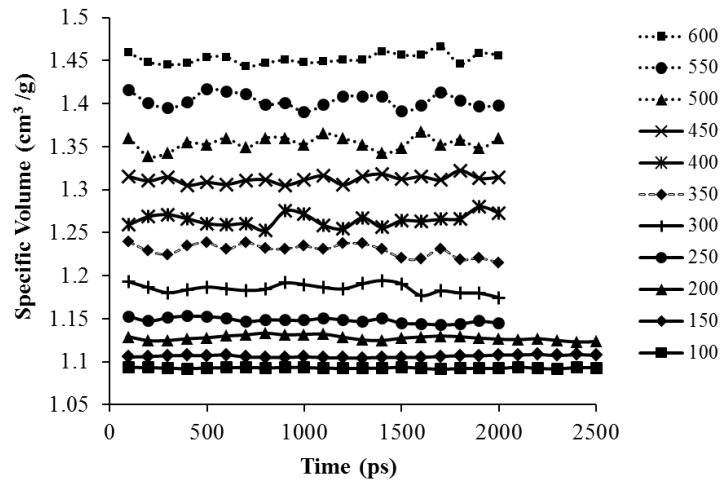


Fig. 4.4 Specific volume change of amorphous PE with n=400 against time in the equilibration process.

4.4 Stress-strain analysis

The generalized Hook's law for the stress-strain relation can be written as

$$\sigma_{lm} = C_{lmnk} \varepsilon_{nk} , \quad \text{Eq. 4.2}$$

where C_{lmnk} is the modulus tensor and $\sigma_{lm}, \varepsilon_{nk}$ are the stress and strain tensors, respectively. Since both the stress and strain tensors are symmetric, the Voigt notation (*i.e.*, $1 = xx, 2 = yy, 3 = zz, 4 = xz, 5 = yz, 6 = xy$) is convenient, which gives rise to

$$\sigma_i = C_{ij} \varepsilon_j \quad i, j = 1:6, \quad \text{Eq. 4.3}$$

where C_{ij} are the stiffness matrix components. The methods to calculate elastic constants from stiffness matrix are explained in some text books [209, 210]; however, the relations are shown in Appendix 1 for convenience.

In this study the static method based on the work of Theodorou and Suter [135] was implemented. They proved that, for glassy atactic polypropylene, the contribution of atomic configuration changes and the vibrational part of Helmholtz free energy is negligible. With these conditions, the changes of the free energy can be replaced by minimum potential energy changes in small deformation as

$$C_{ij} = \frac{1}{V} \frac{\partial A}{\partial \varepsilon_{ij}} \Big|_T = \frac{1}{V} \frac{\partial^2 U_{\min}^{pot}}{\partial \varepsilon_{ij}^2} \Big|_T, \quad \text{Eq. 4.4}$$

in which A is the free Helmholtz energy and U_{\min}^{pot} is the local minimum point of total potential energy. This relation is valid only for very small deformation, otherwise, the contribution of system configuration changes cannot not be ignored. To avoid numerical errors of the second order derivation of Eq. 4.4, it is preferred to use the first order derivative of Eq. 4.3. To evaluate the stiffness matrix by using Eq. 4.3., a prescribed small stain is applied to the cell and the total potential energy based on the MM relations was minimized. The average lm component of stress for each strain pattern is calculated using the static part of the Virial equation (Eq. 3.14) [211], *i.e.*,

$$\sigma_{lm} = \frac{1}{2V_t} \sum_{\alpha=1}^N \sum_{\beta=1}^N r_t^{\alpha\beta} f_m^{\alpha\beta}, \quad \text{Eq. 4.5}$$

where V_i is the total volume of the RVE, and $f_m^{\alpha\beta}$ and $r_i^{\alpha\beta}$ are respectively the interatomic force and distance between atoms α and β . In the MM analysis, only one component of the strains was applied while the others were set to zero. The strain of 0.2% was applied stepwise with an increment of 0.02%, during which the potential energy of the system was minimized. The stresses were then calculated using Eq. 4.5.

It is noted that, during MD equilibrium process, the cell dimensions are fluctuating and the atomistic structure of a frame of MD simulation may be in tension or compression which, statistically, is not a reasonable representative of bulk material for stress-strain analysis. To overcome this problem, the cell dimensions were averaged for the final one nanosecond of equilibrium process and then equilibrated one more nanosecond under NVT ensemble. The next problem arises during the energy minimization process; although the cell dimensions are averaged, the atoms are not located in their equilibrium position. For simple structures such as crystalline materials, a simple energy minimization through MM equations will make the corrections; however, due to the complicated polymer chain entanglement, simple energy minimization is only leads to a local minimum energy point. In other words, compared with an MD simulation, an energy minimization process with MM gives much less mobility to amorphous polymer chains to move towards their equilibrium position of a global minimum energy. However, the local residual stresses are relaxed after applying a small tensile strain. As a result, the first loading gives a nonlinear stress-strain curve. Thus, in this study, multiple loading and unloading cycles were applied to ensure a linear relationship between the stress and strain, and the linearity was obtained from the second cycle. A sample stress-strain curve for the PVC system is shown in Fig. 4.5, which exhibits

a linear elastic behaviour in the second cycle. In this study, the quality of MM simulation was set to ultra-fine for an accurate stress-strain analysis.

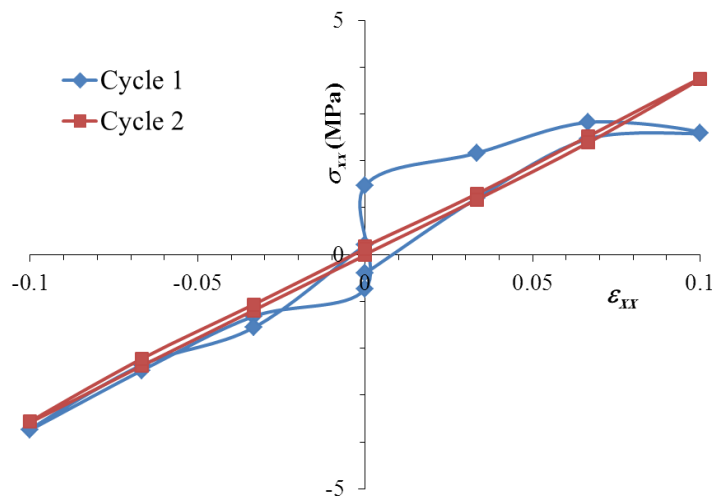


Fig. 4.5 Sample stress-strain relation of pure PVC (Scheme 2) in two cycles.

4.5 Results and discussion

In this section the physical properties such as density, glass transition, coefficient of thermal expansion and elastic properties of different schemes for PE, PVC and PS are discussed and the results are listed and compared with the experimental results i

Table 4.1.

4.5.1 Density

The densities of different schemes after MD equilibrium process are shown in

Table 4.1. The results show that the calculated density of 0.85 g.cm^{-3} for amorphous PE is close to the experimental results [129]; however, the density of semi-crystalline PE (i.e.

0.88 g.cm⁻³) is underestimated compared to the experimental results [129]. The discrepancy may arise due to the equilibrium process of the semi-crystalline PE performed under room temperature and low pressure of 1 atm. This process can preserve the crystalline part; however, it is not a seamless method to eliminate all vacancies which bring about a smaller density. The calculated density of amorphous PS and PVC are 1.05 and 1.42 g.cm⁻³, respectively, which is consistent with the experimental results [1, 212]. The results show that the proposed equilibrium method is more appropriate for the amorphous polymers.

4.5.2 Dilatometric graphs

In this section, the simulation results of dilatometric curves of different schemes for PE, PVC and PS are discussed. The volumetric coefficient of thermal expansions are calculated based on Eq. 4.6,

$$\alpha_v = \frac{1}{V} \left(\frac{\partial V}{\partial T} \right)_p \cong 3 \alpha_L, \quad \text{Eq. 4.6}$$

where α_v and α_L are volumetric and linear coefficients of thermal expansions, respectively.

Polyethylene: Based on the background of section 2.4, semi-crystalline PE has three turning points corresponding to three relaxation processes indexed by so-called α , β and γ [136]. Fig. 4.6 shows the dilatometric curve for the fully amorphous PE (PE scheme 1), which renders $T_g = 250$ K, consistent with the experimental result for the β transition [138] and the simulation result provided by Han. *et al.*[134]. For the semi- crystalline linear PE,

as shown in Fig. 4.6, the first transition occurs at 350 K corresponding to the α transition [138]. The second transition happens at 200 K which is between the experimental β and γ transition temperatures. In the case of the semi crystalline branched PE, the result shows almost the same behaviour as the semi-crystalline PE with linear chains, except that the γ transition is reduced to 150 K which is very close to the experimental γ transition temperature. α_v of the semi-crystalline scheme at room temperature is $6.11 \times 10^{-4} \text{ K}^{-1}$, which is also in excellent agreement with the experimental result of $6 \times 10^{-4} \text{ K}^{-1}$ for a PE with 50% crystallinity [129]. At the temperature of 500K, crystals were melted and the specific volumes of all the schemes approached the same value.

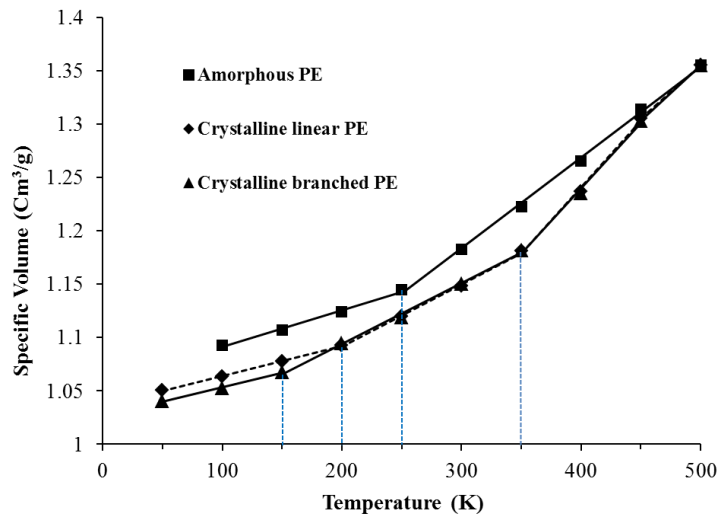
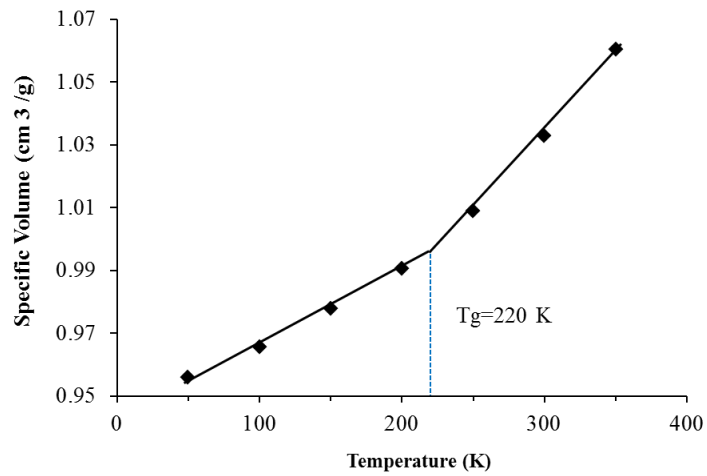


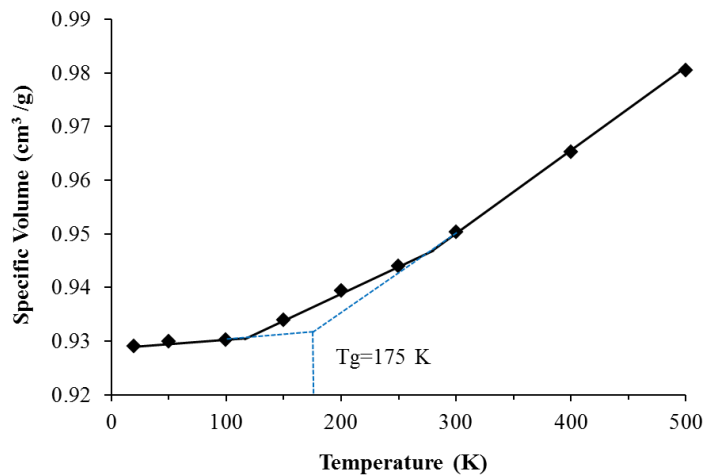
Fig. 4.6 Specific volume change of amorphous and semi-crystalline PE with temperature.

Fig. 4.7 shows the specific volume versus temperature of the CNT-PE composites. Compared with the fully amorphous PE, the glass transition temperatures of the composites are reduced to 220 K and 175 K for the short and infinitely-long CNT-composites, respectively. The α_v is also reduced in the whole temperature range between 50 K to 600

K as shown in Fig. 4.8. The α_v , at room temperature, for the short CNT-PMC and the infinitely-long CNT-PMC are $16.6 \times 10^{-4} \text{ K}^{-1}$ and $5.03 \times 10^{-4} \text{ K}^{-1}$ respectively which shows that, with a volume fraction of 10%, the α_v decreases by 36% for short CNT-PMC and by 80% for the infinitely-long CNT-PMC.



(a)



(b)

Fig. 4.7 Specific volume against temperature change. a) Short-capped CNT-composite b) Infinite CNT-composite.

It should be noted that the actual CNT-reinforced PE composite may not have such a significant change of α_v since the CNTs would not be as ideally dispersed as in the MD models. For the infinitely-long CNT-PMC, it can be seen that some amorphous PE chains arranged in the CNT direction during equilibrating process could form quasi-crystals as shown in Fig. 4.9. This could be the main reason for the similarity to the semi-crystalline PE in the sense that two distinct turning points appeared as shown in Fig. 4.7b.

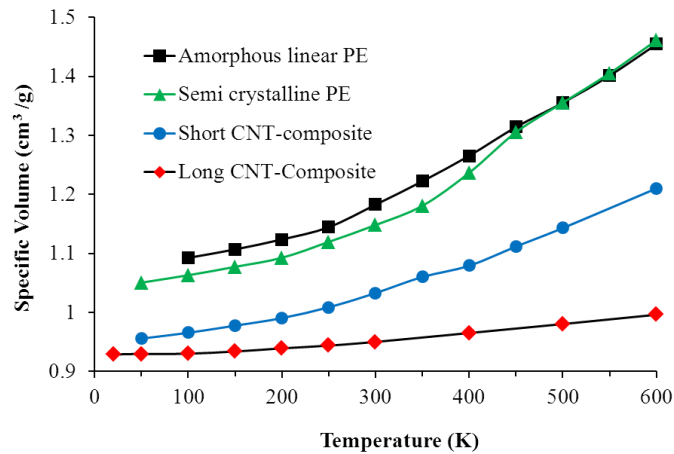


Fig. 4.8 Specific volume changes of different schemes.

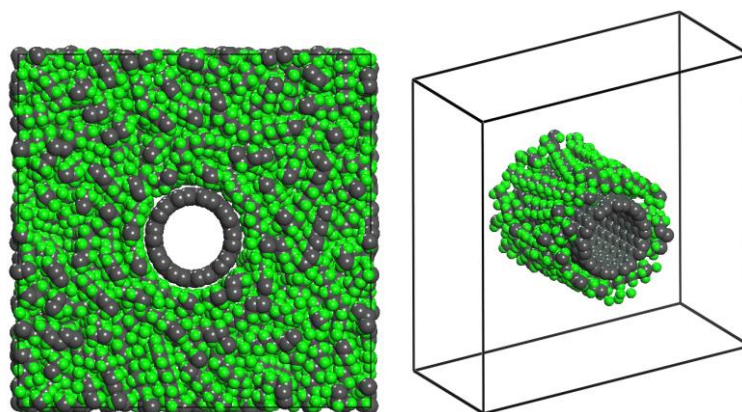


Fig. 4.9 Unidirectional morphology of PE around CNT.

It should be noted that, in reality, PE with linear chains contains at least a small percentage of crystalline PE, therefore no experimental results are available for amorphous PE at room temperature. Also, little (either theoretical or experimental) is available in the literature about the T_g of CNT-PE composite. To the best of our knowledge the only reference is Wei *et al.* [203], which employed the Brenner potential for intra-nanotube interactions. They used the Clarke *et al.*'s [213] potential for interactions within a polymer chain, and the vdW force field for polymer-nanotube interface. They claimed that both T_g and coefficient of thermal expansion are increased with the addition of CNTs, which is contrary to our result. In order to clarify this issue, their models and simulation parameters were repeated with the COMPASS force field. The T_g of the CNT-PE composition resulting from our simulation is still smaller than the pure amorphous PE.

Polyvinyl chloride: The dilatometric graph of Fig. 4.10 shows 361 K as the only transition point for the amorphous PVC, which is consistent with the experimental results of 353-380 K [1]. The calculated α_v in 300 K is $1.57 \times 10^{-4} \text{ K}^{-1}$ is consistent with the experimental results of $15.0 \times 10^{-4} \text{ K}^{-1}$ [212].

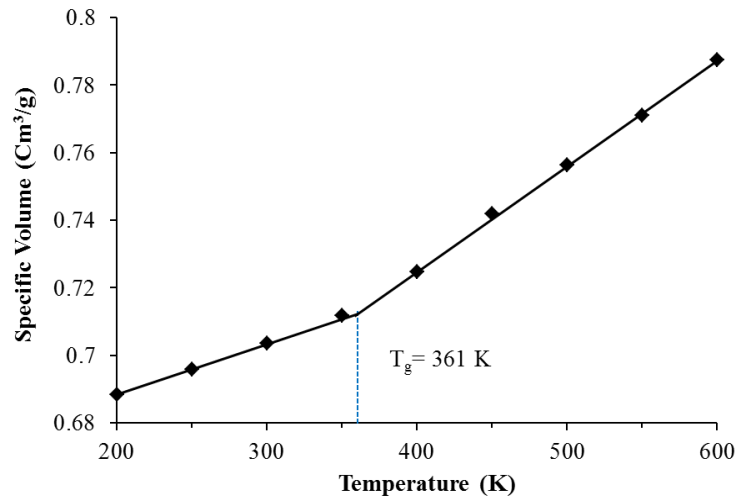


Fig. 4.10 Specific volume against temperature change of amorphous PVC.

Polystyrene: Based on the dilatometric graph of Fig. 4.11, $T_g = 379$ K for the amorphous PS scheme and the α_v is 2.12 K^{-1} which are quite close to the experimental results of $T_g = 373$ K and $\alpha_v = 1.7\text{-}2.1 \text{ K}^{-1}$ [1].

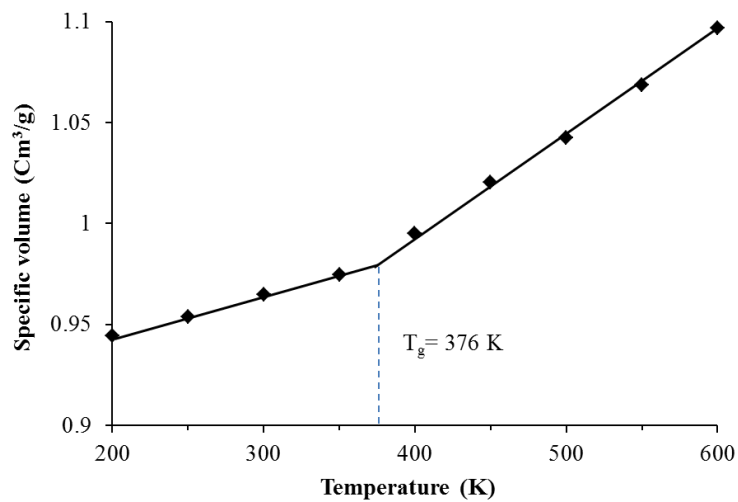


Fig. 4.11 Specific volume against temperature change of amorphous PS.

4.5.3 Stress-strain analysis

For the equilibrated pure PVC, the Young's moduli in three principal directions are $E_{xx} = 3.58$ GPa, $E_{yy} = 3.54$ GPa and $E_{zz} = 3.62$ GPa, which indicates the isotropy owing to the randomly distributed polymer chains. The average Young's modulus and Poisson's ratio are therefore 3.55 GPa and 0.34, respectively, agreeing well with the available experimental results [214, 215]. The MM results of

Table 4.1 show that both Young's modulus and Poisson's ratio of PS are close to the experimental results. The results above, indicate that the COMPASS force field and the MM simulations with the equilibrated atomic models can render good results for PVC and PS. However, the MM results of elastic constants of both the amorphous and the semi-crystalline PE show a major disagreement with the experimental results. Considering the excellent MD results for T_g and α_v of both amorphous and the semi-crystalline PE, one may conclude that the problem does not arise from the atomistic model and COMPASS force field; however, the applied static method based on the work of Theodorou and Suter [135] was established on the assumption that the contribution of atomic configuration changes and the vibrational part of Helmholtz free energy is negligible. The results show that this assumption is valid only for glassy and rigid polymers such as PVC and PS, however, experimental results of

Table 4.1 have been measured at room temperature which is much higher than T_g of PE. In this condition PE is not a glassy polymer, therefore static method cannot catch real configuration changes of PE chains giving rise to an overestimated stiffness.

Table 4.1 Physical parameters, obtained from atomistic simulations and compared to experimental results.

Material	Density ρ (g.cm ⁻³)		Glass transition temperature T_g (K)		Volumetric coefficient of thermal expansion ^a α (K ⁻¹) $\times 10^{-4}$		Young's modulus E (GPa)		Poisson's ratio ν	
	MD	Exp.	MD	Exp.	MD	Exp.	MM	Exp.	MM	Exp.
PVC	1.42	1.30-1.45 [212]	361	353-380 ^b [1]	1.57	1.5[212]	3.55	3.58 [214]	0.34	0.38 [215]
PS	1.05	1.04-1.065 [1]	376	373 [1]	2.3	1.7-2.1 [1]	3.42	3.2-3.4 [1]	0.32	0.325-0.33[1]
Amorphous PE	0.85	0.86 [129]	250	243-258 ^c [1]	7.17	4.5 ^d [129]	1.73	< 0.262 [129]	0.33	0.46 [216]
Semi-crystalline PE ^e	0.88	0.93 [129]	150	140-155 ^f [1]	6.11	6.0 [129]	3.93	0.315 [129]	0.323	0.46 [216]

^a T=300 K; ^b depends on polymerization temperature; ^b 50% crystallinity; ^d based on volumetric measurement; ^e β transition; ^f α transition;

4.6 Conclusion

This chapter aimed to consider the conditions under which atomistic simulations can predict the physical properties of thermoplastic polymers, and to clarify the effect of molecular morphology and CNT additives on the glass transition temperature of polymers. To this end, three sample thermoplastic polymers of PE, PVC and PS were examined. Density, glass transition temperature, volumetric coefficient of thermal expansion and elastic properties of different schemes were obtained. This chapter concludes that MD simulations using the COMPASS force field predict T_g , α_v and density of polymers in good agreement with the corresponding experimental measurements even for a small model a few nanometers in dimension; and that the static method using the COMPASS force field, well predicts the elastic properties of glassy polymers; however, it fails for soft polymers such as PE. The study revealed that the existing models of the fully amorphous PE cannot be used to study the actual PE properties since an actual PE is always semi-crystalline which should never be ignored in an MD simulation, and that different from an amorphous PE, the semi-crystalline PE scheme predicts two transition temperatures, all of which are in good agreement with experimental measurements. It was concluded that, although both the linear and branched semi-crystalline PE have the same α_v at room temperature, branches significantly change the T_g and should be taken into account in atomistic simulations, and that for the CNT-PMCs, an addition of only 10% of the infinitely-long CNTs can reduce the α_v by 80%, when it is under the condition that the CNTs are parallel and perfectly dispersed.

Chapter 5

Chapter 5

Elastic properties of free-standing SWCNTs and SWCNT-clusters

This chapter is based on: “*Elastic properties of single-walled carbon nanotube clusters: Dependence on hydrostatic pressure*” by S. Herasati and L.C. Zhang, published in *Computational Materials Science Volume 86,2014, Pages 93-98*.

5.1 Introduction

Understanding the elastic properties of CNTs is essential for characterizing their composites. Although extensive theoretical work has been done to determine the longitudinal Young’s modulus and Poisson’s ratio of free-standing CNTs, there is only a little on all five elastic parameters (e.g. [31, 87]) and further studies need to be provided. Since CNTs have the same role as the reinforcing solid fibres in a composite, they can be treated as solid fibres [31] with transversely isotropic properties; with this assumption there is no concern regarding to their wall thickness.

Due to the existence of a vdW gap between CNTs within their clusters, characterizing the elastic properties of CNT-clusters is more complicated than free-standing CNTs. In one sense the vdW gap between CNTs is similar to a soft material [118] with highly nonlinear elastic properties. Therefore, rationally, any external load (e.g. hydrostatic pressure) that changes the vdW gap distance can alter the elastic properties of CNT-clusters as well; however, this effect has not been studied thoroughly. Furthermore, in the case of non-

bonded CNT-composites, there is a vdW gap between the CNT wall and internal surface of the matrix, in a manner that is similar to the CNT-clusters (further discussion will be provided in Chapter 6), emphasizing the importance of characterizing the elastic properties of CNT-clusters in a variety of ambient conditions.

The aim of this chapter is to characterize the free-standing SWCNTs as a solid cylinder and to investigate the effect of hydrostatic pressure on the elastic properties of CNT-clusters composed of armchair SWCNTs of diameters below 2 nm. The simulations will be done using MM simulation.

5.2 Modelling

In this study, two schemes of free-standing SWCNT and SWCNT-cluster are studied. CNTs were generated using the Materials Studio visualizer [176]. The three generic carbon bonds (C3) were assigned to each carbon atom, which is used by the COMPASS force field. CNTs are aligned in Z direction and PBC are enforced along all the three directions. Therefore, they are a two-dimensional array of SWCNTs of infinite length.

5.2.1 Free-standing SWCNT

Free-standing armchair SWCNTs were constructed in a cubic cell including only one SWCNT as shown in Fig. 5.1. To avoid side effects from the neighboring SWCNTs, the lateral size of the cell was much greater than the vdW cutting radius. The initial dimensions of the simulation cell were $100 \times 100 \times 24.6 \text{ \AA}$.

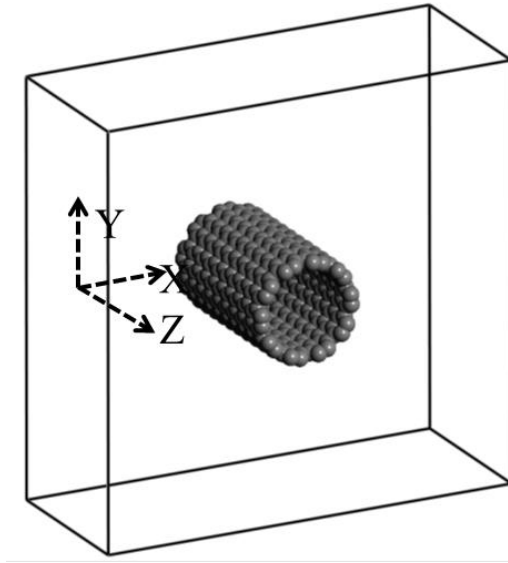


Fig. 5.1 Free-standing SWCNT scheme.

5.2.2 *SWCNT-cluster*

SWCNT-clusters have hexagonal configuration as shown in Fig. 5.2a. Using two-SWCNTs in a periodic cell (one SWCNT at the centre of cell and four quarters at the corners), a global hexagonal SWCNT-cluster can be generated as shown in Fig. 5.2b. Letting x-y be the plane of symmetry, the SWCNT-cluster can be approximated as a transversely isotropic material.

As a numerical forming process, the SWCNT-cluster was initially generated in a periodic cell of sufficiently large dimensions. In this case, the SWCNTs were far enough from each other such that the vdW attraction would be insufficient to hold them together. There are different ways to construct initial SWCNT-clusters for MD analysis. For example, when using the Parrinello-Rahman method, the equilibrium cell dimensions could be averaged for a few pico-seconds in atmospheric pressure. Alternatively, MM could be used, with which

an external pressure is necessary to push the SWCNTs to their globally equilibrium positions. This pressure should be big enough as otherwise the SWCNTs might be trapped in a position with a local minimum energy. In this study, a hydrostatic pressure of 100 MPa was applied to compress the SWCNTs and form the SWCNT-cluster numerically, during which the overall energy was minimized to obtain the most compact hexagonal configuration (Fig. 5.2b). It should be noted that the hydrostatic pressure of 100 MPa is much less than the collapse pressure of SWCNTs, but is enough to obtain a global optimum structure of the SWCNT-clusters. The pressure was then reduced to the atmospheric pressure stepwise associated with the energy minimization in every step to lead to the final equilibrium configuration.

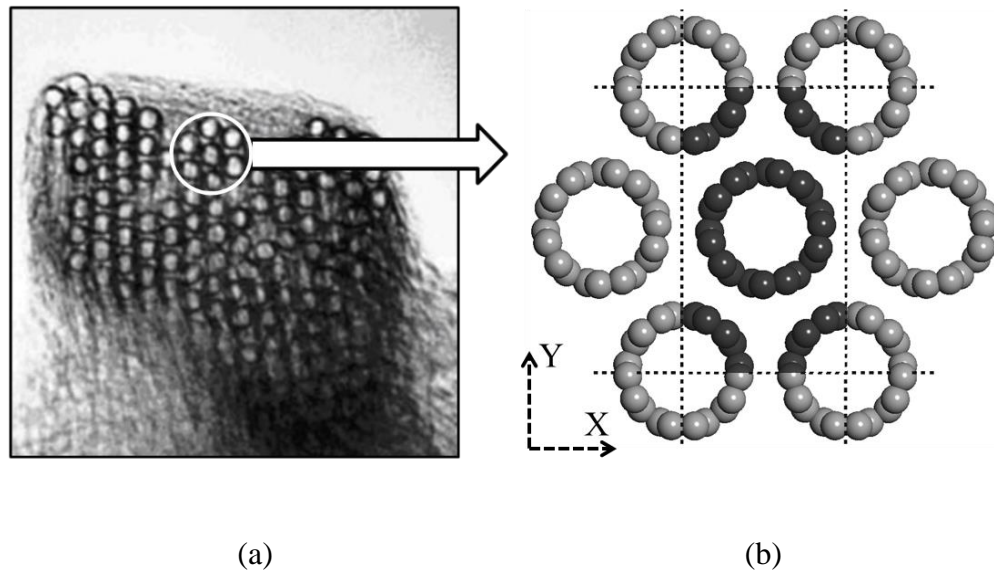


Fig. 5.2 The concept of an SWCNT-cluster: (a) the SEM image of some SWCNT-clusters [110], and (b) an SWCNT-cluster scheme in a periodic cell, involving image atoms out of cell.

As a numerical forming process, the SWCNT-cluster was initially generated in a periodic cell of sufficiently large dimensions. In this case, the SWCNTs were far enough from each

other such that the vdW attraction would be insufficient to hold them together. There are different ways to construct initial SWCNT-clusters for MD analysis. For example, when using the Parrinello-Rahman method, the equilibrium cell dimensions could be averaged for a few pico-seconds in atmospheric pressure. Alternatively, MM could be used, with which an external pressure is necessary to push the SWCNTs to their globally equilibrium positions. This pressure should be big enough as otherwise the SWCNTs might be trapped in a position with a local minimum energy. In this study, a hydrostatic pressure of 100 MPa was applied to compress the SWCNTs and form the SWCNT-cluster numerically, during which the overall energy was minimized to obtain the most compact hexagonal configuration (Fig. 5.2b). It should be noted that the hydrostatic pressure of 100 MPa is much less than the collapse pressure of SWCNTs, but is enough to obtain a global optimum structure of the SWCNT-clusters. The pressure was then reduced to the atmospheric pressure stepwise associated with the energy minimization in every step to lead to the final equilibrium configuration.

5.3 Atomistic simulation

The atomistic simulation was conducted using Materials Studio, Forcite modules [176]. The COMPASS force field [48], was used to model the atomic interactions. Because this force field covers both the valance and non-bonding energy terms, it is more reliable for investigating the mechanical properties of SWCNT-clusters. The static part of virial equation (Eq. 4.5) was used to calculate pressure and stress components in the MM simulation.

5.3.1 Collapse pressure of SWCNT-cluster

To obtain the collapse pressure of an SWCNT-cluster, the external pressure was increased stepwise with an increment of 100 MPa. The total energy was minimized in each pressure state to obtain the new cell dimensions and SWCNT configuration. Any sudden decrease in the cell volume indicated a ‘phase’ transformation or collapse pressure. In this study, the collapse pressure of free-standing SWCNT is not considered. In the case of an SWCNT-cluster, the external pressure is applied to each SWCNT from its six surrounding SWCNTs through vdW interactions. Although the external pressure is not applied uniformly to the central SWCNT, it is close to the collapse pressure of free-standing SWCNT pressure.

5.3.2 Elastic moduli of SWCNT-clusters

As a transversely isotropic material, the SWCNT-cluster has five elastic constants of longitudinal and transverse Young’s moduli (E_{zz} , E_{xx}), in-plane and out-of-plane Poisson’s ratio (ν_{zx} , ν_{xy}) and out-of-plane shear modulus (G_{zx}). The SWCNT-clusters can be treated as solid bulk material by the same method as explained in section 4.4. However, the Young’s moduli and Poisson’s ratio are obtained through numerical simple tensile tests. To obtain the Young’s moduli and Poisson’s ratio in different pressure states, in each pressure state, a total strain of 0.2% (either in compression and tension) was applied in one direction stepwise with an increment of 0.02%, during which the potential energy of the system was minimized. The periodic cell dimensions in two other directions were allowed to change during the energy minimization, which helps keep a constant principal stress, quantitatively equal to the external pressure in those directions (the same as a simple tensile test in a

hydrostatic pressure condition), while enabling the calculation of the transverse strain and the Poisson's ratio. To obtain G_{zx} , a total of 1% pure shear strain was applied with potential energy minimization. After each strain increment, the stresses were calculated by using Eq. 4.5, and the Young's moduli and shear modules were calculated from the stress-strain relation.

Multiple loading and unloading cycles were applied to avoid local points of minimum potential energy and to ensure the linearity of the stress-strain relationship. It should be noted that the vdW interaction is non-linear, which gives rise to the non-linear behaviour of the SWCNT-cluster under transversal large strain. It is also worth noting that under a small strain of 0.2%, the error of linearity estimated from the vdW interaction of COMPASS force field (9-6 Lennard-Jones) was less than 2%.

5.3.3 Elastic moduli of free-standing SWCNTs

A free-standing SWCNT has transversely isotropic properties. In this study, only armchair SWCNTs (5, 5), (10, 10), (15, 15) and (20, 20) are characterized to be used for the composite models in Chapter 7. SWCNTs are assumed as solid cylinders with the average radius of R_{CNT} . Three numerical experiments were carried out to extract five elastic constants: (i) using the free-standing scheme Fig. 5.1, the longitudinal tensile/compression test in the Z direction was performed to extract the longitudinal Young's modulus (E_{zz}) and the radial Poisson's ratio ($\nu_r = \nu_{zx} = \nu_{zy}$). A total strain of 0.2% (compression and tension) was applied stepwise with an increment of 0.02%. The potential energy of the system was minimized in every step. Both the longitudinal Young's modulus and the transverse strain

of SWCNT are then calculated;(ii) using the free-standing scheme, the torsion test was performed to obtain the shear modulus $G_{yz} = G_{xz}$ [31]; and (iii) using the CNT-cluster (Fig. 5.2b), the uniaxial transversal tension-compression test along either X or Y axis was performed to obtain the transverse Young's modulus $E_{xx} \cong E_{yy}$ and the Poisson's ratio ν_{xy} . In this case, a transverse small strain (0.3%) was applied on the periodic cell of the CNT-cluster and the stress of the central SWCNT was calculated using Eq. 4.5 after energy minimization. It is noted that the transverse loads were actually applied by surrounding SWCNTs through vdW interactions to the central SWCNT and the true normal strains of the SWCNT along the X and Y directions are different from the strain (i.e., 0.3%) applied to the cell boundary. Assuming an ellipsoid deformation of the cross-section of the SWCNT, the radii of the SWCNT in X and Y directions before and after loading were measured to calculate the transverse strains.

In the torsion test *ii*, one end of SWCNT is fixed and a rotational shear strain of 0.2% was applied to the next end. After an energy minimization, the energy change (ΔU) is used to calculate the shear modulus through

$$G_{yz} = G_{xz} = \frac{2 \Delta U}{\phi^2 J_{Solid}} L_0, \quad \text{Eq. 5.1}$$

where J_{Solid} and ϕ are the polar moment of inertia of the equivalent solid cylinder and torsional angle respectively and L_0 is the effective length of SWCNT.

5.4 Results and discussion

5.4.1 Collapse pressure of SWCNTs

The pressure-volume behaviour of some SWCNT-clusters is shown in Fig. 5.3a, where the volumes were normalized by the volume of the corresponding cluster at zero pressure. The result shows that the normalized volume of all the SWCNT-clusters follow the same pattern before reaching the collapse pressure, P_c , at which the volume falls suddenly. The values of the P_c for SWCNTs of different diameters are shown in Fig. 5.3b, showing an exponential relationship of

$$P_c = 60.0 e^{(-0.174 D_{CNT})} \text{ (GPa) }, \quad \text{Eq. 5.2}$$

in which D_{CNT} is the SWCNT diameter.

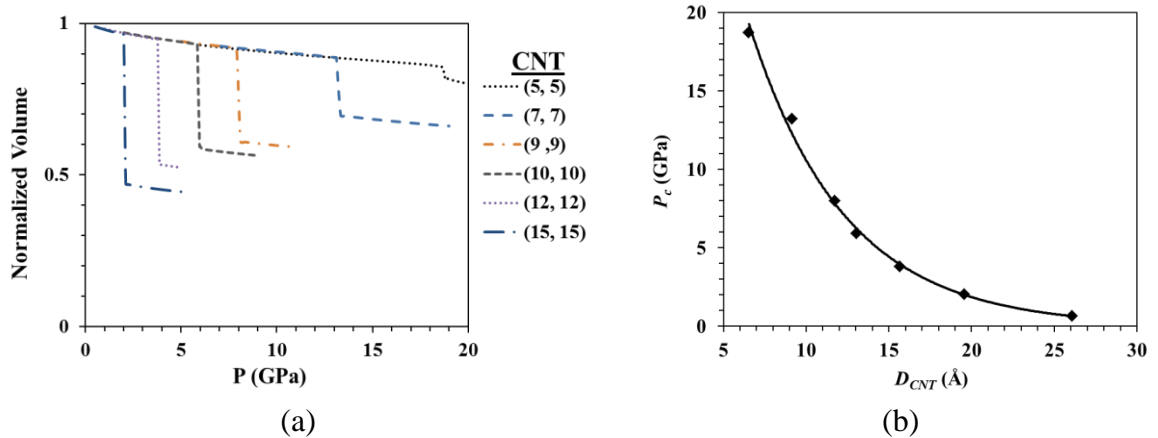


Fig. 5.3 Collapse pressure of some SWCNT-clusters: (a) variation of the normalized cell volume with pressure, and (b) variation of the collapse pressure with SWCNT diameter.

An SWCNT often has a diameter below 20 Å. Based on the results of Fig. 5.3, the collapse pressure for $D_{CNT} = 20$ Å, *i.e.*, SWCNT (15, 15), is $P_c = 2$ GPa. This is in consistent with the reports on the structural distortion/transition of SWCNTs [123]. It should be noted that the maximum external pressure of 2 GPa is much smaller than the external pressure needed to change the material phase by making new bonds [217]. For example, it has been reported that even at a high temperature of 1,800 K, a pressure of 14.5 GPa is required to initialise a phase transformation [218]. This study will focus on the effect of pressure less than 2 GPa on the elastic properties of SWCNT-clusters, a phase transformation will not take place and does not need to be considered.

5.4.2 Elastic moduli of SWCNT-clusters

Now consider the variation of the elastic moduli of the SWCNT-clusters of 11 diameters from SWCNT (5, 5) to SWCNT (15, 15) in the pressure range from 0 to 2 GPa. For the sake of a clear visualization, Fig. 5.4 gives the longitudinal and transverse Young's moduli of SWCNTs of only six different diameters.

To explain each elastic property in detail, let us define three distinct regimes: (1) that with the absolute value of an elastic property at zero pressure, (2) that with a relative value ranging from 0 to 2000 MPa, and (3) that with a relative value at 2000 MPa. For example Fig. 5.5a shows the three distinct regimes of the longitudinal Young's modulus under the absolute zero pressure (E_{zz-0}). Fig. 5.5b gives the change of the elastic properties of various clusters relative to E_{zz-0} , *i.e.*, ΔE_{zz} , when pressure varies to 2000 MPa. In Fig. 5.5a, $\Delta E_{zz-2000}$

denotes the variation of the elastic properties under the pressure of 2000 MPa relative to that at zero pressure, *i.e.*, $E_{zz-2000} = E_{zz-0} + \Delta E_{zz-2000}$.

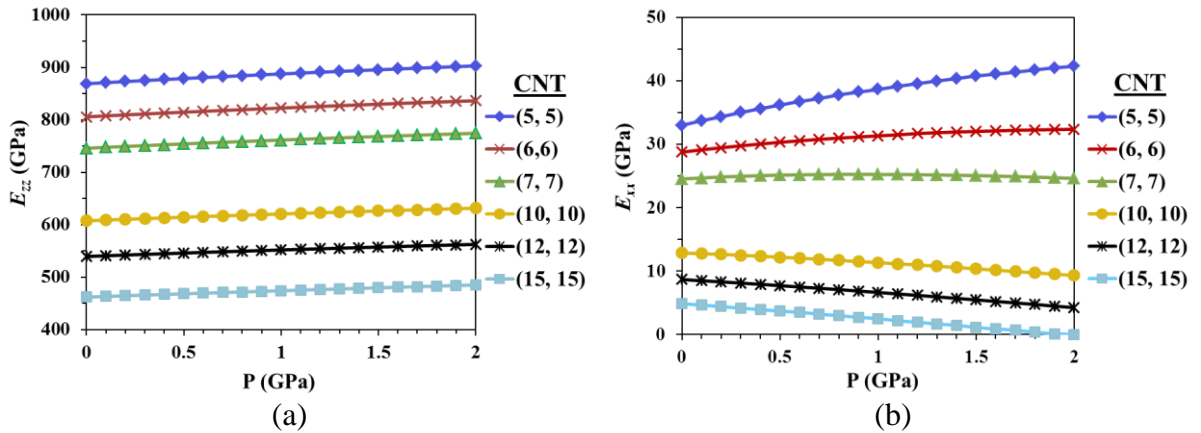


Fig. 5.4 Variation of elastic properties with the external pressure applied when the SWCNT diameter changes: (a) longitudinal Young's modulus, and (b) transverse Young's modulus.

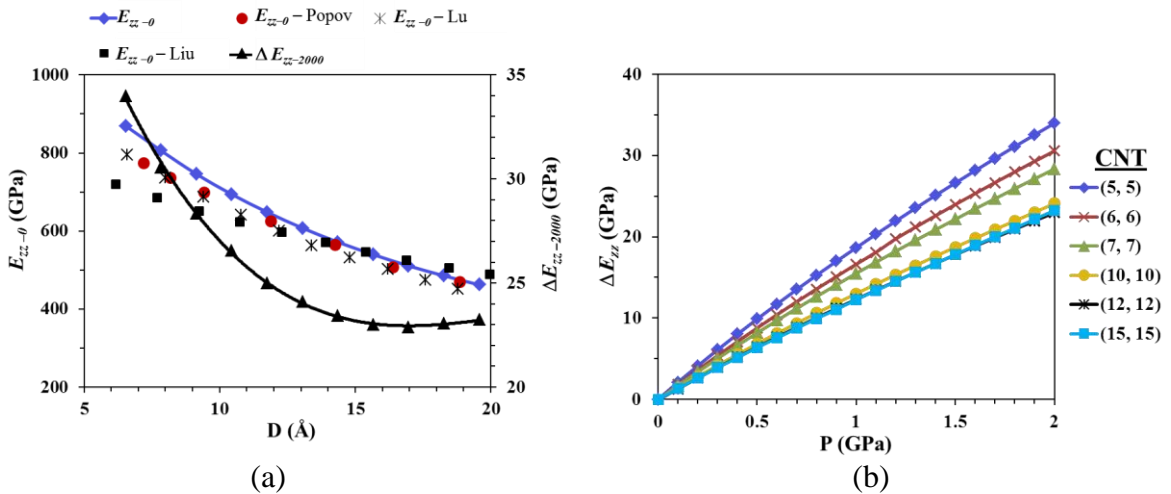


Fig. 5.5 (a) Longitudinal Young's modulus, E_{zz} , at the absolute zero pressure compared with the results of Lu [74], Popov *et al.* [118] and Liu *et al.* [119], and ΔE_{zz} at 2000 MPa when the SWCNT diameter varies, and (b) ΔE_{zz} as a function of pressure.

Fig. 5.5a shows that E_{zz-0} decreases from 870 GPa for SWCNT (5, 5) to approximately half of that for SWCNT (15, 15). Its variation is in good agreement with that obtained by Lu *et*

al. [74] which used an empirical force-constant model, and that given by Popov *et al.* [118] based on a lattice dynamics model. However, the results of Liu *et al.* [119] shows a discrepancy especially for smaller diameters. It can be seen that if the wall thickness t of the SWCNT is assumed to be a constant, then the longitudinal Young's modulus of a free-standing SWCNT as a thin shell cylinder does not change significantly with its diameter [219]. The present results demonstrate, however, that when an SWCNT-cluster is treated as a solid material, a larger SWCNT radius leads to a more empty space in the SWCNT-cluster and hence should have a smaller equivalent modulus. Fig. 5.5b shows that E_{zz} increases almost linearly for all the SWCNTs when pressure rises. Overall, the percentage of E_{zz} variation is less than 5, and thus is probably negligible in engineering applications.

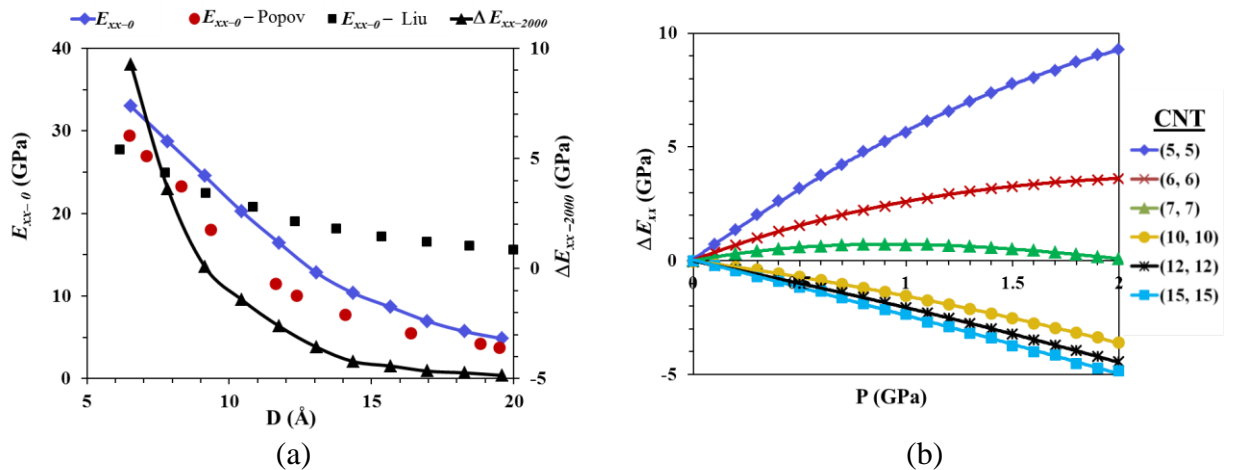


Fig. 5.6 (a) Variation of the transverse Young's modulus, E_{xx-0} and $\Delta E_{xx-2000}$, and (b) ΔE_{xx} as a function of pressure.

Fig. 5.6 shows the transverse Young's modulus, E_{xx} , in a variety of pressure states and SWCNT diameters. Fig. 5.6a shows that the transverse Young's modulus at zero pressure, E_{xx-0} , decreases from 33 GPa for SWCNT (5, 5) to 4.9 GPa for SWCNT (15, 15). This is

close to the results reported by Popov *et al.* [118]. However, Liu *et al.* [119] shows a big discrepancy especially for a diameter of SWCNTs. Because of the weak non-bonded vdW interaction and ovalization of the SWCNTs, SWCNT-clusters show much less rigidity in the transverse direction compared to E_{zz-0} .

Fig. 5.6b shows that when the SWCNT diameter is small, ΔE_{xx} increases with raising the hydrostatic pressure. However, the opposite occurs when the SWCNT diameter is large. SWCNT (7, 7) seems to be the turning diameter at which E_{xx} remains almost a constant when the external pressure varies. This could be understood if we examine the variation of the strain energy of SWCNT-clusters. The relation of strain energy and Young's modulus for an isotropic material under a simple tension is,

$$U = \frac{1}{2} V E \varepsilon^2 = \frac{1}{2} V \sigma \varepsilon, \quad \text{Eq. 5.3}$$

where U , V , E and ε are strain energy, volume, Young's modulus and strain, respectively. The SWCNT-cluster however is not an isotropic material. Therefore, Eq. 5.3 should be applied for each pair of atoms separately, which gives rise to the static part of the virial equation (Eq. 4.5). To study the strain energy change qualitatively as a function of pressure, let us assume a uniform strain on all the bonds between constituent particles. Then according to Eq. 5.3, the overall Young's modulus is proportional to the strain energy per unit cell volume, and could be separated to two bond and non-bond strain energies. As vdW is the only non-bonded interaction in this study, the strain energy and Young's modulus are linked by

$$E = C_B \frac{U_B}{V} + C_{vdW} \frac{U_{vdW}}{V} \quad \text{Eq. 5.4}$$

where U_B and U_{vdW} are bond and vdW strain energies, respectively. The two coefficients, C_B and C_{vdW} , are functions of strain and volume of the corresponding region associated with the bond and vdW interaction. They could be obtained using the same method for virial stress determination. Fig. 5.7 shows the variation of bond and vdW (non-bond) strain energies for SWCNTs (5, 5), (7, 7) and (10, 10) in different pressure states under a constant transversal strain of $\varepsilon = 0.2\%$, where the strain energies per unit cell volume have been normalized by their energy values at zero pressure. The figure shows that in the case of SWCNT (5, 5), the bond energy almost remains constant with the pressure variation; while the vdW energy increases significantly, giving rise to a bigger Young's modulus at a higher pressure. In contrast, the vdW energy of SWCNT (10, 10) increases only at a lower pressure and reaches a plateau at a certain higher pressure. The bond energy reduces with the pressure rise, causing a reduction of the Young's modulus. In the case of SWCNT (7, 7), the vdW energy increases with the pressure rise; but the bond energy reduces, which keeps the total energy almost constant and brings about a constant Young's modulus as shown in Fig. 5.6b.

It is a fact that the result of the vdW and the SWCNT structural deformation determines the variation of E_{xx} . The above results demonstrate that due to the intrinsic rigidity of the SWCNTs of smaller diameters, their SWCNT-clusters have greater resistance to ovalisation, leading to a greater rigidity in the transverse direction. Thus in this case the dominant parameter is the vdW interaction. When the external pressure reduces the

vdW distance, the rigidity of the system is increased. For the SWCNTs of bigger diameters, on the other hand, the SWCNTs can be flattened more easily under an external pressure, leading to a smaller transversal rigidity. Fig. 5.6b shows that the variation of E_{xx} under the pressure of 2000 MPa ($\Delta E_{xx-2000}$) is more sensitive to the SWCNT diameter.

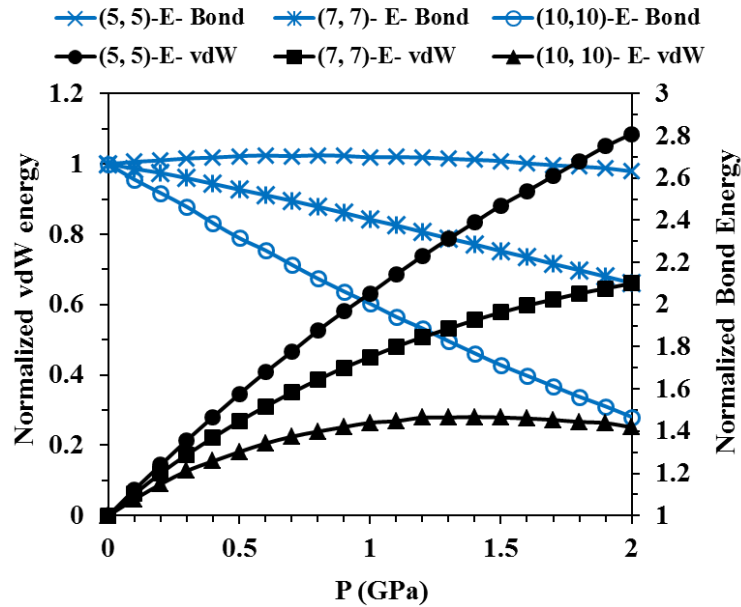


Fig. 5.7 Variation of normalized vdW and bond portions of strain energy with pressure.

Fig. 5.8a shows that the out-of-plane Poisson's ratio under zero pressure, ν_{xy-0} , increases from 0.64 for SWCNT (5, 5) to 0.94 for SWCNT (15, 15), which is consistent with the findings of Popov *et al.* [122] (but not those of Liu *et al.* [119]). The out-of-plane Poisson's ratio, ν_{xy} , approaches 1.0 as the diameter approaches 20 Å, indicating that although the cross-section of a larger SWCNT flattens, its circumference does not change [122]; however, for rigid small SWCNTs, the dominant parameter is vdW gap which is reduced without a sensible flatness of SWCNTs. Fig. 5.8b shows that the variation of ν_{xy} , i.e., $\Delta\nu_{xy}$, is almost linear. Fig. 5.8a also shows that $\Delta\nu_{xy-2000}$ for smaller SWCNTs are more sensitive

to pressure rise. For bigger SWCNTs, ν_{xy} at 2000 MPa, *i.e.*, $\nu_{xy-2000}$, is very close to one. This is probably due to the fact that the pressure becomes very close to their collapse pressure. In the case of SWCNT (15, 15), for example, $\nu_{xy-2000} = \nu_{xy-0} + \Delta\nu_{xy-2000} = 0.944 + 0.056 = 1.000$.

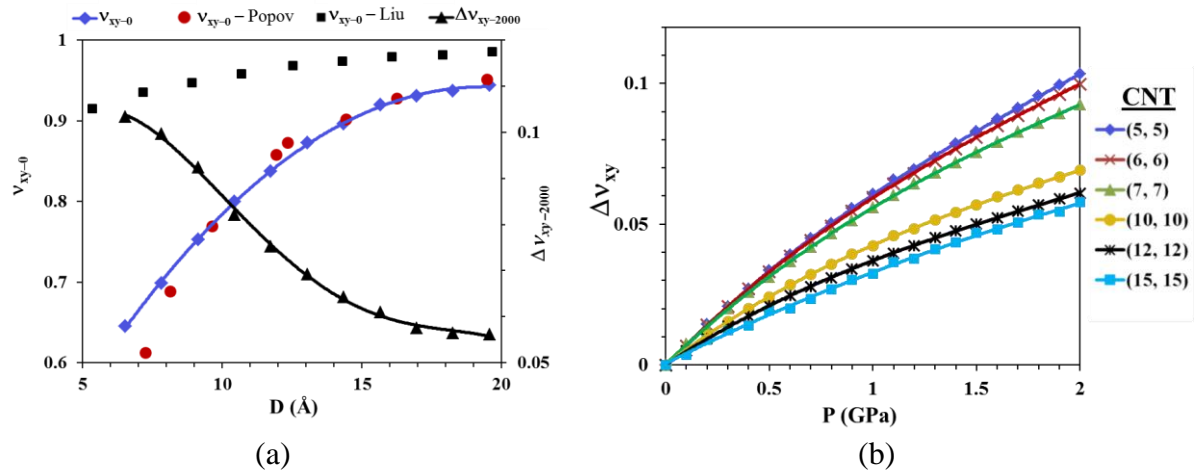


Fig. 5.8 (a) Out-of-plane Poisson's ratio, ν_{xy} , and (b) $\Delta\nu_{xy}$ as a function of pressure.

Fig. 5.9a shows that the in-plane Poisson's ratio ν_{zx-0} increases from 0.18 for SWCNT (5, 5) to 0.25 for SWCNT (15, 15). However, Popov *et al.* [122] and Liu *et al.* [119] reported a different trend with a smaller ν_{zx-0} for the whole range of SWCNT diameters. The discrepancy could be raised by the difference between radial Poisson's ratios of free-standing SWCNT in those methods. For example, Popov *et al.* [219] reported that the radial Poisson's ratio approaches 0.21 for relatively large SWCNT radius, while our analysis shows a value of 0.28 (in agreement with that of Lu *et al.* [74]). Fig. 5.9b shows that the diameter change of SWCNTs does not alter the variation trend of Poisson's ratio. Furthermore, $\Delta\nu_{zx-2000}$ (Fig. 5.9a) of a SWCNT of a diameter ranging from 10 to 13 Å varies only slightly.

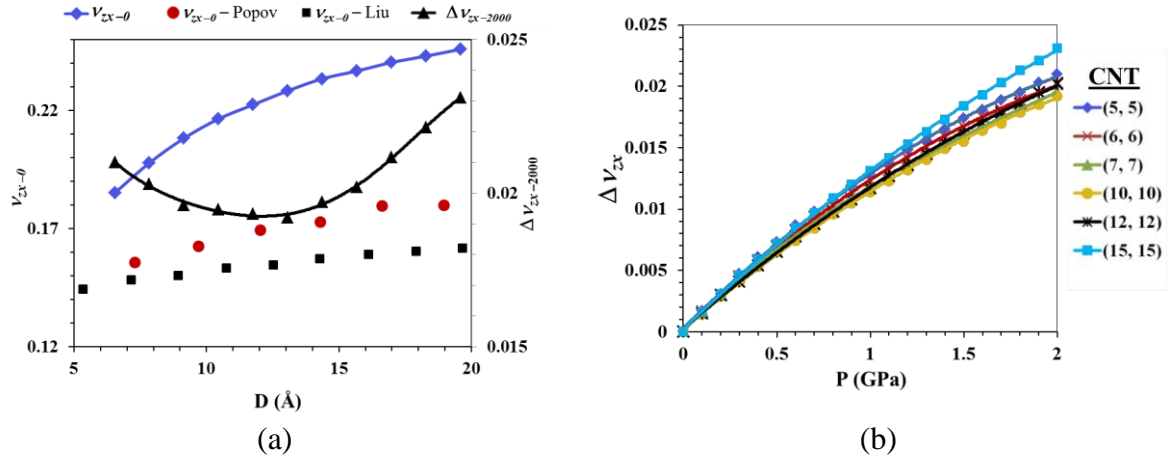


Fig. 5.9 (a) Variation of the in-plane Poisson's ratio, v_{zx} with SWCNT diameter, and (b) Δv_{zx} as a function of pressure.

Fig. 5.10a shows that the out-of-plane shear modulus at zero pressure, G_{zx-0} , is approximately equal to 0.8 GPa for the discussed range of SWCNTs, which is close to the experimental results of 1.1~2.0 GPa reported by Lasjaunias *et al.* [220] and of 1 GPa reported by Salvetat *et al.* [94]. It seems that G_{zx-0} is a very weak function of SWCNT diameter. To the best of our knowledge, there are no theoretical results on G_{zx} in the range of CNT diameter for comparison. Liu *et al.* [119] estimated that the upper and lower bounds are 2.2 and 0.25 GPa, respectively, and that they do not vary with CNT diameter which is consistent with our findings. Fig. 5.10b shows that G_{zx} increased linearly with the pressure rise. The variation of $\Delta G_{zx-2000}$ (Fig. 5.10a) shows that $G_{zx-2000} = G_{zx-0} + \Delta G_{zx-2000}$ is approximately double that of G_{zx-0} which is the elastic property most affected by pressure change.

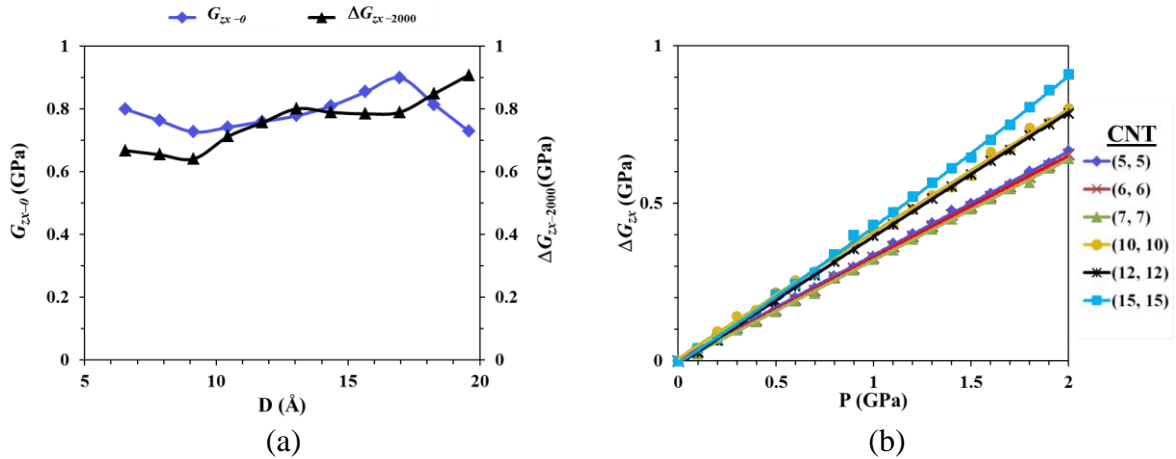


Fig. 5.10 (a) Variation of out-of-plane shear modulus, G_{zx} , and (b) ΔG_{zx} as a function of pressure.

5.4.3 Elastic moduli of free-standing SWCNT

Five elastic properties of SWCNTs in a range of SWCNT radius (R_{CNT}) are listed in Table 5.1. The results show that the longitudinal Young's modulus (E_{zz}) of equivalent solid SWCNT is reduced remarkably with the increase of the SWCNT radius. However, longitudinal Young's modulus of SWCNTs should be in a narrow range as explained in Sec. 2.3.2. The discrepancy arises when an SWCNT is treated as a solid fibre rather than a thin-walled shell. Therefore, a larger CNT radius leads to a more empty space and a smaller equivalent modulus. If the wall thickness t of the CNT is assumed to be a constant, the Young's modulus of the thin shell SWCNT reduces proportionally with $2t/R_{CNT}$ for equivalent solid SWCNT and theoretically approaches zero when the CNT radius approaches infinity. For example, the longitudinal Young's modulus of SWCNT (20, 20) as a solid cylinder is 553.12 GPa. Assuming a thickness of 3.4 Å for SWCNT, the equivalent Young's modulus is 1.064 TPa which is consistent with the experimental [92, 101] and theoretical results [74, 76]. Both E_{xx} and G_{yz} are decreased with increasing the SWCNT

radius, which is partly due to the empty volume fraction as explained above. ν_{zy} is 0.26 for SWCNT (5, 5) and 0.28 for other SWCNTs which is the same as that obtained by Lu [74] from empirical potentials and is close to the result from tight-binding (TB) methods [75]. In contrast to the SWCNT-crystals, ν_{xy} of free-standing SWCNTs are close to one even for small diameters showing that, under lateral load, free-standing SWCNTs are flattened and their circumferences do not change [122]. Due to exclusion of vdW gap, the results of Table 5.1 for free-standing SWCNTs are obviously different from those results of SWCNT-clusters especially for transverse Young's modulus and shear modulus.

Table 5.1 Five elastic properties of free-standing SWCNT as a solid cylinder.

SWCNT	$R_{CNT}(\text{\AA})$	Elastic modulus (GPa)			Poisson's ratio	
		E_{zz}	E_{xx}, E_{yy}	G_{yz}, G_{xz}	ν_{zy}, ν_{zx}	ν_{xy}
(5,5)	3.38	1968.52	77.68	383.52	0.26	0.95
(10,10)	6.58	1028.86	32.94	366.67	0.28	0.98
(15,15)	9.83	688.63	10.41	104.85	0.28	0.99
(20, 20)	13.09	553.12	2.29	75.36	0.28	0.99

5.5 Conclusions

In this chapter, with the aid of MM, all five independent elastic properties of armchair SWCNT-clusters at room pressure and under hydrostatic pressure were considered. Furthermore, elastic properties of free-standing SWCNTs were characterized. The study found that the collapse pressure of SWCNT-clusters varies exponentially with increasing the SWCNT diameter, and that the elastic properties of SWCNT-clusters are not only a

function of the SWCNT diameter, but are also dependent strongly on the hydrostatic pressure. Except the transverse Young's modulus, all other elastic quantities increase with the pressure rise. However, depending on the SWCNT diameter, the variation of the transverse Young's modulus is not monotonic. There is a critical SWCNT diameter at which the transverse Young's modulus remains almost constant, within a range of hydrostatic pressure. The out-of-plane shear modulus is nearly a constant for different SWCNT diameters and is the elastic property most influenced by hydrostatic pressure. The study concludes that the out-of-plane Poisson's ratio of free-standing SWCNTs for all ranges of diameters of SWCNTs is close to one.

Chapter 6

Chapter 6

Elastic properties of nano-representative volume element: A three-phase model

This chapter is based on: “A new method for characterizing the interphase regions of carbon nanotube composites” by S. Herasati, H.H. Ruan and L.C. Zhang, *International Journal of Solids and Structures* Volume 51, 2014, Pages 1781-1791.

6.1 Introduction

A cubic NRVE model of a CNT-PMC is a fundamental element for a multiscale analysis, which can be characterized with the aid of atomistic simulation. However, atomistic simulation of such NRVE is a time consuming process. A rational solution is to characterize all regions of NRVE separately to implement them in a continuum based model. Geometrically, a cubic NRVE of a non-bonded CNT-PMC involves four regions, the CNT, the vdW gap, the dense matrix interphase and the bulk matrix.

The purpose of this chapter is to characterize the NRVE with the aid of atomistic simulation and developing methods to characterize different regions of the NRVE. Using SWCNT-reinforced PVC as an example, this chapter presents a new technique to characterize interphase regions. The fundamental issue that will be clarified is the reliable characterization of the ESF and the independent determination of the dense interphase properties. The method developed will be examined with a three-phase NRVE continuum FE model to account the ESF, the interphase and the matrix.

6.2 Modelling

In this study, a composite with the SWCNT surrounded by a PVC chain is established, as shown in Fig. 6.1a. The diameter of the SWCNT was changed from 6.76 Å of the SWCNT (5, 5) to 26.18 Å of the SWCNT (20, 20), which is a typical range for SWCNTs. Since the aspect ratio of a typical SWCNT is usually around 1,000 or more, it is reasonable to assume that the SWCNT is infinitely long and can be represented by the PBCs in the Z-direction. It is therefore rational to assume that the longitudinal strains in both the SWCNT and the PVC are the same. The PVC in the current composite is a random-walk chain with $n = 400$.

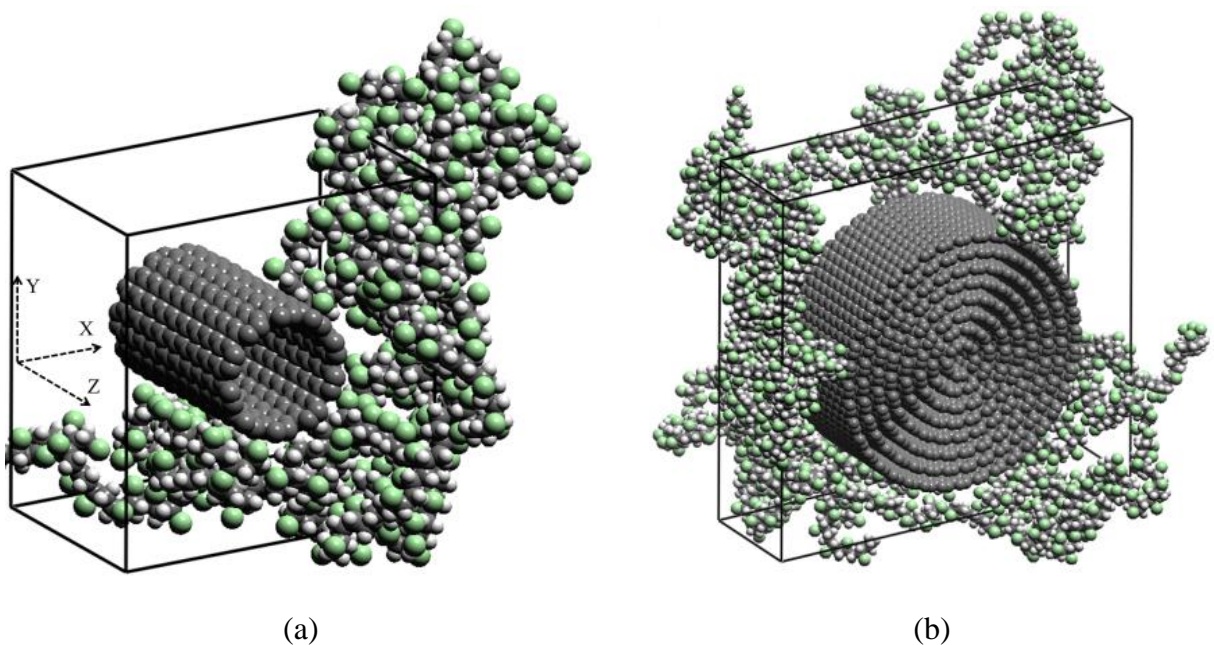


Fig. 6.1 CNT-PVC composite schemes, (a) the SWCNT-PVC composite, and (b) the MWCNT-PVC composite, where the dark gray balls represent carbon atoms, the green ones indicate chlorine atoms, and the white ones stand for hydrogen atoms.

To study the effect of internal walls of an MWCNT on the interphase, an armchair CNT (5, 5)-(40, 40) of eight walls was embedded in a PVC matrix of four random-walk chain molecules with $n = 400$, as shown in Fig. 6.1b.

To generate random-walk polymer chains, the Accelrys Amorphous Cell module which is based on the method proposed by Theodorou and Suter [198] and Meirovitch [208], was used.

6.3 Atomistic simulations

Both the MD and MM methods were used to extract the mechanical properties of the atomic system. MD was used for initial equilibration of the atomistic system. Mechanical properties were then extracted with the aid of MM. The results of the last two chapters on pure polymer and CNTs indicate that the COMPASS force field and the MM simulations with the relaxed atomic models can render good results for isolated polymers and CNTs and thus can be used for analyzing the polymer CNT-composite as used before (*e.g.*, [24, 150, 182, 184]).

The preparation process for atomistic schemes above is quite similar to the method explained in Section 4.3 for pure polymer and the details of stress analysis of NRVE is the same as the method explained in Section 4.4.

6.4 Development of three-phase NRVE model

The existing theories of CNT-PMC rely increasingly on detailed atomistic simulations, owing to the difficulty in characterizing the nanoscale material behaviour through

experimentation. For the SWCNT-PVC composite subjected to the present investigation, one can immediately identify the four regions, i.e., the SWCNT, the vdW gap interphase, the transition PVC phase and the PVC matrix, that play different roles. We consider the volume inside the PVC as a single phase, which contains the SWCNT under the vdW forces. This volume will be treated as a solid fibre in the continuum model and thus named ESF. Adjacent to the ESF, the PVC layer of certain thickness is named the dense interphase. The outermost region is the PVC matrix with the identical mechanical properties as characterized using the model of pure PVC (Section 4.5.3). With these considerations, the three-phase model is summarized in Fig. 6.2. We then seek a way to characterize them respectively.

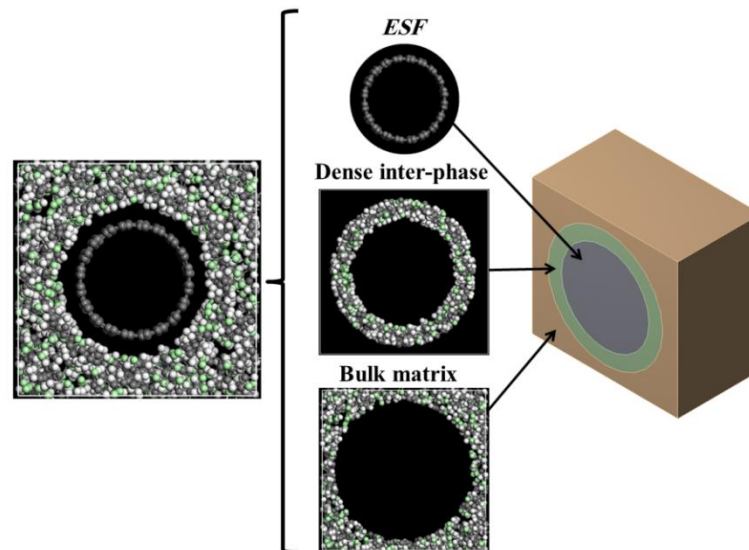


Fig. 6.2 The three-phase NRVE model, phase 1- ESF, phase 2- dense interphase, phase 3- bulk matrix.

6.4.1 Phase 1-ESF

An SWCNT surrounded by PVC may be different from the free-standing one owing to the interaction between two materials. However, in the existing theories, the mechanical properties of the SWCNT in a composite were generally assumed to be identical to the free-standing one. This conventional treatment induces the difficulty in accounting for the vdW interaction between CNT and the matrix. Even though the weak interface can approximately be dealt with by a low-stiffness layer [42] or nonlinear springs [52], the non-local effect of vdW interaction, namely the interaction between CNT atoms and a thin layer of the PVC atoms as schematically indicated in Fig. 6.3a, is very difficult to account with a continuum model. Both complexities can however be treated if the ESF inside the composite is directly characterized. The further gain is that the ESF and the surrounding media can be assumed to be perfectly bonded in a continuum model, since the effect of weak interface between the SWCNT and the matrix has been involved in the characterization of ESF.

To characterize the ESF, the same procedure as described in Section 4.4 is carried out. However, six small strains should now be applied on the boundaries of the ESF. To do so, a prescribed strain field is first applied to every atom in the composite, as shown in Fig. 6.3. The PVC chain is then kept fixed while the SWCNT atoms are allowed to rearrange themselves to minimize the total potential energy. This means that a constant strain is applied only on the ESF boundary through the matrix. Otherwise the matrix atoms will move during the energy minimization process and the strains on the ESF boundaries will become different from the far-field strain. The resultant stress components of the SWCNT

are calculated based on Eq. 4.5, in which V_t represents the volume of the ESF not the entire NRVE volume and the interatomic forces are confined to the interaction within the SWCNT atoms and the vdW forces exerted by the matrix to the SWCNT atoms.

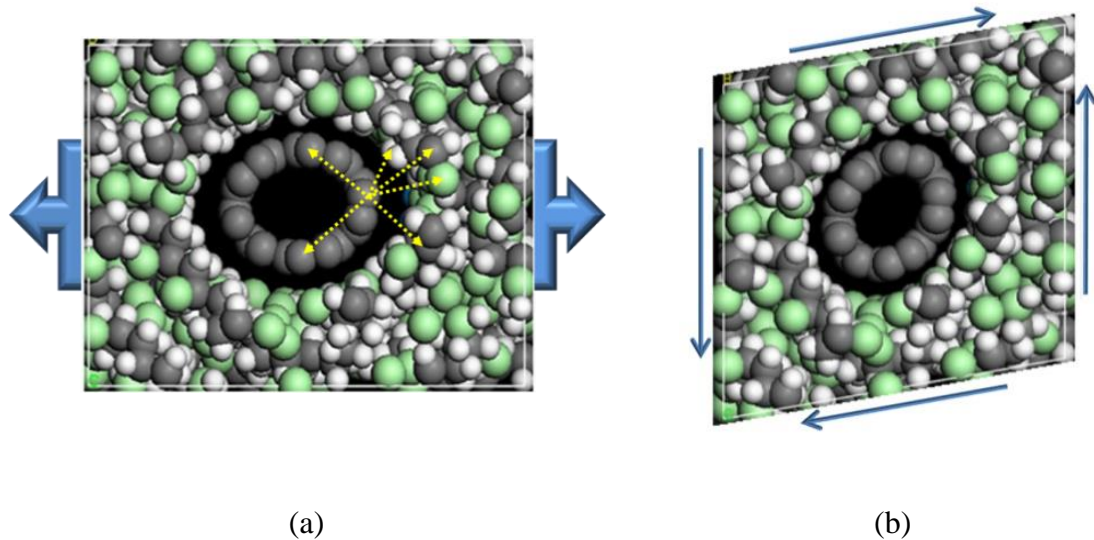
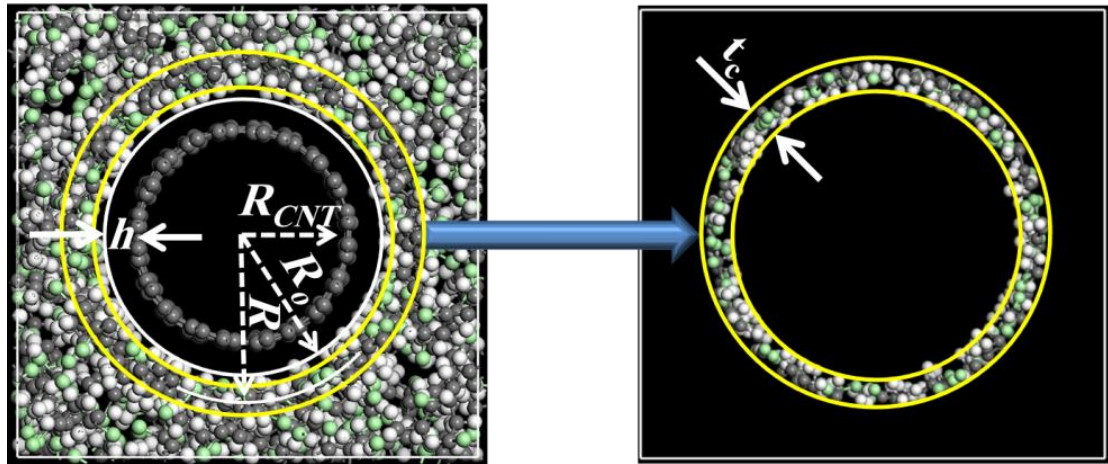


Fig. 6.3 Strain state on the SWCNT-PVC scheme, (a) tensile, and (b) pure shear strain.

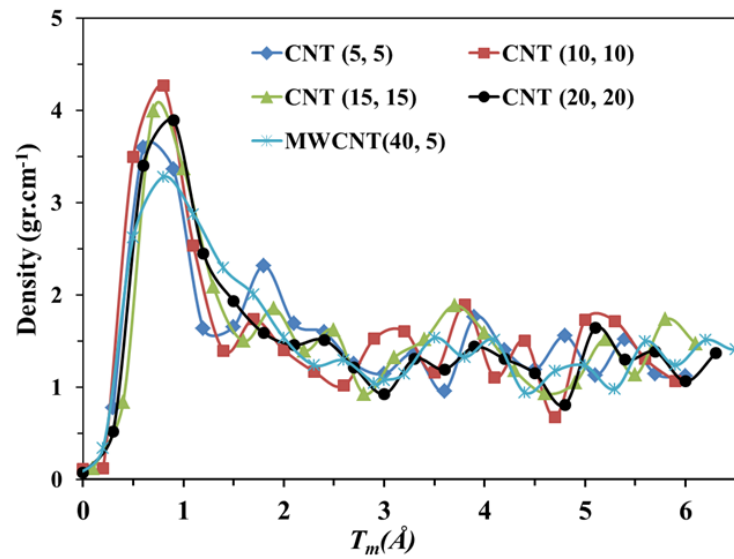
6.4.2 Phase 2 - Dense interphase

There is not a clear boundary between the dense interphase region and the bulk matrix. However, the density change can be used as a reasonable criterion to determine the thickness of this region and was used before in some works (e.g., Ref. [142]). That is, the dense interphase region ends when the density of the material in this region reaches that of the bulk matrix. The local density at different radius R is determined by dividing the atomic mass of a cylindrical shell of thickness $t_c = 0.3 \text{ \AA}$ to the corresponding volume. When such a density is scanned radially from the centre outwards, the inner boundary of the matrix of

radius R_o (the radius of ESF) is determined when the PVC density becomes non-zero, as indicated in Fig. 6.4a. The thickness of the vdW gap is then $h = R_o - R_{CNT}$.



(a)



(b)

Fig. 6.4 (a) Concentric cylinders to explore the local density of the matrix, and (b) the variation of the local density in the matrix with the radial thickness of the matrix.

Fig. 6.4b shows that the density of PVC varies with the radius R from the inner boundary R_0 to the boundary of the simulation box, where the horizontal axis is $T_m = R - R_0$ for shifting the curves resulted from different SWCNTs to the same origin.

For SWCNTs of different diameters, the variations of the local density are close as shown in Fig. 6.4b, The hump of the density variation ends at around $T_m = 1.5 \text{ \AA}$. The density then fluctuates and reduces slowly until about $T_m = 3 \text{ \AA}$. Beyond this, the average density approaches the bulk PVC density of 1.42 g.cm^{-3} . It can be seen that for the MWCNT-PMC the internal walls of the CNT do not have a noticeable effect on the density variation. This result indicates that thickness of the PVC interphase can be treated as a constant for different CNTs. The density of the PVC has a profound effect on its mechanical properties. We use the density as the only parameter to determine the mechanical properties of this dense PVC region. This interphase also renders the lower bound of the dimension of the NRVE for simulating a SWCNT-PVC composite. In this study, close contact effect of CNTs on the interphase is not considered which means that the transverse dimensions of the NRVE should be larger than $2(R_0 + 3) \text{ \AA}$.

6.4.3 Phase 3-Bulk matrix

The bulk matrix region is immediately after the dense interphase (Fig. 6.4a) and has the same density and mechanical properties as the pure PVC. The mechanical properties could be obtained from references (e.g., [212]) or by atomistic simulations. In this work, the atomistic results for pure PVC, as discussed in Section 4.5.3, were used. The volume of

phase 3 is related to the NRVE dimensions and should be large enough to avoid low concentration nano-composites.

6.5 Results and discussion

6.5.1 Stress analysis of atomistic NRVE

The resulting stiffness matrix of the composite exhibits an anisotropic behaviour, which is expected because of the engagement of the SWCNT. The stiffness matrix C , for composite with SWCNT(5, 5) is

$$C = \begin{pmatrix} 6.564 & 3.248 & 3.501 & -0.164 & 0.116 & 0.174 \\ 3.248 & 6.333 & 3.626 & 0.040 & 0.127 & 0.050 \\ 3.501 & 3.626 & 60.462 & -0.133 & -0.189 & -0.135 \\ -0.164 & 0.040 & -0.133 & 1.588 & -0.202 & 0.039 \\ 0.116 & 0.127 & -0.189 & 0.202 & 1.575 & 0.100 \\ 0.174 & 0.050 & -0.135 & 0.039 & 0.100 & 1.605 \end{pmatrix} (GPa) \quad \text{Eq. 6.1}$$

This result indicates that the stiffness matrix of the composite is approximately orthotropic and can be simplified as:

$$C = \begin{pmatrix} 6.564 & 3.248 & 3.501 & 0 & 0 & 0 \\ 3.248 & 6.333 & 3.626 & 0 & 0 & 0 \\ 3.501 & 3.626 & 60.462 & 0 & 0 & 0 \\ 0 & 0 & 0 & 1.588 & 0 & 0 \\ 0 & 0 & 0 & 0 & 1.575 & 0 \\ 0 & 0 & 0 & 0 & 0 & 1.605 \end{pmatrix} (GPa) \quad \text{Eq. 6.2}$$

The elastic constants for the above anisotropic and orthotropic stiffness matrices are summarized in Table 6.1, which shows that the error induced by the orthotropic assumption

is less than 2.5 %. It is also straight from Eq. 6.2 that the atomistic model is transversely isotropic since $C_{11} \cong C_{22}$ and $C_{66} \cong (C_{11} - C_{12})/2$. The results from different NRVEs show transversely isotropic properties and hence the number of elastic constants can be reduced to five.

Table 6.1 Elastic constants of (5, 5) SWCNT-PVC evaluated from Eq. 6.1 and Eq. 6.2

Matrix form	Young's modules (GPa)			Shear modules (GPa)			Poisson's ratio		
	E_{xx}	E_{yy}	E_{zz}	G_{yz}	G_{zx}	G_{xy}	ν_{zy}	ν_{zx}	ν_{xy}
Anisotropic	4.816	4.648	57.753	1.538	1.553	1.591	0.404	0.337	0.488
Orthotropic	4.852	4.665	57.836	1.575	1.588	1.605	0.401	0.335	0.487
% Error	0.77	0.34	0.14	2.41	2.25	0.88	1.06	0.56	0.20
	$E_{xx} = E_{yy}$		E_{zz}	$G_{yz} = G_{xz}$			$\nu_{zy} = \nu_{zx}$		ν_{xy}
Transversely Isotropic	4.732		57.753	1.545			0.371		0.488

6.5.2 The properties of ESF and a simplified CNT-cluster approach

The approach described in Section 6.3 leads to the mechanical properties of ESF shown in Table 6.2. It is noted that the longitudinal modulus E_{zz} is slightly smaller than that directly calculated from the isolated SWCNT. For example, the isolated SWCNT (10, 10) of the assumed wall thickness 0.34 nm has the longitudinal Young's modulus of 0.98 TPa. It leads to the equivalent modulus of the ESF of radius 0.93 nm 515.04 GPa, larger than that listed in Table 6.2. This discrepancy manifests the effect of the vdW forces on the embedded CNT in the matrix.

The complete stiffness matrix of an ESF can be quantified by the approach described in Section 6.3. However, such approach is computationally demanding owing to the large

number of atoms in the PVC chain. We resort to a simplified model as shown in Fig. 6.5, where the surrounding matrix is replaced by six CNT denoted as “CNT-cluster” and the number of atoms to be involved in computation can be minimized by using a PBC. Using CNT-cluster model the computation time for equilibration and stress analysis can be reduced from several days for PVC-SWCNT composite to a few minutes. We then check whether such a CNT-cluster model can be used to approximately determine the mechanical properties of the ESF.

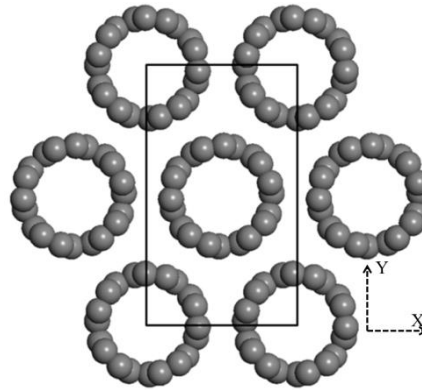


Fig. 6.5 The SWCNT-cluster model in a periodic cell involving some image atoms out of cell.

The same procedure in Section 5.2.2 was taken into account to obtain the most compact hexagonal configuration (Fig. 6.5). The elastic constants of the SWCNT-cluster can be extracted using the procedure described in Section 5.3.2. For stress analysis, Eq. 4.5 was used; however, the equivalent volume of an SWCNT in the cluster is assumed to be the same as that of an ESF. It is noted that the vdW interaction is nonlinear, giving rise to the non-linear behaviour of the ESF under large strain. However, under a small strain of 0.2%

of this study, the error of linearity estimated from the 9-6 Lennard-Jones vdW interaction, is less than 2%.

The SWCNT and the vdW gap interphase in the SWCNT-cluster model are akin to the ESF in a composite. However, under the pressure of 1 atm, the elastic constants are different from those calculated from the composite. This deficiency can be alleviated by tuning the applied pressure until equivalence is achieved. Using the (5, 5) SWCNT-cluster as an example, the elastic constants under different external pressures (P) are shown in Fig. 6.6, which were normalized by the corresponding value of the ESF in the composite. The results show that the normalized elastic constants from the SWCNT-cluster approach almost simultaneously to 1 when the applied pressure is about -1.5 GPa. We named this pressure the equivalent pressure P_e and studied the other cases of different SWCNTs to obtain the variation of P_e with the CNT radius. For SWCNT (10, 10) and SWCNT (15, 15) clusters, the equivalent pressure is -1,000 and -700 MPa respectively. The results are shown in Fig. 6.7 and closely fitted by a polynomial:

$$P_e = 9.9136 R_{CNT}^2 - 255 R_{CNT} + 2248.9 \text{ (MPa)} \quad \text{Eq. 6.3}$$

The predictability of Eq. 6.3 is examined in the case of SWCNT (20, 20). All the results are listed in Table 6.2. It is noted that the discrepancy for the SWCNT (20, 20) does not increase. Therefore, Eq. 6.3 can be used for the typical range of the radius of SWCNT. The negative pressure P_e implies the strong bond between CNTs in the cluster, since they were deliberately pulled apart to achieve the equivalent elastic modulus for the ESF in the composite.

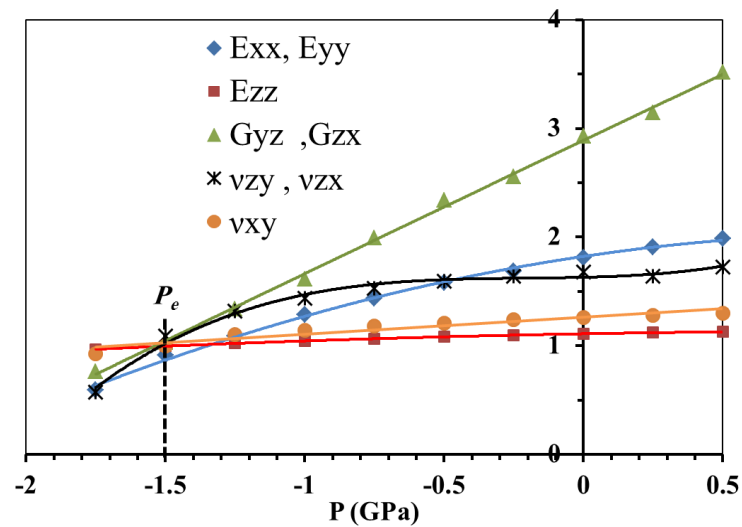


Fig. 6.6 The elastic constants of (5, 5) SWCNT-cluster normalized by those of ESF from the (5, 5) SWCNT-PVC scheme.

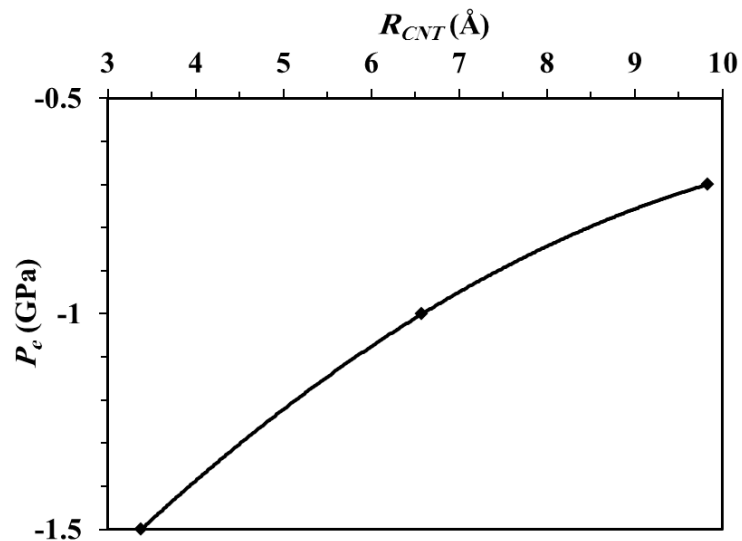


Fig. 6.7 Variation of the proper external pressures on SWCNT-clusters with SWCNT diameter.

For the sake of comparison, we also characterized the elastic properties of free-standing SWCNTs. The SWCNT is assumed as a solid cylinder with the same volume as the ESF.

Three numerical experiments were carried out to extract five elastic constants which are similar to the procedure explained in Section 5.3.3.

The results are listed in row C of Table 6.2. The free-standing SWCNTs (5, 5), (10, 10) and (15, 15) have greater transverse Young's modulus than the corresponding ESFs. However, for SWCNT (20, 20) the transverse Young's modulus becomes smaller than that of the counterpart ESF. It is noted that the magnitudes of longitudinal Young's moduli E_{zz} from the three different calculations are very close to each other and that they all reduce with the increase of the CNT radius. This is because the ESF is a solid fibre rather than a thin-walled shell. Therefore, a larger CNT radius leads to a more empty space and a smaller equivalent modulus. If the wall thickness t of the CNT is assumed to be a constant, the Young's modulus of the ESF reduces proportionally with $2R_{CNT}t/(R_{CNT} + h)^2$ and approaches zero when the CNT radius approaches infinity. Due to the weak vdW interaction, the shear modulus G_{xz} and G_{yz} of the ESFs are much smaller than those of the free-standing SWCNTs. The radial Poisson's ratios of the ESF ($\nu_r = 0.11\sim 0.22$) are smaller than that of the free-standing SWCNT ($\nu_r = 0.28$). It is noted that the out-of-plane Poisson's ratio ν_{xy} of ESF is more than 0.5 and can even approach 1.0 for the SWCNT of larger diameter. As pointed out by Popov, Van-Doren [118], this is due to the flattening of the circular cross-section of the CNT [118] while it is stretched along a diameter.

Table 6.2 Five elastic constants, (A) ESF with PVC-SWCNT composite, (B) ESF with SWCNT-cluster scheme, and (C) free-standing SWCNT as a solid cylinder.

SWCNT	R_o (Å)	R_{CNT} (Å)		Elastic modules (GPa)			Poisson's ratio	
				E_{xx}, E_{yy}	E_{zz}	G_{yz}, G_{xz}	ν_{zy}, ν_{zx}	ν_{xy}
(5,5)	6	3.38	A	12.63	608.30	0.21	0.11	0.54
			B	11.53	607.96	0.23	0.12	0.55
			Error%	8.71	0.06	9.52	9.09	1.85
			C	24.65	624.70	40.53	0.26	0.95
			Difference%*	95.17	2.69	25880	225.0	126.19
(10,10)	9.3	6.58	A	11.2	502.66	0.35	0.18	0.71
			B	10.76	501.05	0.44	0.2	0.76
			Error%	3.93	0.32	25.7	11.11	7.04
			C	16.49	515.04	96.38	0.28	0.98
			Difference%	47.23	2.46	30990	55.55	38.02
(15,15)	12.6	9.83	A	5.72	409.11	0.34	0.21	0.87
			B	5.69	408.19	0.34	0.23	0.89
			Error%	0.52	0.22	0	9.52	2.30
			C	6.34	419.13	40.67	0.28	0.99
			Difference%	10.84	2.44	11862	40	13.79
(20, 20)	15.6	13.09	A	3.13	355.46	0.36	0.22	0.95
			B	3	354.49	0.33	0.24	0.94
			Error%	4.15	0.27	8.33	9.09	1.05
			C	1.61	389.45	36.37	0.28	0.99
			Difference%	48.56	9.56	7806.5	27.27	4.21

*Difference in percentile between A and C.

6.5.3 The interphase

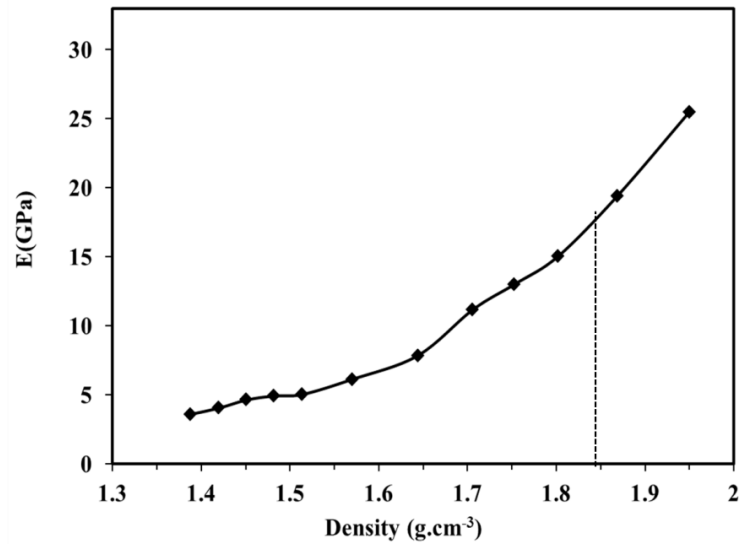
The vdW gap thickness (h), the density of the dense interphase (ρ_i) and the bulk PVC density (ρ_o) of different NRVEs are compared in Table 6.3, showing that the average vdW gap thickness is 2.65 Å less than the graphite sheet distance of 3.4 Å which is used in some works (e.g., [52]). It can be seen that the bulk density (ρ_o) also varies with the SWCNT dimension, although the variation is rather small. This is due to the small size of an NRVE. The variation will vanish if the NRVE is large enough.

Table 6.3 Variation of the dense interphase density with SWCNT dimension.

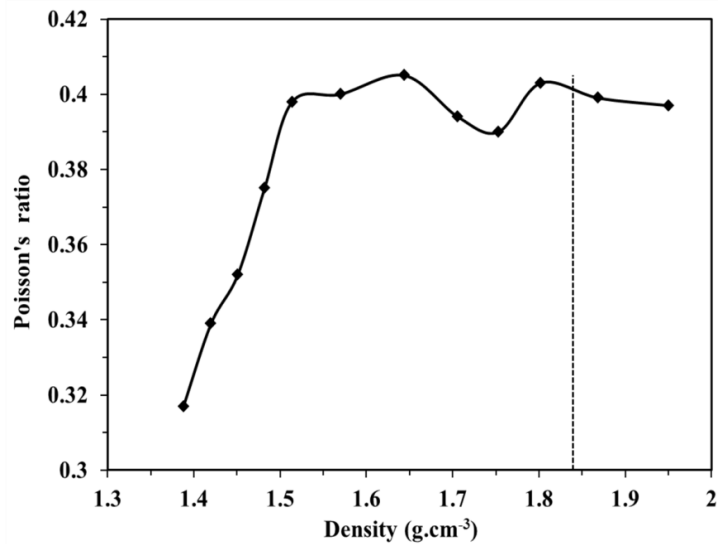
SWCNT type	h (Å)	ρ_i (g.cm ⁻³)	ρ_o (g.cm ⁻³)
(5, 5)	2.62	1.86	1.39
(10, 10)	2.72	1.87	1.42
(15, 15)	2.77	1.80	1.41
(20, 20)	2.51	1.82	1.40
Average	2.65	1.84	1.40
MWCNT	2.65	1.86	1.39

The results show that the thickness of the vdW gap and the density of the dense interphase of the MWCNT-PVC composite are almost the same as those of the SWCNT-PVC composites, indicating that the internal walls of an MWCNT have a negligible contribution to the formation of the dense interphase. Even though the interphase atoms are within the

range of cutting radius of the MWCNT internal walls, their effect on the interphase is weak due to their distance from the internal matrix surface.



(a)



(b)

Fig. 6.8 Elastic constants of PVC against density: (a) Young's modulus, and (b) Poisson's ratio.

To obtain the elastic properties of the dense interphase, we approximated the density as the only state variable and assume that the mechanical properties of the interphase are isotropic. To do so, the cell dimensions of the PVC scheme (Fig. 4.3b) are reduced stepwise and equilibrated by MD simulation for 0.1 ns at each step. The mechanical properties of PVC at different densities are calculated using the method described in Section 4.4. The variation of the Young's modulus and Poisson's ratio of PVC with the density are shown in Fig. 6.8a and Fig. 6.8b respectively. According to Table 6.3, the average density of the dense interphase region is 1.84 g.cm^{-3} . Thus the Young's modulus and Poisson's ratio obtained from Fig. 6.8 are 17 Gpa and 0.4 respectively.

6.5.4 The comparison between the three-phase model and MM simulation

The three-phase model established above can now be employed for a continuum-mechanics analysis. We resort to FE analysis using the FE three-phase model shown in Fig. 6.9a. To manifest the influence of the dense interphase, a two-phase model was generated in which the dense interphase layer was eliminated as shown in Fig. 6.9b. Furthermore, to explore the influence of the vdW gap interphase, both three-phase and two-phase models are re-examined by substituting the ESF with the equivalent free-standing SWCNTs with the properties from Table 6.2. ANSYS was employed to carry out a three-dimensional analysis to obtain the overall elastic constants of a SWCNT-PMC. The present study used ANSYS Workbench to generate initial FE models with the same dimensions of the corresponding atomic NRVEs. They were then transferred to ANSYS APDL. With the script files developed, the stiffness matrix was determined as follows. A small normal strain (0.2%) was applied on one face of the model while the other faces were kept fixed in their

normal direction and free in the other two directions. The total normal force of each face was then calculated from their involved nodes. The average normal stresses were then calculated by dividing the total normal reaction force to the related area. The stiffness matrix components were subsequently determined based on stress-strain relation ($\sigma_i = C_{ij} \varepsilon_j$, $j = 1,3$). The shear modulus was determined in the ANSYS Workbench by applying a pure shear. To avoid the lag effect in the case of $G_{zx} = G_{zy}$, the length of the FE model in the principal direction of ESF was increased while an aspect ratio of 10 was reached for ESF.

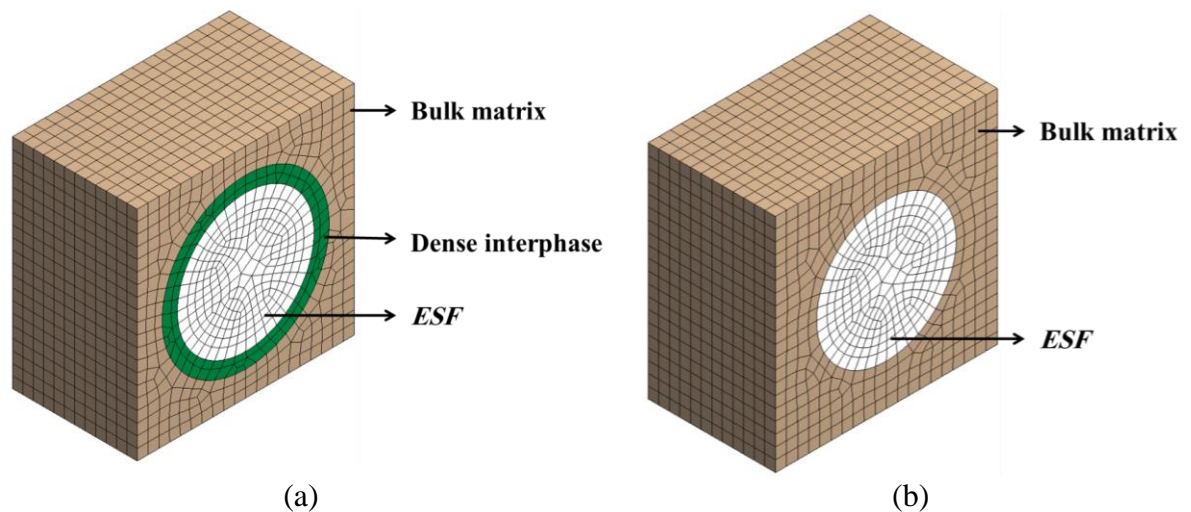


Fig. 6.9 Two FE models: (a) three-phase model, and (b) two-phase model.

The results of four different NRVEs with different SWCNT inclusions are summarized in Table 6.4, where the “MM” rows show transversely isotropic elastic constants of the NRVEs from MM simulation. The FE results are obtained from four different cases. The indices “3P” and “2P” refer to the three-phase and the two-phase models with and without the dense PVC interface respectively. The indices “ESF” or “FS” indicate the elastic

properties of either the ESF or the free-standing SWCNT used for the central solid fibre. It is noted that the three-phase model with both ESF and the dense PVC interface can well predict the stiffness matrix of the composite with errors of less than 10%. The results of two-phase schemes (FE-2P-ESF and FE-2P-FS) exhibit significant discrepancies for transverse Young's modulus and shear modulus, indicating the significance of the dense interphase. It is noted that the composite model becomes less stiff if the dense interphase is not considered. In contrast, using the elastic properties of a free-standing SWCNT in the three-phase scheme (FE-3P-FS) leads to the larger stiffness. These exhibit the opposite effects of the vdW interaction on the SWCNT and the PVC interphase. It makes the ESF less stiff than the free-standing SWCNT but the PVC interphase stiffer than the PVC matrix. For the case of SWCNT (5, 5), the results from the FE-2P-FS model seem to be very close to those of the FE-3P-ESF model and MM simulation, owing to the cancelling of the two opposite effects of vdW interaction and dense interphase. Except for the case of SWCNT (5, 5), the errors in calculating the transverse Young's modulus and the shear modulus increase with the diameter of the SWCNT, if either the dense-interface is ignored or the elastic properties of the free-standing SWCNT are used. The error in calculating the shear modulus is the most prominent. It is noted that we have assumed that the dense interphase region is a homogeneous material however the modelling above could be modified to be more precise if the material in the interphase region were treated as a functionally gradient material (FGM).

Table 6.4 Molecular mechanics and FE results for elastic constants of different NRVEs.

SWCNT type	NRVE dimensions (nm)		Elastic modules (GPa)			Poisson's ratio	
			E_{xx} , E_{yy}	E_{zz}	G_{yz} , G_{zx}	ν_{zy} , ν_{zx}	ν_{xy}
(5, 5)	3.68×3.56×2.38	MM	4.73	57.75	1.54	0.35	0.48
		FE-3P-ESF	4.94	57.24	1.45	0.32	0.47
		Error%	4.44	0.88	5.84	8.57	2.08
		FE-2P-ESF	4.39	55.68	0.46	0.29	0.52
		Error%	7.19	3.58	70.13	17.14	8.33
		FE-3P-FS	5.11	58.64	1.605	0.33	0.48
		Error%	8.03	1.54	4.22	5.71	0
		FE-2P-FS	4.45	56.98	1.56	0.32	0.49
		Error%	5.91	1.33	1.30	8.57	2.08
		(10, 10)	3.78×3.78×2.37	MM	5.7	100.23	1.51
FE-3P-ESF	5.78			100.09	1.51	0.3	0.53
Error%	1.40			0.14	0	0	3.63
FE-2P-ESF	4.78			98.12	1.06	0.28	0.54
Error%	16.14			2.10	29.80	6.67	1.82
FE-3P-FS	6.05			103.23	2.11	0.33	0.51
Error%	6.14			2.99	39.7	8.95	7.27
FE-2P-FS	4.96			100.86	1.80	0.32	0.52
Error%	12.98			0.63	19.20	6.67	4.45

Table 6.4 (Continue)

(15, 15)	3.87×4.25×2.37	MM	5.4	127.12	1.57	0.31	0.65
		FE-3P-ESF	5.59	128.46	1.53	0.3	0.62
		Error%	3.52	1.05	2.55	3.22	4.61
		FE-2P-ESF	4.51	126.24	0.94	0.28	0.62
		Error%	16.48	0.69	40.13	9.68	4.61
		FE-3P-FS	5.75	131.80	2.49	0.32	0.63
		Error%	6.48	3.68	58.60	3.22	3.07
		FE-2P-FS	4.62	129.61	2.13	0.31	0.62
		Error%	14.44	1.96	35.66	0	4.61
		(20, 20)	4.38×4.42×2.37	MM	4.57	143.44	1.14
FE-3P-ESF	4.77			144.47	1.21	0.29	0.72
Error%	4.38			0.72	6.14	0	1.41
FE-2P-ESF	3.76			142.18	0.7	0.28	0.72
Error%	17.72			0.87	38.59	3.45	1.41
FE-3P-FS	4.17			158.24	2.79	0.32	0.78
Error%	8.75			10.31	144.74	10.35	9.86
FE-2P-FS	3.17			155.98	2.15	0.31	0.77
Error%	30.63			8.74	88.59	6.89	8.45

6.6 Conclusions

This chapter has developed a new technique to characterize non-bonded CNT-PMCs. The NRVE of the nano-composite system has been successfully modelled by integrating three phases, the equivalent solid fibre to mimic the CNT under the van der Waals forces, the dense interphase PVC with properly determined thickness and density, and the bulk matrix. Two methods have been established to determine the elastic properties of the equivalent solid fibre from the atomistic NRVE and the CNT-cluster. The study has concluded that the average density of the interphase can be used as a parameter to determine the mechanical properties of the dense PVC region. Using MM results, the method has been examined in a continuum-based three-phase model with the FE method. The model predictions show a good agreement with the atomistic results. The investigation has also concluded that the CNT diameter has a negligible effect on the equilibrium thickness of vdW gap interphase and on the density, thickness and mechanical properties of the dense interphase, and the same equilibrium thickness of the vdW gap. The internal walls of MWCNTs have a negligible effect on the interphase. However, ignoring either the vdW interaction region or the interphase matrix layer can bring about misleading results.

Chapter 7

Chapter 7

Characterizing and modelling the waviness and alignment of CNTs and the effect on their composites

This chapter is based on: “A New Method for Characterizing and Modeling the Waviness and Alignment of Carbon Nanotubes in Composites” by Saeed Herasati and Liangchi Zhang, *Composites Science and Technology*; Volume 100, 2014, Pages 136-142.

7.1 Introduction

Due to the low bending stiffness and exceptionally high aspect ratio of CNTs, they are highly wavy in a matrix [8, 9, 23, 153] which can effectively reduce the stiffness of CNT-PMCs [20, 21, 40, 154-160]. Extensive investigations have been carried out to characterize the waviness morphology and understand the waviness effect of the CNTs on the elastic properties of composites. In most of them however, CNTs have been treated as uniform fibres of a sinusoidal wavy shape [21, 84, 154, 166] or with a simple bow wavy shape [156, 159] which is not consistent with real morphology of the wavy CNTs.

This chapter aims to develop a novel method to characterize the waviness of CNTs, to construct the wavy CNT-PMCs, and to study the effects of waviness and alignment of CNTs on the elastic properties of their composites. The micrograph images of CNTs in composites will be used to characterize the CNT waviness. An algorithm will be developed to efficiently construct an RVE containing a wavy CNT. Then a mechanics model will be

established to carry out the engineering-scale (i.e., macroscopic scale) analysis of the elastic properties of CNT-composites. The proposed model will be verified with experimental results.

7.2 Modelling of wavy CNTs

Each wavy CNT is generated as a cord including a sequence of 3D small straight segments. The total number of segments (N_s) is a function of the CNT volume fraction and its external diameter. For each wavy CNT, a set of points (P_i) on their neutral line is generated. The initial point (P_0) of the first segment is selected randomly on one of the boundary planes of the cubic composite RVE. The direction of the first segment is selected randomly. The method to generate the segments is shown schematically in Fig. 7.1. The essential parameters are defined in Table 7.1.

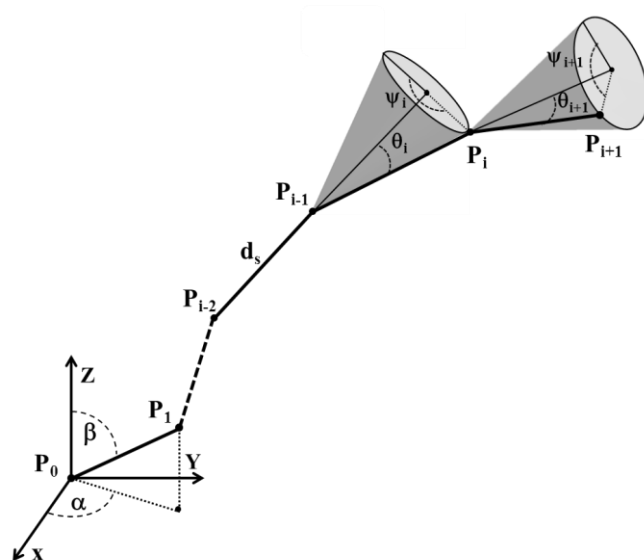


Fig. 7.1 The schematic diagram of the random walking chains.

Table 7.1 Definitions of the algorithm parameters

Parameter	Description/Definition
L_x, L_y, L_z	Dimensions of the cubic RVE in x, y and z directions which are defined as input values
P_i	A set of points on neutral line of wavy CNTs
P_0	Initial point of the first segment
θ_{max}	Waviness angle which is the maximum angle of the cone as shown in Fig. 7.1
d_s	Walking distance or length of a chain segment
V_f	The volume fraction of CNTs
L_{Cmin}	The minimum length of a CNT cord
d_{min}	The minimum distance between two cords
J_{Cmax}	The maximum number of iterations to find a way through other CNTs
N_s	The total number of segments required to reach the desired volume fraction
$P_{i,j}$	The coordinate vectors of the i^{th} point on the j^{th} cord
$S_{i,j}$	The relative coordinate vector between two points on a cord ($P_{i,j} - P_{i-1,j}$)
θ_i	The deflection angle of i^{th} segment which is generated with a standard normal distribution in the range of $(-\theta_{max}, \theta_{max})$
ψ_i	The rotational angle of i^{th} segment around the cone axis that is generated with a uniform distribution in the range of $(0, 2\pi)$

Each new point is generated on the base of a right circular cone. The apex of the cone is located at the end point of the last segment (P_{i-1}) and the axis of the cone is coincident with the orientation of that segment. The length of the generatrix line is equal to the walking step (d_s). The angle of deflection (θ_i) and the rotational angle (ψ_i) are assigned randomly. To avoid close contact of the CNTs, the distance of each new generated point from the previously generated points is calculated to make sure that it is more than the minimum

predefined distance (d_{min}). Otherwise, the algorithm will keep searching a path throughout the chains until such condition is reached. If this path cannot be identified in certain iterations (J_{Cmax}), the current chain is discarded and a new chain will be established. To reduce the shear lag effects, a minimum chain length is defined (L_{Cmin}) in the algorithm as a constraint. The algorithm is described in more detail in Fig. 7.2. It is implemented using a MATLAB code to generate the end points of the segments of a wavy CNT. This provides the input data for a standard FE code, such as ANSYS, to perform the required stress analysis.

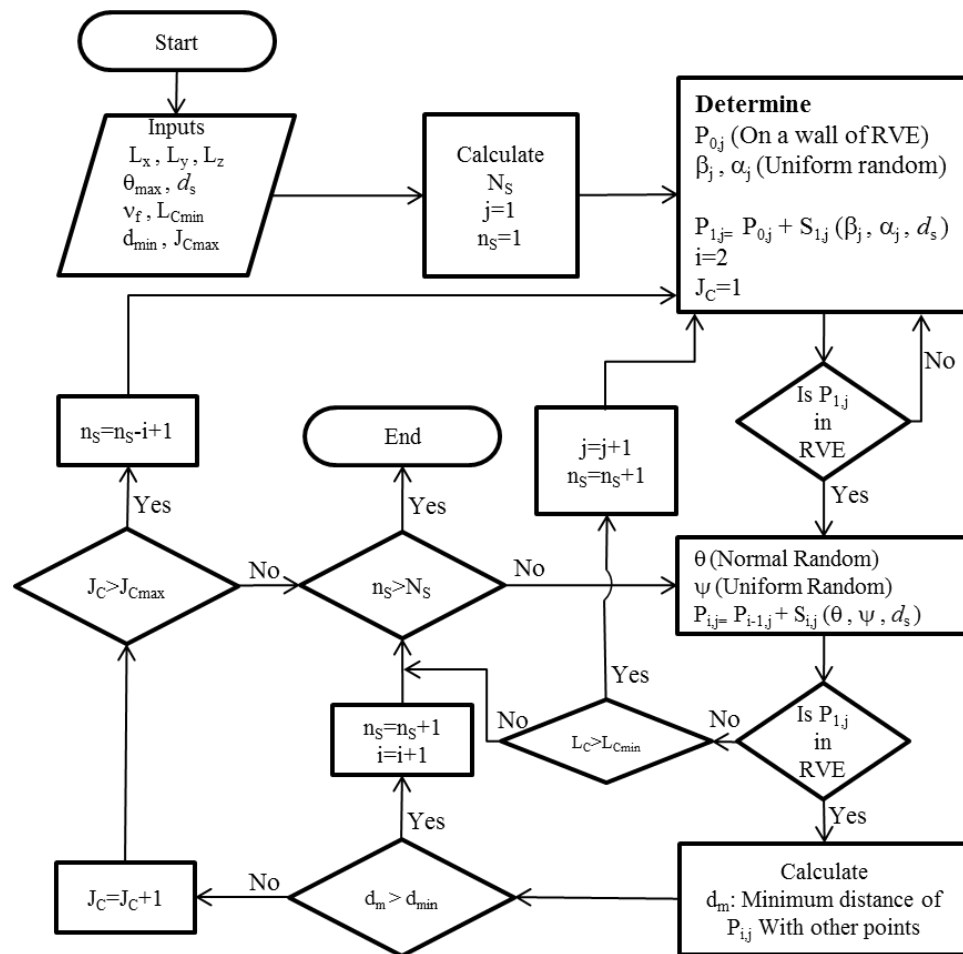


Fig. 7.2 The algorithm flowchart for generating endpoints of segments of wavy cords in a cubic RVE.

7.3 Validation of technique with experimental results

The modelling method and its associated algorithm developed above can be validated by the experimental data available in the literature. Qian *et al.* [9] dispersed MWCNTs homogeneously through a PS matrix with a weight percentage of 1% (equivalent to a volume fraction of 0.487 %). They produced thin film samples with randomly oriented in-plane CNTs. Thus, such a thin film can be appropriated as a lamina with in-plane (2D) distribution of the CNTs. Fig. 7.3a shows a TEM image of a sample thin film containing CNTs [9].

7.3.1 Data scanning

To analyse the waviness in a more consistent manner, the CNTs with approximately the same diameter of 30 nm were chosen, which is equal to the average diameter of the CNTs of the nano-composite sample used in the experiment of Qian *et al.* [9]. The waviness data points of Fig. 7.3b were collected with the aid of the Plot Digitizer software. Our investigation showed that the short walking distance (d_s) can increase the acquisition error, while the long walking distance cannot capture sharp curvatures. We found that the best walking distance is equal to the CNT diameter. Therefore, $d_s = 30$ nm was selected to characterize the waviness of CNTs.

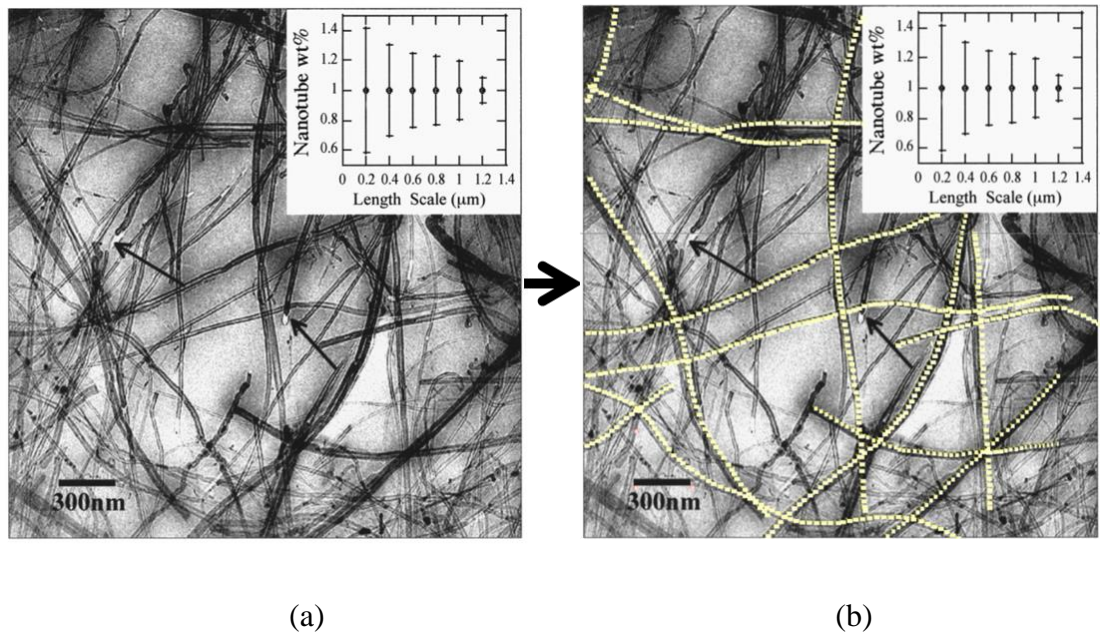


Fig. 7.3 Waviness characterization of the CNTs with a diameter of 30 nm, (a) original image, and (b) selected datapoints.

7.3.2 Data analysis

Since the CNTs are assumed to have a 2D (in-plane) distribution, the deflection angle of each segment (θ) is equal to the angle between the orientation of two sequential segments. The deflection angles of all the segments were analysed with a MATLAB code. Because the rotational angle (ψ) around the cone axis is in the range of $(0, 2\pi)$, the sign of the deflection angle (θ) is not important. Thus, the absolute value of θ for each segment can be calculated and mirrored to the negative side, giving rise to the symmetric histogram shown in Fig. 7.4. This histogram demonstrates that the deflection angle (θ) has a normal distribution which validates our assumption in the algorithm (Fig. 7.2). The maximum deflection angle or waviness angle of the CNTs in the examined composite is $\theta_{\max} = 25^\circ$ as

shown in Fig. 7.4. Although the target walking distance is $d_s = 30$ nm, there was some scattering in the data acquisition which led to an average $d_s = 35$ nm. Fig. 7.4 is based on 740 data points of Fig. 7.3b. An error analysis showed that 300 points could provide sufficiently accurate results, indicating that an analysis on a few CNTs would provide an acceptable representation of the CNT waviness in a composite.

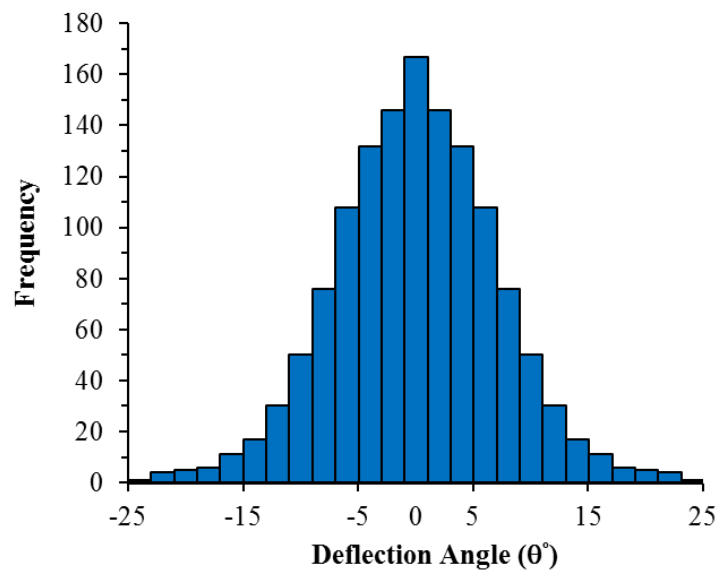


Fig. 7.4 Histogram of the deflection angle from the scanned data.

7.3.3 Constructing wavy CNTs

In order to perform a stress analysis, the RVE of the composite can now be generated using the values of d_s and θ_{\max} obtained above. To understand the effects of waviness and alignment of CNTs, different CNT distribution schemes of aligned (1D-Schemes), in-plane (2D-Schemes) and spatial (3D-Schemes) CNTs with different waviness angles are constructed, as shown in Fig. 7.5 to Fig. 7.8.

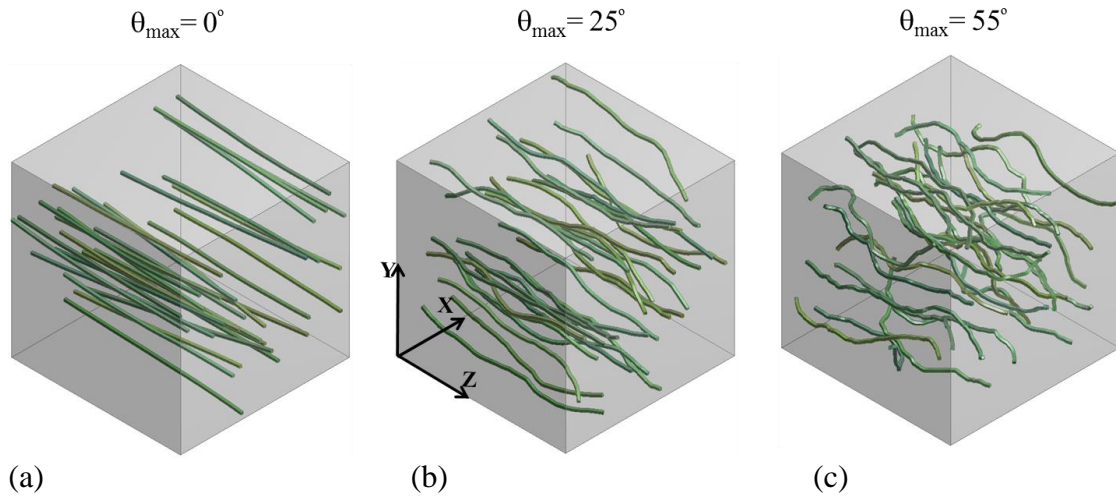


Fig. 7.5 The 1D-Scheme samples including aligned CNTs with the CNT volume fraction of 0.5 and waviness angles of (a) $\theta_{\max}=0^\circ$, (b) $\theta_{\max}=25^\circ$, and (c) $\theta_{\max}=55^\circ$.

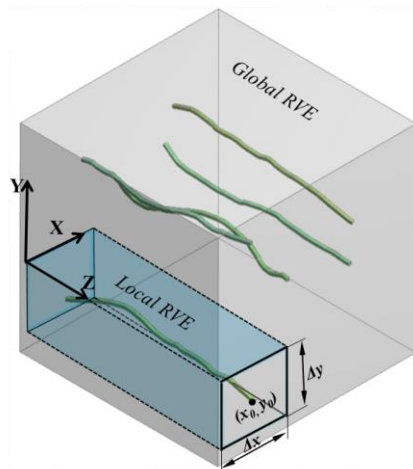


Fig. 7.6 Local RVE defined to generate 1D-Scheme samples.

Fig. 7.5 shows three 1D-Schemes with different waviness angles. To construct such schemes, the same procedure in Fig. 7.2 was applied. After assigning the first point of each CNT ($P_{0,j}$), the local RVE dimensions for this particular CNT in X and Y directions are constrained to a narrow cube with the same length of RVE in the Z direction and four planes at $x_0 \pm \Delta x/2$ and $y_0 \pm \Delta y/2$, as shown in Fig. 7.6. The values of Δx and Δy depend on

the average maximum amplitude of the aligned CNTs which could be measured from the micrograph images [221]. In the present study $\Delta x = \Delta y = 200$ nm were used, because they are close to the maximum amplitude of the wavy CNTs in the experimental characterization of Qian *et al.*[9].

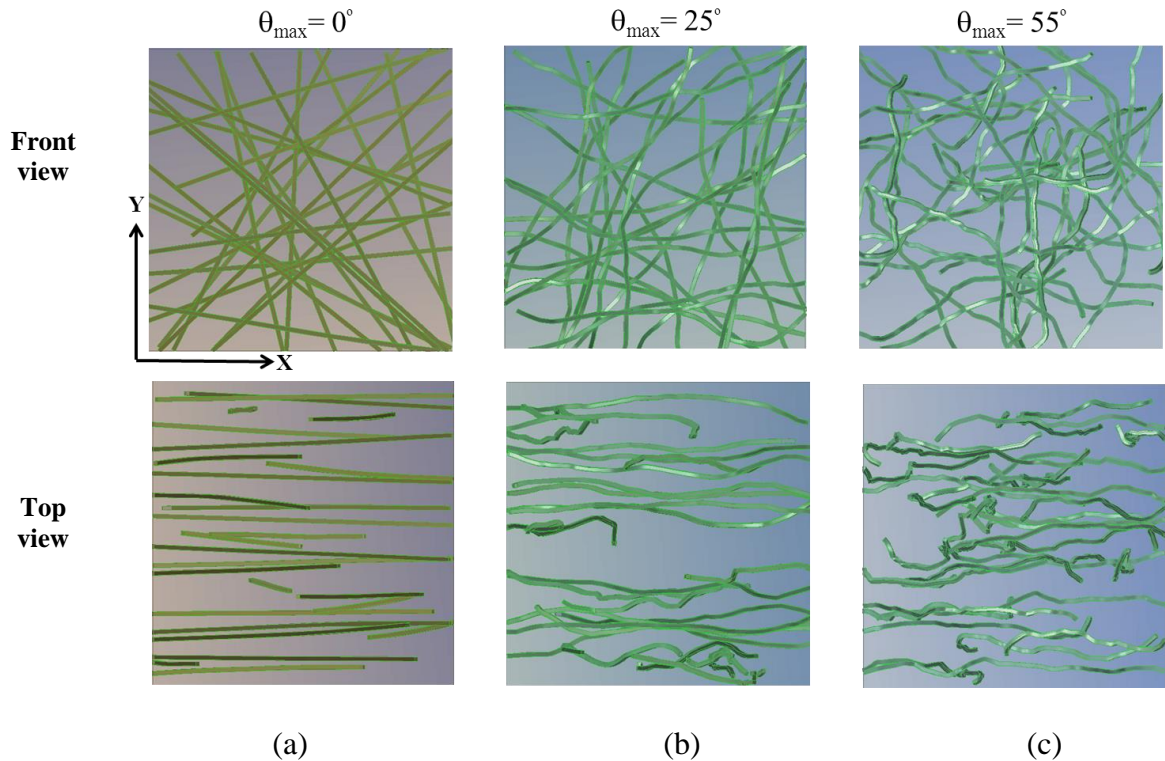


Fig. 7.7 Front and top views of the 2D-Scheme samples with the CNT volume fraction of 0.5 and waviness angles of (a) $\theta_{\max} = 0^\circ$, (b) $\theta_{\max} = 25^\circ$, and (c) $\theta_{\max} = 55^\circ$.

Similarly, the procedure explained for generating the 1D-Scheme samples could be applied for generating the 2D-Scheme samples. In this scenario, however, the local RVE is constrained only in the Z-direction with $z_0 \pm \Delta z/2$ planes and $\Delta z = 200$ nm. The two other dimensions (x and y) are consistent with the global RVE. Fig. 7.7 shows the front and top views of three 2D-Scheme samples with a restricted fluctuation in the Z-direction.

The 3D-Scheme samples can be generated following the algorithm of Fig. 7.2. In the 3D case, however, the CNTs are not constrained within local RVEs. Fig. 7.8 shows three samples with a specific volume fraction and waviness angles of CNTs.

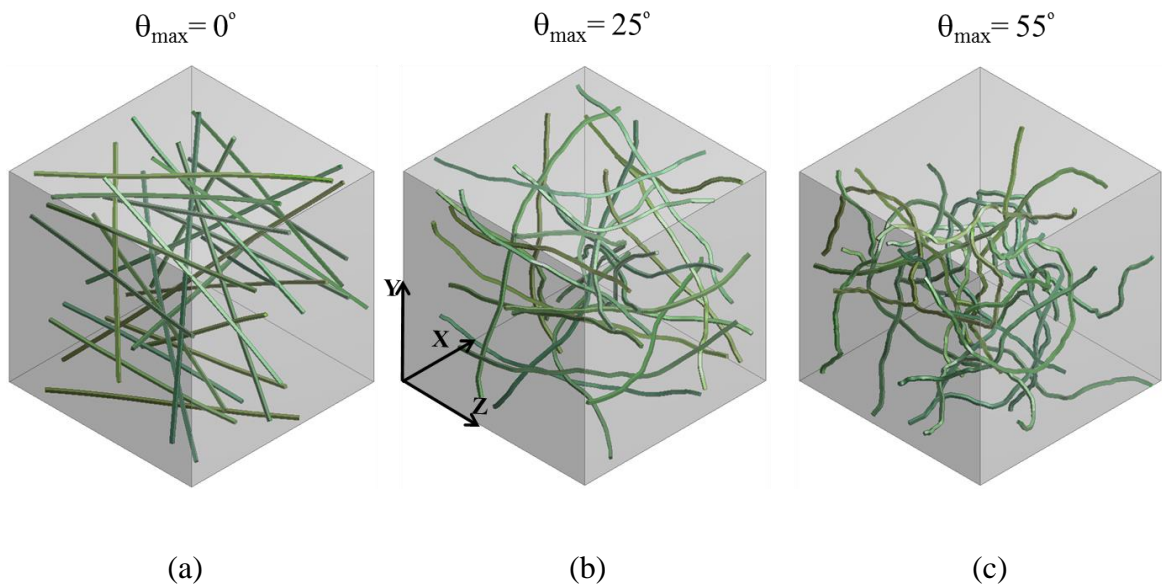


Fig. 7.8 The 3D-Scheme samples with the CNT volume fraction of 0.5 and waviness angles of

(a) $\theta_{\max} = 0^\circ$, (b) $\theta_{\max} = 25^\circ$, and (c) $\theta_{\max} = 55^\circ$.

The characterization of the waviness angle discussed above was from an in-plane distribution of CNTs (Fig. 7.3). As elucidated previously, however, most of the CNT-PMCs have 3D distributions of CNTs in a composite. Hence, specific attention is required to determine their waviness angles. To this end, a $5 \mu\text{m}$ cubic RVE includes a 3D distribution of CNTs with the waviness angle of $\theta_{\max} = 25^\circ$ and the volume fraction of 1% was constructed by the developed algorithm, as shown in Fig. 7.9a. Since the maximum depth to detect the sub-surface CNTs with the voltage-contrast SEM was 250 nm [168], CNTs included in a thin layer of RVE of 250 nm in thickness were projected onto a plane (Fig.

7.9b), showing some short and long CNT segments. Our investigation revealed that most of the short segments are those from the out-of-plane CNTs while the long segments are mostly the in-plane CNTs. To use the technique developed above for quantifying the 3D waviness angle, we can select long segments to represent the in-plane CNTs.

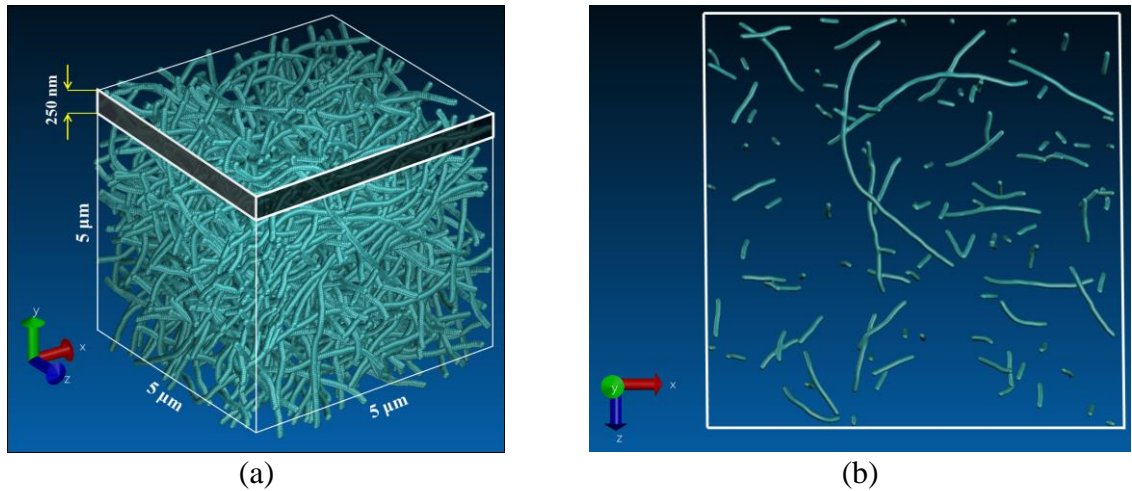


Fig. 7.9 (a) An algorithm-generated cubic RVE with the CNT volume fraction of 1%, θ_{\max} of 25° and side length of $5 \mu\text{m}$, and (b) the top view of a thin layer from the upper region of the RVE.

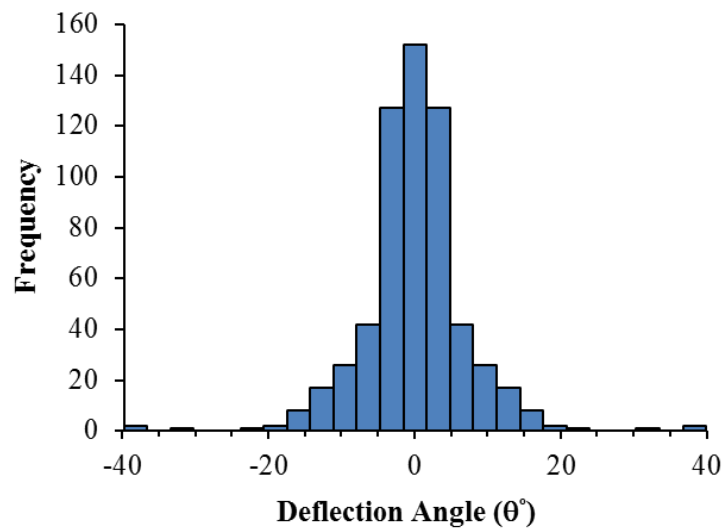


Fig. 7.10 Histogram of θ of the long CNT segments from Fig. 7.9b.

The equivalent histogram of Fig. 7.9b was obtained, as shown in Fig. 7.10. Although a few angles are around 40° , the overall trend of the histogram shows that the graph ends at $\theta = 25^\circ$ which is the same as the original θ_{\max} . This result shows that θ_{\max} can be extracted from the long CNT segments associated with the thin sub-surface layer.

7.3.4 Accuracy analysis

Fig. 7.11a shows the 2D-Scheme sample with $\theta_{\max} = 25^\circ$ and volume fraction of 0.5%, constructed by the algorithm developed. From the figure it can be seen that the result is similar to the original TEM image of Fig. 7.11b.

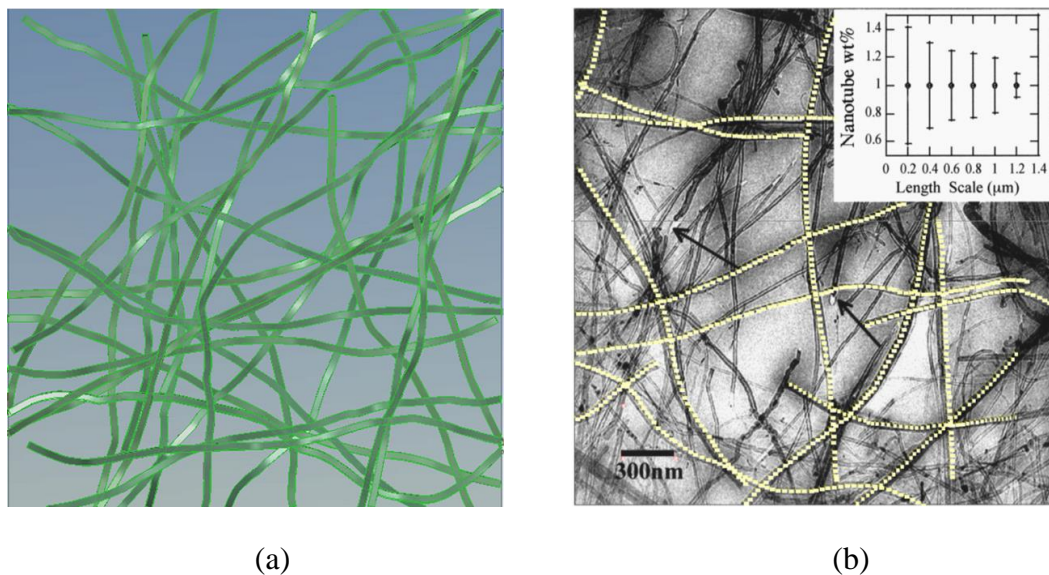


Fig. 7.11 A comparison of an algorithm-generated 2D-Scheme sample with the experimentally observed CNT distribution (CNT volume fraction = 0.5% and $\theta_{\max} = 25^\circ$). (a) the algorithm-generated RVE, and (b) the TEM image [9].

Fig. 7.12a to Fig. 7.12c show the distributions of two key angles of a 3D-Scheme sample with $\theta_{\max} = 25^\circ$ and CNT volume fraction of 0.5%. The corresponding normal probability

(Fig. 7.12b) shows a linear trend of θ . Fig. 7.10c demonstrates that the algorithm generates an appropriate uniform distribution of the rotational angle (ψ) in the range of 0 to 2π .

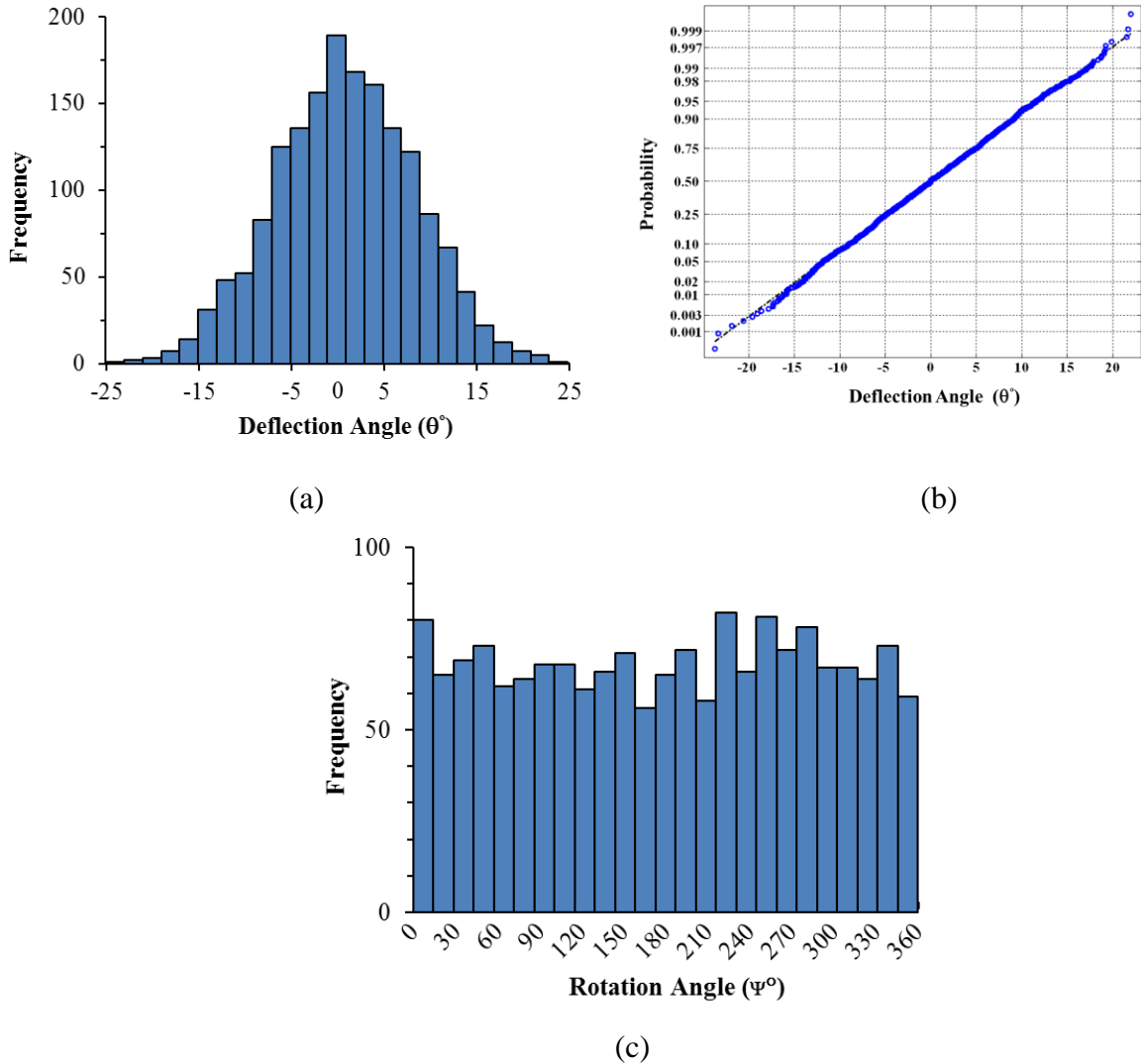


Fig. 7.12 Distribution of the algorithm-generated angles of a 3D-Scheme sample with $\theta_{\max}=25^\circ$. (a) histogram of θ , (b) normal probability of θ , and (c) histogram of ψ .

It is noted that the initial deflection angles (θ) have a normal distribution. In the generation process, the algorithm rejects some deflection angles to avoid a close contact of CNTs. Because of this, one may imagine that the final histogram may not have a normal

distribution of θ . However, the trend of the accepted θ by the algorithm in Fig. 7.12b demonstrates a normal distribution, showing that the rejection process of the algorithm will not change the distribution of θ .

7.4 Stress analysis using FE

The RVE established above enables us to carry out an efficient 3D stress analysis using a conventional FE technique (e.g., using a commercially available FE code, ANSYS). This will allow a convenient characterization of the macroscopic elastic properties of a CNT-PMC. In the present study, the ANSYS Workbench was utilized to generate the initial FE models. The models were then transferred to ANSYS APDL to gain the script file for the stress analysis. In the present case study, the CNTs had a diameter of 30nm; thus the effect of the CNT-matrix interphase on the macroscopic Young's modulus of the CNT-PMC could be ignored without causing any noticeable error according to Ref. [145].

7.4.1 Mesh generation

For the simplicity of the FE meshing but without losing the generality, it is assumed that a CNT can be regarded as a solid fibre of a square cross-section (called a CNT-fibre hereafter for convenience). The mechanical properties of a CNT-fibre are the same as the CNT. The cross-section of the CNT-fibre was determined in such a way that it gave rise to the same volume fraction of the CNTs in the composite. The wavy CNT-fibres could then be easily meshed using the 20-node brick element (Solid 186) in ANSYS, as shown in Fig. 7.13a. The matrix, however, was meshed with the 10-node tetrahedron elements (Solid 187), as demonstrated in Fig. 7.13b. Each CNT-fibre could be meshed as a sequence of brick

elements. A sensitivity test on the mesh size showed that finer meshes have a negligible influence (less than 3%) on the overall results.

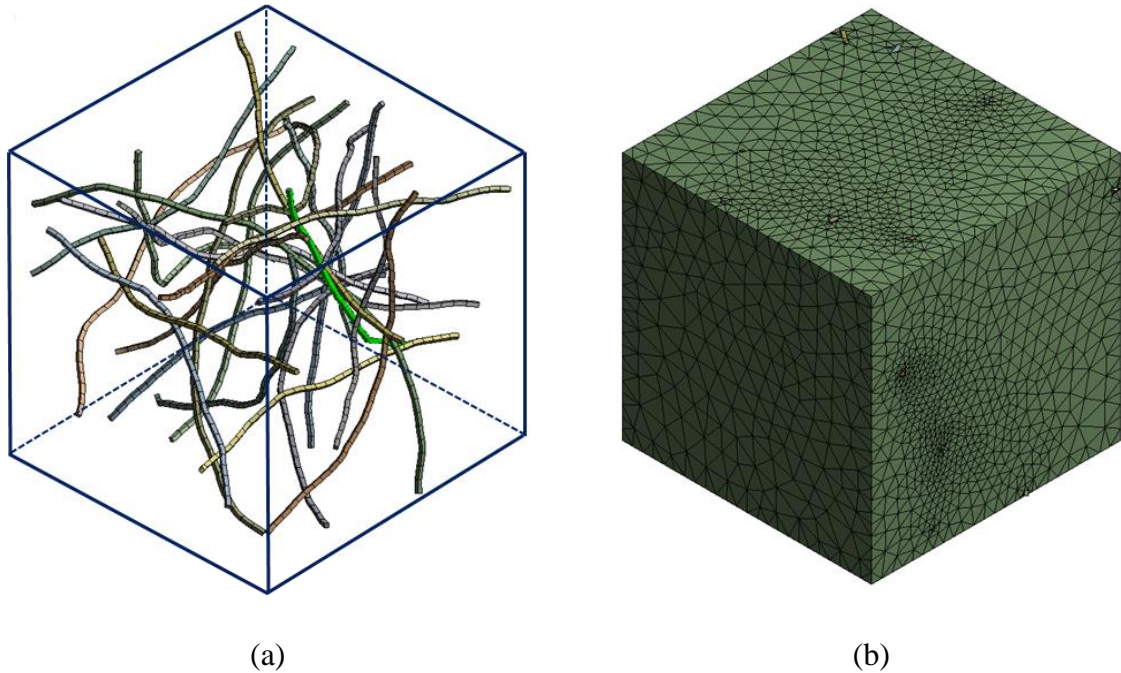


Fig. 7.13 Sample mesh generation of (a) 3D distribution of CNTs, and (b) matrix.

7.4.2 Local coordinates of CNT-fibre elements

In the majority of the previous studies in the literature, CNTs have been treated as an isotropic material (e.g. Ref. [84, 85]). Nevertheless, CNTs have been found to have transversely isotropic properties [86, 222] as we do in this study. Thus, a coordinate system of a CNT-fibre must follow the direction of a CNT in each point. A script file can be developed to adjust the principal axis of the local coordinate system of each element parallel to the neutral axis of the CNT-fibre. A sample wavy CNT-fibre and the corresponding local coordinates of each element are shown in Fig. 7.14.

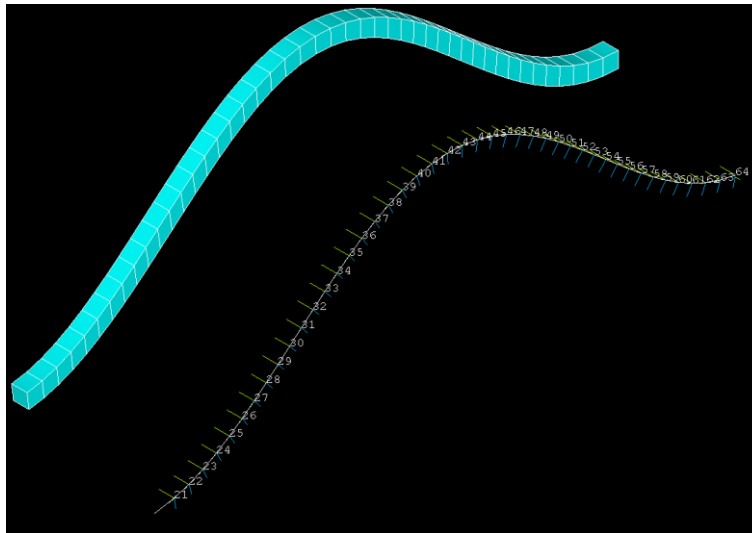


Fig. 7.14 The local coordinate system of each element is oriented to be tangent to the neutral axis of a CNT-fibre.

7.4.3 Stress-strain analysis

With the script files developed, the stiffness matrix is determined. A small normal strain of 0.2% was applied on one face of the RVE while the other faces were kept fixed in their normal directions and free in their other two directions. The total normal force of each face was calculated from their nodes involved. The average normal stresses were then calculated by dividing the total normal reaction force to the related area. The stiffness matrix components were subsequently determined based on the stress-strain relation, *i.e.*

$$\sigma_i = C_{ij} \varepsilon_j, \quad j = 1,3, \quad \text{Eq. 7.1}$$

where σ_i , C_{ij} and ε_j are normal stress, stiffness matrix and strain components respectively. The elastic moduli were then calculated based on the stiffness matrix relations

in Appendix 1. For the FE stress analysis, we used the isotropic elastic properties of the blank PS matrix from the work of Qian *et al.*[9], i.e., $E_m=1190$ MPa with the Poisson's ratio of $\nu_m=0.38$. Assuming that the length of nanotube is bigger than $1 \mu\text{m}$, the transversely isotropic properties of an MWCNT of diameter 30 nm was obtained with the method proposed by Shen *et al.* [86], which gave rise to the elastic properties of $E_{zz} = 1.1$ TPa, $E_{xx} = E_{yy} = 14$ GPa, $G_{zx} = G_{zy} = 190$ GPa, $\nu_{zx} = \nu_{zy} = 0.13$ and $\nu_{xy} = 0.91$. It is noted that regards to the big diameter of the studied MWCNT, MM is not a suitable tool for calculating its elastic properties. Therefore, in this study the analytical method based on the work of Shen *et al.* [86] was applied.

7.5 Results and discussion

The variations of the longitudinal elastic modulus ($E_{xx} = E_{yy}$) and transverse elastic modulus (E_{zz}) of the 2D-Scheme composites with θ_{\max} are shown in Fig. 7.15. It can be seen that these moduli decrease with increasing the θ_{\max} . When θ_{\max} changes in the range of 5° to 40° , the moduli vary almost linearly. After θ_{\max} goes beyond 50° , the Young's moduli in both the longitudinal and transverse directions approach their steady values.

The error scales denoted in the figure are the results of four samples. It can be seen that at a low waviness the longitudinal Young's moduli have a bigger standard deviation because of the small dimension of the RVEs and the low percentage of the CNTs in the composites. This indicates that if the CNTs are straight, adding little more CNTs in a direction can significantly increase the stiffness of the composite in that direction. This effect will become weaker if the number of the CNTs is increased at a higher volume fraction. Under a

higher waviness angle, the elements of each CNT-fibre are scattered in a wide range of directions. Thus, statistically the composite will become quasi-isotropic. As a result, the moduli have lower standard deviations.

The vertical dashed line in Fig. 7.15 shows the Young's modulus of a composite includes the CNT-fibre of waviness angle $\theta_{\max} = 25^\circ$ and volume fraction = 0.5% (the same as in the experiment done by Qian *et al.* [9]). It is clear that the prediction of the model presented in this study for longitudinal Young's modulus ($E_c = 1.41E_m = 1680 \pm 96$ MPa) is in excellent agreement with the experimental measurement ($E_c = 1.42E_m = 1690 \pm 130$ MPa). This shows that the proposed method in this chapter provides very accurate predictions.

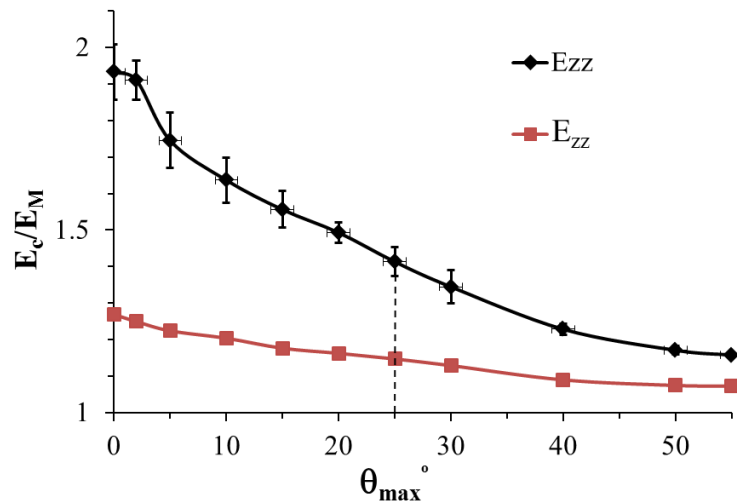


Fig. 7.15 The relative Young's moduli of the composite to the matrix with different waviness angles (θ_{\max}) (volume fraction = 0.5%; 2D-Scheme).

The effect of CNT alignment on the variation of the relative longitudinal Young's modulus is demonstrated in Fig. 7.16 (the CNT volume fraction of 0.5%). It is shown that the CNT alignment has a remarkable effect on the modulus in the whole range of waviness angles.

For example, the dashed line on the waviness angle of 25°, which is the same as the experimental work of Qian *et al.* [9], shows an improvement of 21% when the CNTs have a 3D distribution (3D-Scheme). This improvement jumps to 41% if the CNTs have an in-plane distribution (2D-Scheme). If the CNTs are fully aligned (1D-Scheme), a significant improvement of 110% (more than five times that for the 3D-Scheme) is achieved. The above comparison demonstrates that at the same waviness angle, the alignment of CNTs can significantly enhance the Young's modulus of their composites.

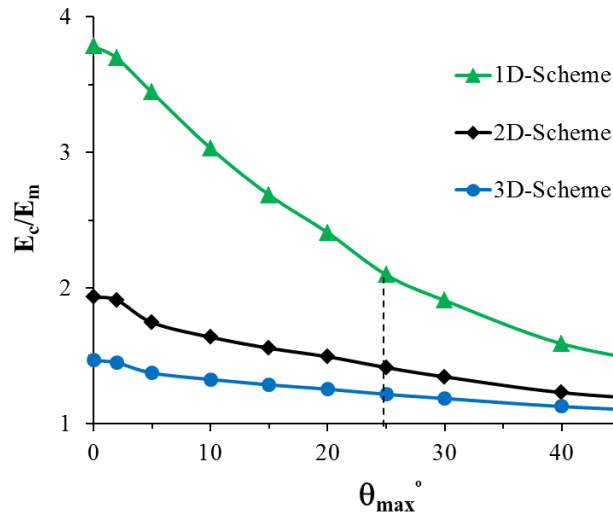


Fig. 7.16 Effect of CNT-alignment on the variation of E_c/E_M with the CNT waviness angle.

The upper limit of the relative longitudinal Young's modulus of the CNT-PMC with aligned straight CNTs (i.e., 1D-Scheme at $\theta_{\max}=0$) can be obtained from the rule of mixture, i.e,

$$E_c/E_M = v_M + v_{CNT} E_{CNT}/E_M, \quad \text{Eq. 7.2}$$

in which v_M and v_{CNT} are the volume fractions of the matrix and CNTs respectively, and E_{CNT} is the longitudinal Young's modulus of the CNTs. With the aligned straight CNTs, Eq. 7.2 gives $E_C/E_M = 5.6$, which is greater than our model prediction of 3.8. A major cause of this discrepancy is due to the fact that the present modelling imitates the experimental micrograph images (e.g. Ref. [221]) in which the CNTs were aligned randomly rather than absolutely straight along the Z-axis, and allowed to have a misalignment in their local RVE which reduces the E_C .

7.6 Conclusions

This chapter has developed an innovative technique to characterize the waviness of CNTs in composites and to study the effect of waviness and alignment of CNTs on the macroscopic elastic properties of CNT-PMCs. The concept of CNT waviness angle has been introduced and an efficient algorithm has been established to construct wavy CNTs for 1D, 2D and 3D CNT-PMCs. The RVEs generated were implemented in a commercially available FE code for characterizing the macroscopic properties of CNT-PMCs. A comparison with the experimental results shows that the method can accurately predict the elastic properties of CNT-PMCs. The analysis also concludes that the waviness of the CNTs influences the stiffness significantly. However, compared to the waviness, the CNT alignment is a more superior parameter affecting the elastic properties of the composite.

Chapter 8

Chapter 8

The effect of interphase on the macroscopic elastic properties of non-bonded SWCNT-PMCs

8.1 Introduction

The interphase of a CNT-matrix plays an important role in determining macroscopic properties of the composite. In the case of a non-bonded SWCNT-PMC, there are two distinct interphases: the vdW gap interphase and the dense interphase. In Chapter 6, a comprehensive atomistic NRVE for characterizing SWCNT-PVC composites was developed. The atomistic NRVE was capable of accommodating the coupled contribution of all phases associated with a CNT-PMC unit: the matrix, the dense interphase, the vdW gap and the SWCNT. The vdW gap and the SWCNT were regarded as an ESF. The elastic properties of each phase was then characterized by atomistic simulation and implemented within a three-phase continuum-based FE model. Compare to the atomistic NRVE, the three-phase model does not only reduce the computational cost but also give a flexibility to calculate the elastic properties of NRVE with a desired size. Our investigation showed that the NRVEs have transversely isotropic properties and that the vdW gap interphase is softer but the dense interphase is stiffer than the bulk matrix. It was concluded that ignoring an interphase region would bring about erroneous predictions of the elastic parameters of the NRVE, particularly its transverse Young's modulus and the out-of-plane shear modulus. However, the results were limited to a special case with straight SWCNTs. In reality, nevertheless, CNTs in a composite are highly wavy because of their flexibility and

extremely high aspect ratio of length to diameter [9, 153]. Moreover, in Chapter 7, a technique for characterizing the waviness of CNTs, together with an algorithm to generate wavy CNTs consistent with experimental observations was proposed. The method was verified by experiment and can be considered reliable for studying the effect of SWCNT waviness.

This chapter will develop a multiscale method to explore the impact and contribution of each of the interphases outlined above on the overall elastic properties of non-bonded, randomly wavy SWCNT-PMCs. Aligned and 3D distributed SWCNTs with different waviness angles will be constructed and implemented in an FE platform for stress analysis.

8.2 Multiscale modelling

The primary strategy of the multiscale modelling is illustrated in Fig. 8.1. The basic element is the atomistic NRVE (A-NRVE) which was characterized in Chapter 6. In a CNT-PMC, the volume fraction of CNTs is always low, rarely above 20%. It is therefore rational to assume, when the CNTs are dispersed well in the composite in manufacturing, that each CNT is surrounded fully by the matrix, and that the distance between individual CNTs is much larger than the thickness of an individual CNT-matrix interphase. Hence, the contact between CNTs and that between CNT-matrix interphases does not need to be considered in the modelling. As a result, A-NRVE under a PBC must be big enough to avoid any artificial effect of interphase or CNT contacts. To reduce a close contact between wavy CNTs in micro-scale, the cross-section area of NRVE is reduced as much as possible. To do so, the minimum NRVE dimension can be confined by the external diameter of the

dense interphase layer and treated by the three-phase FE model that was explained in Chapter 6 as illustrated in Fig. 8.1, called 3P-NRVE. When this 3P-NRVE is applied to a greater scale analysis, the characterization can be treated as a homogeneous solid NRVE (S-NRVE). In this way, the calculation will be efficient but the lower scale effects (atomistic and interphase) are already included.

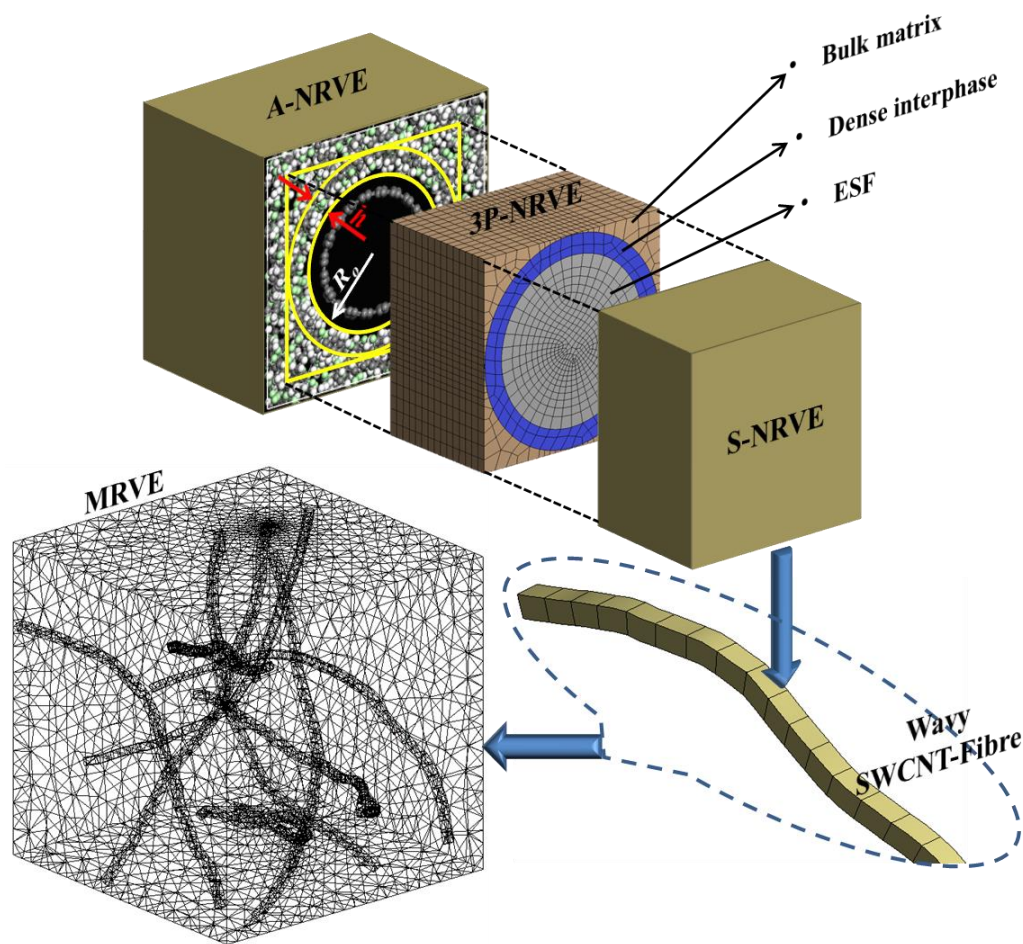


Fig. 8.1 A schematic diagram of the multiscale modelling strategy for characterizing SWCNT-PMCs from the atomistic scale NRVE to the micro-scale MRVE. The MRVE is ready to be used for an efficient FE analysis but with all the atomistic and interphase effects counted.

A series of S-NRVEs can be assembled to build up a randomly wavy SWCNT-fibre, as illustrated in Fig. 8.1. A micro scale representative volume element (MRVE) can therefore be obtained by assembling such SWCNT-fibres with the surrounding PVC matrix. Such an MRVE is ready to be used for an efficient FE analysis but with all the atomistic and interphase effects counted.

8.2.1 Elastic properties of S-NVRE

The elastic properties of S-NRVE can be obtained by transferring those of 3P-NRVE which includes three phases: the ESF, the dense interphase and the bulk matrix, as illustrated in Fig. 8.1. To explore the diameter effect on the properties of the 3P-NRVE, a variety of SWCNTs, with typical diameters ranging from 6.76 Å of SWCNT (5, 5) to 26.18 Å of SWCNT (20, 20), were used to construct the corresponding 3P-NRVEs. It has been shown that the dense interphase of PVC has a thickness of 3 Å, Young's modulus of 17 GPa, and Poisson's ratio of 0.40. The Young's modulus and Poisson's ratio of the bulk PVC are 3.6 GPa and 0.38, respectively. The overall elastic properties of 3P-NRVE can therefore be obtained by a 3D FE analysis developed in Chapter 6. This gives rise to the five elastic moduli of the corresponding S-NRVE, as listed in Table 8.1. Rows A to D represent the schemes of: (A) all phases included, (B) vdW gap excluded, (C) dense interphase excluded, and (D) both dense interphase and vdW gap excluded.

Table 8.1 Elastic properties of transversely isotropic 3P-NRVEs containing SWCNTs of different diameters

SWCNT	R_o (Å)	Cross section (Å ²)	Elastic modules (GPa)			Poisson's ratio		
			E_{xx}, E_{yy}	E_{zz}	G_{yz}, G_{xz}	ν_{zy}, ν_{zx}	ν_{xy}	
(5,5)	6	18×18	(A)	11.27	221.33	1.97	0.29	0.58
			(B)	15.54	233.02	4.24	0.33	0.65
			(C)	5.91	214.87	0.75	0.25	0.49
			(D)	6.96	226.90	2.40	0.30	0.52
(10,10)	9.3	24.6×24.6	(A)	10.11	231.63	1.74	0.29	0.66
			(B)	12.61	237.82	5.05	0.32	0.73
			(C)	6.10	226.97	0.79	0.27	0.57
			(D)	7.04	233.24	3.05	0.31	0.59

Table 8.1 (Continue)

(15,15)	12.6	31.2×31.2	(A)	6.96	214.66	1.53	0.30	0.78
			(B)	7.43	220.22	5.74	0.32	0.85
			(C)	4.83	210.91	0.65	0.28	0.69
			(D)	5.09	216.51	3.56	0.30	0.74
(20,20)	15.6	37.2×37.2	(A)	5.10	200.66	1.40	0.30	0.79
			(B)	4.34	219.94	5.88	0.32	0.86
			(C)	3.57	197.47	0.62	0.28	0.78
			(D)	2.80	216.78	3.68	0.30	0.85

(A): all phases included; (B): vdW gap excluded; (C): dense interphase excluded; (D): both dense interphase and vdW gap excluded

8.2.2 Elastic properties of MRVE

The wavy SWCNT-fibres could be generated based on the algorithm developed in Chapter 7. In this chapter $d_s = 3$ nm is used. The wavy SWCNT-fibres are then assembled with the PVC matrix in a cubic MRVE. A sensitivity analysis showed that the overall elastic properties of MRVE change with the variation of its dimensions (due to shear lag effect),

but converge when the dimensions reach about 100 times those of the S-NRVE side length. The FE models for stress analysis are then generated with the aid of the commercial ANSYS Workbench. Since the S-NRVE elements have transversely isotropic properties, the local coordinate system of each element must be directed in parallel with the neutral axis of the CNT cord with the script file developed.

To study the interphase effect under different waviness angles, SWCNT (10, 10) is selected because this size is typical in the synthesized SWCNTs. However, when studying the interphase effect with varying SWCNT diameter, the waviness angle is fixed. To explore the role of CNT alignment, both aligned SWCNTs, denoted as the 1D-Scheme for convenience of discussion, and randomly distributed in three-dimensional directions, denoted as the 3D-Scheme, are investigated with a fixed volume fraction of 0.5% but a variety of waviness angles (*e.g.* Fig. 8.2). 1D-Scheme models are generated with the algorithm, that explained in Section 7.3.3. In this study, the local RVEs for the 1D-Scheme fibres are limited to $\Delta x = \Delta y = 20 \text{ \AA}$.

The stiffness matrix components of an MRVE are determined based on the FE method that was explained in Section 7.4.3. The elastic properties of the bulk PVC from our previous atomistic simulation in Chapter 4 and the experimental results available [214] are $E_m=3.6 \text{ GPa}$ and $\nu_m=0.38$ [215]. The elastic properties of the S-NRVEs of different schemes are listed in Table 8.1.

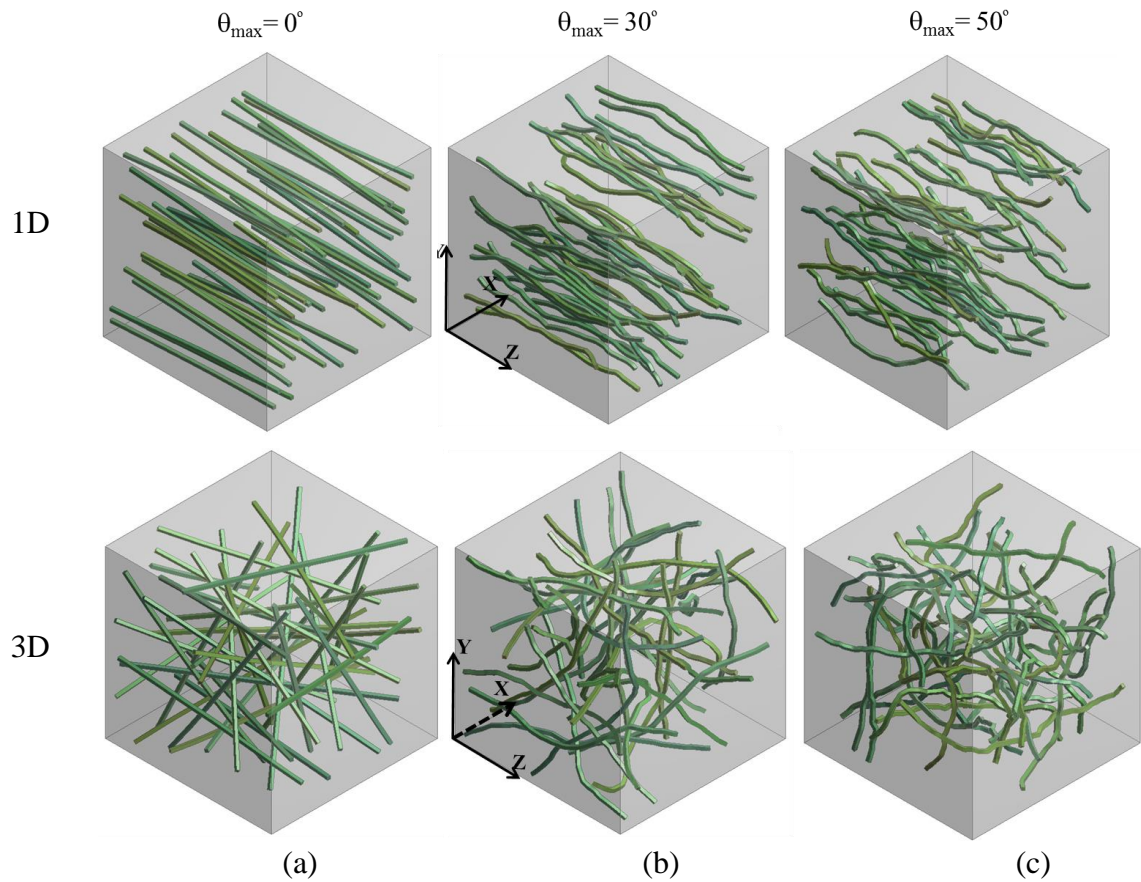


Fig. 8.2 1D and 3D-Schemes of SWCNT-PMCs with a volume fraction of 0.5% and waviness angles of (a) $\theta_{\max}=0^\circ$, (b) $\theta_{\max}=30^\circ$, and (c) $\theta_{\max}=50^\circ$.

8.3 Results and discussion

Fig. 8.3a shows the variation of the relative Young's modulus (E_c/E_m) of the CNT-PMC using the 3D-Scheme with SWCNT (10, 10). Each point in the figure is an average of three samples. The results show that the Young's modulus will be overestimated if the effect of vdW gap interphase is ignored but will be underestimated if the dense interphase effect is neglected. When both the vdW gap and dense interphases are ignored, the results approach those including all phases. This indicates that with SWCNT (10, 10), the overall influence of the interphases as a whole is insignificant. However, Fig.8.3b demonstrates that when

the diameter is greater than SWCNT (10, 10), the discrepancy of overall interphase effect becomes greater. A closer look to the Fig.8.3b, shows that the upper and lower bonds, that are case B and C respectively, approach together with increasing SWCNT diameter and suppose to converge to the case A, include all phases, after a certain big diameter of CNTs beyond the range of our study. This is consistent with the findings of Wang *et al.* [145] and Odegard *et al.* [142]. They claimed that the effect of interphase on the elastic properties of a nano-composite reduces and will vanish eventually when the diameter reaches to a certain big diameter that is 20 nm and 200 nm as claimed with Odegard *et al.* and Wang *et al.* respectively. Fig. 8.3b also shows that SWCNT diameter has a big influence on the composite properties.

Fig. 8.3 shows that when the volume fraction of SWCNTs is a constant, the macroscopic Young's modulus of a CNT-PMC decreases with increasing the waviness and CNT diameter. This is consistent with the results of Tsai *et al.*[31]. In other words, with a given CNT concentration and waviness angle, in the range of SWCNT diameter studied, smaller SWCNTs are more superior reinforcing fillers. However, it should be noted that a smaller SWCNT is more easily bent to make its waviness angle larger, and in turn reduce the stiffness.

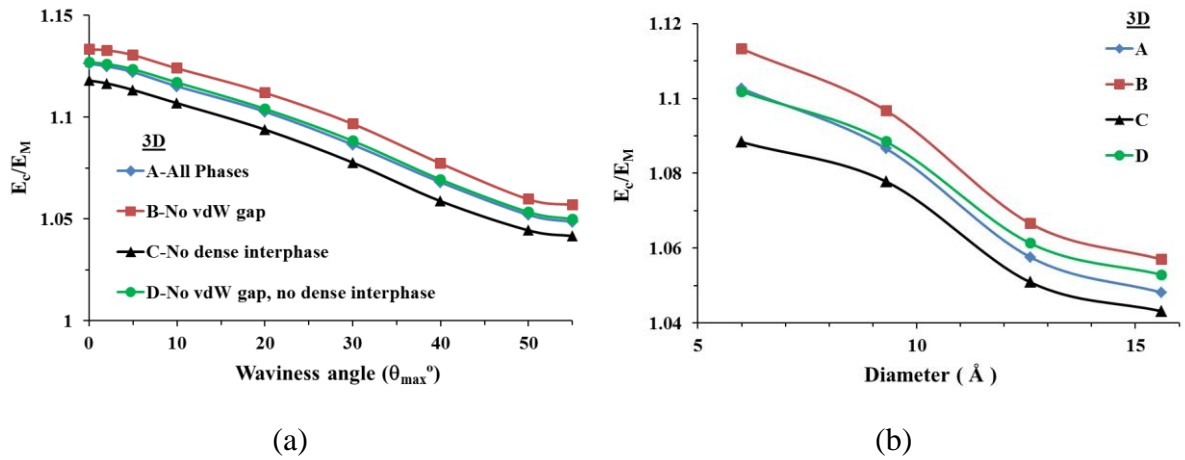


Fig. 8.3 The Young's moduli of CNT-PMCs, E_c , normalised by that of the PVC matrix, E_M , (a) with SWCNT(10,10), and (b) with a variety of SWCNTs from SWCNT (5, 5) to (15, 15) under a given $\theta_{\max}=30^\circ$. The SWCNT volume fraction is 0.5%.

Fig. 8.4a presents the variation of the longitudinal E_c/E_m of the composite with aligned SWCNT (10, 10), that is a 1D-Scheme. It shows that both the vdW gap and the dense interphases can be ignored without a remarkable effect on the overall longitudinal Young's modulus of the composite. Figure 4b illustrates that the result above is consistent in the whole range of SWCNT diameters examined. Moreover, the results in Fig. 8.3 and Fig. 8.4 show that with the same volume fraction, aligned SWCNTs can reinforce the matrix five times that of the randomly distributed ones in the SWCNT alignment direction.

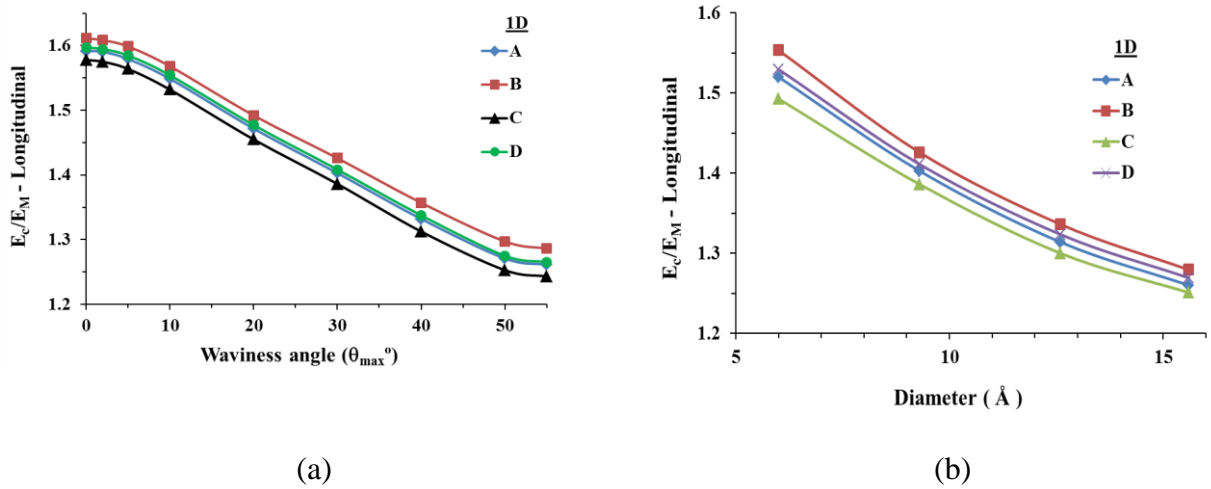


Fig. 8.4 The relative Young's modulus of the composite with aligned SWCNTs. (a) using SWCNT(10,10) but varying θ_{\max} , and (b) using $\theta_{\max} = 30^\circ$ but varying SWCNT diameters.

Fig. 8.5a shows the effect of waviness angle on the transverse E_c/E_m of composites with aligned SWCNT (10, 10). It can be seen that when the waviness angle is small, Scheme (A) consideration (i.e., all interphases included) brings about a greater Young's modulus than the Scheme (D) consideration (without an interphase). The discrepancy vanishes as the waviness angle increases. It is a fact that an SWCNT has small deflection stiffness and a high aspect ratio of length to diameter. Hence, an SWCNT in a composite normally has a high waviness angle [9, 153]. This seems to indicate that the interphase effect on the transverse modulus is negligible in the case of SWCNT (10, 10). Fig. 8.5b shows that for SWCNTs of a diameter smaller than (10, 10), the interphase plays an important role on the transverse modulus. The smaller the diameter, the greater the interphase effect becomes. It must be pointed out further that the present study focuses on non-bonded SWCNT-PMCs only. When chemical bond takes place between functionalized CNTs and matrices, such as those discussed by [19, 174], the mechanical properties of the interphases will change. In

this case, the effects of interphases, waviness and alignment on the macroscopic behaviour of an SWCNT-PMC will also be altered. This will need to be studied further.

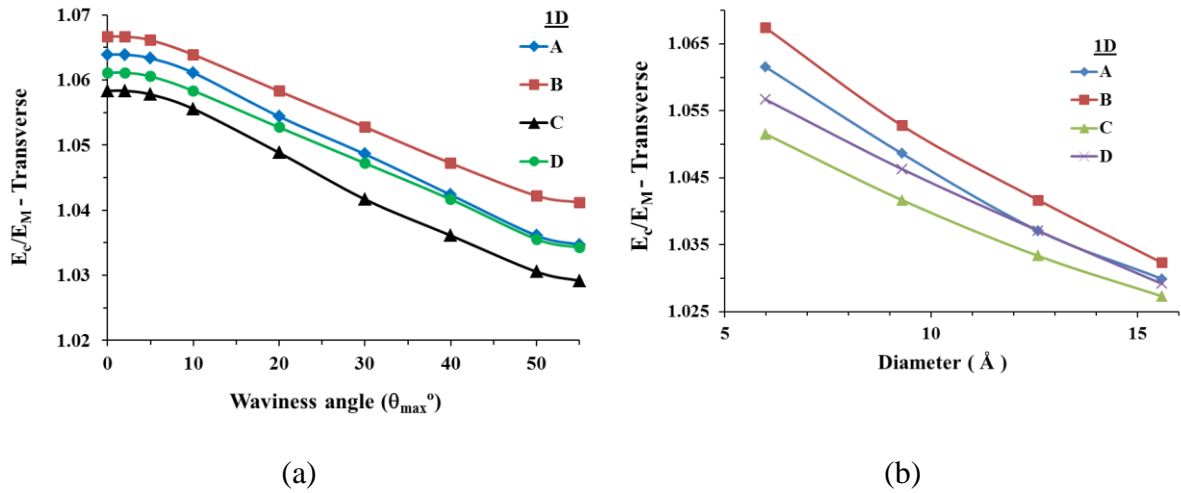


Fig. 8.5 Variation of the relative transverse Young's modulus of composites with aligned SWCNTs. (a) with SWCNT (10, 10), and (b) with the change of SWCNT diameters.

8.4 Conclusion

This chapter has investigated the effects of SWCNT-matrix interphases, SWCNT alignment, and SWCNT waviness on the macroscopic elastic properties of SWCNT-PMCs. A truly multiscale characterization method has been applied to enable an efficient continuum-mechanics analysis involving atomistic effects of the materials. The influential factors studied include the vdW gap, the dense interphase, the waviness of SWCNTs and the nanotube diameter. The study concludes that ignoring the contribution of the vdW gap will overestimate the macroscopic Young's modulus of an SWCNT-PMC, but that neglecting the role of the dense interphase will underestimate the modulus. Ignoring the interphase does not alter the longitudinal Young's modulus of aligned SWCNT-PMCs. In the case of 3D-schemes, the bigger the SWCNT diameter, the greater the effect of

interphase. With a given volume fraction of SWCNTs, aligned ones can reinforce the matrix five times that of the randomly distributed ones.

Chapter 9

Chapter 9

Conclusion and future directions

9.1 Concluding remarks

This dissertation has developed a numerical multiscale strategy to extract elastic properties of non-bonded SWCNT-PMCs. The contributions were reflected in five chapters and the following conclusions can be drawn from each chapter.

9.1.1 Characterization of composite constituents (Chapters 4 and 5)

The constituents include the polymer matrix and the SWCNTs are characterized in two chapters. In Chapter 4, a procedure was proposed to characterize the elastic properties of polymers and the conditions under which MM give acceptable results were discussed. Using MD simulation, the effect of molecular morphology and the CNT additives on the glass transition temperature of polymers were considered. The results showed that MD with COMPASS force field can give rise to acceptable results for physical properties such as density, glass transition temperature and coefficient of thermal expansion; and that the stress analysis based on MM analysis well predicts the elastic constants of glassy polymers. Nevertheless, it fails for soft polymers such as PE. The study concluded that the crystalline part of semi-crystalline polymers is significantly effective on the T_g and should not be ignored in atomistic simulations.

In Chapter 5, using MM simulation, all five independent elastic properties of free-standing armchair SWCNT and SWCNT-clusters were evaluated. The collapse pressure of SWCNT-

clusters and the effect of hydrostatic pressure on their elastic properties were explored. The results showed that the collapse pressure of SWCNT-clusters varies exponentially with increasing the SWCNT diameter. The hydrostatic pressure increases all elastic quantities of SWCNT-clusters, except the transverse Young's modulus, which is not monotonic and remains almost constant in a critical SWCNT diameter. The out-of-plane shear modulus is almost constant for different SWCNT diameters and is the most influenced elastic property by hydrostatic pressure. The study concludes that the out-of-plane Poisson's ratio of free-standing SWCNTs for all ranges of diameters of SWCNTs is close to 1.

9.1.2 Elastic properties of NRVE (Chapter 6)

Using SWCNT-reinforced PVC as an example, in Chapter 6, the atomistic system of CNT and polymer were integrated as an NRVE and equilibrated with the aid of MD then characterized with MM simulation. The NRVE of the SWCNT-PVC system was modelled as an assemblage of three phases, ESF mimicking the SWCNT under the vdW forces, the dense interphase PVC of appropriate thickness and density, and the bulk PVC matrix. Two methods were proposed to extract the elastic properties of the ESF from the atomistic NRVE and the CNT-cluster. This chapter presented a new technique to characterize interphase regions. Using atomistic simulations, the thickness and the average density of the dense interphase matrix were determined and its elastic properties were characterized as a function of density. The method was examined in a continuum-based three-phase model developed with the aid of MM and FE method. The predictions of the continuum-based model showing a good agreement with the atomistic results verifies that the interphase properties of amorphous matrix in CNT-PMCs could be approximated as a function of

density. The results showed that the effect of CNT diameter and internal walls of MWCNTs on the density and thickness of the dense interphase is negligible.

9.1.3 Waviness of CNTs (Chapter 7)

In Chapter 7, a technique was developed for characterizing and modelling the waviness of CNTs in a composite. A reference waviness angle was introduced and quantified through micrograph images. An algorithm was developed to construct corresponding wavy CNTs embedded in a cubic matrix. The generated models were implemented in FE to extract the elastic properties. The study concluded that the developed technique can predict elastic properties of wavy CNT-PMCs accurately, and that the waviness of CNTs can greatly reduce the elastic properties of CNT-PMCs, meanwhile, CNT alignment is a greater parameter affecting the elastic properties of CNT-PMCs. The study showed that even a thin sub-surface image of a CNT-PMC, with a 3D distribution of wavy CNTs, is sufficient to characterize their waviness angle.

9.1.4 The effect of interphase (Chapter 8)

In Chapter 8, the impact of interphase, the diameter and the waviness of SWCNTs on the overall elastic properties of SWCNT-PMCs were studied through a multiscale modelling. The wavy SWCNTs with the interphase were implemented in an FE cubic MRVE. The overall elastic properties were then extracted in a three-dimensional FE analysis. The results conclude that excluding each interphase region gives rise to magnificent discrepancy. However, due to the opposite effect of two interphase regions, ignoring both

interphases does not alter the longitudinal Young's modulus of aligned SWCNT-PMCs and the Young's modulus of 3D-Schemes for the diameters smaller than SWCNT (10, 10). The results show that with a given volume fraction of SWCNTs, aligned ones can reinforce the matrix five times that of the 3D-distributed ones.

9.2 Future directions

The results of this thesis shed light on some unclear issues regarding to the modelling of the elastic properties of CNT-PMCs, however, also open up new horizons in this field.

9.2.1 The effect of large deformation on the overall elastic properties of SWCNT-PMCs

The results of Chapter 5 illustrated that the elastic properties of the SWCNT-clusters is a function of hydrostatic pressure. Moreover, the results of Chapter 6 showed that the ESF could be characterized as a CNT-cluster under a specific hydrostatic pressure. Thus in one sense, ESF is similar to CNT-clusters and their elastic properties vary under a hydrostatic pressure or a large strain. Consequently, any dynamic or static load leading to a large deformation can change the elastic properties of CNT inclusions and their composites. The influence of this phenomenon on the macroscopic elastic properties needs further study.

9.2.2 Analytical solution for the elastic properties of ESF

In Chapter 6, the elastic properties of ESF were obtained numerically which is the only part of the proposed three-phase model that still dependent on the atomistic simulation. There

are some analytical models to characterize elastic properties of free-standing SWCNTs analytically, however, the analytical solution for the elastic properties of the ESF has not been developed yet and needs further studies.

9.2.3 The efficiency of MWCNTs vs. SWCNTs

This thesis concluded that, the waviness of CNTs could reduce the overall elastic properties of CNT-PMCs. Regarding to the higher bending stiffness of MWCNTs, compared to SWCNTs, they are more resistant against bending. However, the waviness and overall elastic properties of CNT-PMCs is affected by a variety of parameters giving rise to two substantial questions: (1) with the same method of production, which CNT brings about a smaller waviness? and (2) with the same volume fraction, regarding their waviness, which CNT is more efficient to reinforce a matrix?

9.2.4 Close contact of CNTs

In this study, a low concentration of CNTs without any close contact was considered. A more general case includes close contact of CNTs with overlapped interphases. The effect of close contact on the interphase region, and consequently on the overall elastic properties of CNT-PMCs needs more detailed discussion.

References

1. Mark, J.E., *Polymer Data Handbook (2nd Edition)*. 2009: Oxford University Press.
2. Chawla, K.K., *Composite Materials: Science and Engineering*. Second ed. 1998: Springer.
3. Iijima, S., *Helical microtubules of graphitic carbon*. *Nature*, 1991. **354**(6348): p. 56-58.
4. Moniruzzaman, M. and K.I. Winey, *Polymer Nanocomposites Containing Carbon Nanotubes*. *Macromolecules*, 2006. **39**(16): p. 5194-5205.
5. Rahmat, M. and P. Hubert, *Carbon nanotube-polymer interactions in nanocomposites: A review*. *Composites Science and Technology*, 2011. **72**(1): p. 72-84.
6. Coleman, J.N., et al., *Small but strong: A review of the mechanical properties of carbon nanotube-polymer composites*. *Carbon*, 2006. **44**(9): p. 1624-1652.
7. Gojny, F.H., et al., *Influence of different carbon nanotubes on the mechanical properties of epoxy matrix composites – A comparative study*. *Composites Science and Technology*, 2005. **65**(15-16): p. 2300-2313.
8. Zhang, L.C., I. Zarudi, and K.Q. Xiao, *Novel behaviour of friction and wear of epoxy composites reinforced by carbon nanotubes*. *Wear*, 2006. **261**(7-8): p. 806-811.
9. Qian, D., et al., *Load transfer and deformation mechanisms in carbon nanotube-polystyrene composites*. *Applied Physics Letters*, 2000. **76**(20): p. 2868-2870.
10. Ci, L. and J. Bai, *The reinforcement role of carbon nanotubes in epoxy composites with different matrix stiffness*. *Composites Science and Technology*, 2006. **66**(3-4): p. 599-603.
11. Spitalsky, Z., et al., *Carbon nanotube-polymer composites: Chemistry, processing, mechanical and electrical properties*. *Progress in Polymer Science*, 2010. **35**(3): p. 357-401.
12. Guo, P., et al., *Fabrication and mechanical properties of well-dispersed multiwalled carbon nanotubes/epoxy composites*. *Composites Science and Technology*, 2007. **67**(15-16): p. 3331-3337.
13. Zhang, S., et al., *Nanocomposites of Carbon Nanotube Fibers Prepared by Polymer Crystallization*. *ACS Applied Materials & Interfaces*, 2010. **2**(6): p. 1642-1647.
14. Omidi, M., et al., *Prediction of the mechanical characteristics of multi-walled carbon nanotube/epoxy composites using a new form of the rule of mixtures*. *Carbon*, 2010. **48**(11): p. 3218-3228.
15. Xiao, K.Q., L.C. Zhang, and I. Zarudi, *Mechanical and rheological properties of carbon nanotube-reinforced polyethylene composites*. *Composites Science and Technology*, 2007. **67**(2): p. 177-182.
16. Zarudi, I. and L.C. Zhang, *Structural evolution of carbon nanotubes in composites under contact sliding stresses*. *Applied Physics Letters*, 2006. **88**(24): p. 243102-3.
17. Gou, J., et al., *Computational analysis of effect of single-walled carbon nanotube rope on molecular interaction and load transfer of nanocomposites*. *Composites Part B: Engineering*, 2005. **36**(6-7): p. 524-533.

-
18. Xiao, K.Q. and L.C. Zhang, *The stress transfer efficiency of a single-walled carbon nanotube in epoxy matrix*. Journal of Materials Science, 2004. **39**(14): p. 4481-4486.
 19. Frankland, S.J.V., et al., *Molecular Simulation of the Influence of Chemical Cross-Links on the Shear Strength of Carbon Nanotube–Polymer Interfaces*. The Journal of Physical Chemistry B, 2002. **106**(12): p. 3046-3048.
 20. Tsai, C.H., et al., *The effect of inclusion waviness and waviness distribution on elastic properties of fiber-reinforced composites*. Composites Part B: Engineering, 2011. **42**(1): p. 62-70.
 21. Fisher, F.T., R.D. Bradshaw, and L.C. Brinson, *Fiber waviness in nanotube-reinforced polymer composites-I: Modulus predictions using effective nanotube properties*. Composites Science and Technology, 2003. **63**(11): p. 1689-1703.
 22. R. Guzman de Villoria and A. Miravete, *Mechanical model to evaluate the effect of the dispersion in nanocomposites*. Acta Materialia, 2007. **55**: p. 3025-3031.
 23. Xiao, K. and L. Zhang, *Effective separation and alignment of long entangled carbon nanotubes in epoxy*. Journal of Materials Science, 2005. **40**(24): p. 6513-6516.
 24. Grujicic, M., Y.P. Sun, and K.L. Koudela, *The effect of covalent functionalization of carbon nanotube reinforcements on the atomic-level mechanical properties of poly-vinyl-ester-epoxy*. Applied Surface Science, 2007. **253**(6): p. 3009-3021.
 25. Odegard, G.M., S.J.V. Frankland, and T.S. Gates, *The effect of chemical functionalization on mechanical properties of nanotube/polymer composites*, in *Structural Dynamics, and Materials Conference*,. 2003, AIAA: Norfolk,VA.
 26. Mylvaganam, K. and L.C. Zhang, *Chemical Bonding in Polyethylene–Nanotube Composites: A Quantum Mechanics Prediction*. The Journal of Physical Chemistry B, 2004. **108**(17): p. 5217-5220.
 27. Tan, H., et al., *The effect of van der Waals-based interface cohesive law on carbon nanotube-reinforced composite materials*. Composites Science and Technology, 2007. **67**(14): p. 2941-2946.
 28. Wan, H., F. Delale, and L. Shen, *Effect of CNT length and CNT-matrix interphase in carbon nanotube (CNT) reinforced composites*. Mechanics Research Communications, 2005. **32**(5): p. 481-489.
 29. Maksimov, R. and E. Plume, *Effect of interphase layers on the elastic properties of a carbon-nanotube-reinforced composite*. Mechanics of Composite Materials, 2011. **47**(3): p. 255-262.
 30. Nemat-Nasser S, H.M., *Micromechanics: overall properties of heterogeneous materials*, ed. 2. 1999, Amsterdam: Elsevier.
 31. Tsai, J.L., S.H. Tzeng, and Y.T. Chiu, *Characterizing elastic properties of carbon nanotubes/polyimide nanocomposites using multi-scale simulation*. Composites Part B: Engineering, 2010. **41**(1): p. 106-115.
 32. Zheng, Q.B., et al., *Effect of chemisorption on the interfacial bonding characteristics of carbon nanotube-polymer composites*. Polymer, 2008. **49**(3): p. 800-808.
 33. Qi, D., J. Hinkley, and G. He, *Molecular dynamics simulation of thermal and mechanical properties of polyimide–carbon-nanotube composites*. Modelling and Simulation in Materials Science and Engineering, 2005. **13**(4): p. 493-507.

-
34. Mylvaganam, K. and L.C. Zhang, *Theoretical Analysis of Nanotube Functionalization and Polymer Grafting*, in *Surface Modification of Nanotube Fillers*. 2011, Wiley-VCH Verlag GmbH & Co. KGaA. p. 91-111.
 35. Zheng, Q., et al., *Computational analysis of effect of modification on the interfacial characteristics of a carbon nanotube-polyethylene composite system*. *Applied Surface Science*, 2009. **255**(6): p. 3534-3543.
 36. Zhu, R., E. Pan, and A.K. Roy, *Molecular dynamics study of the stress-strain behavior of carbon-nanotube reinforced Epon 862 composites*. *Materials Science and Engineering: A*, 2007. **447**(1-2): p. 51-57.
 37. Han, Y. and J. Elliott, *Molecular dynamics simulations of the elastic properties of polymer/carbon nanotube composites*. *Computational Materials Science*, 2007. **39**(2): p. 315-323.
 38. Griebel, M. and J. Hamaekers, *Molecular dynamics simulations of the elastic moduli of polymer-carbon nanotube composites*. *Computer Methods in Applied Mechanics and Engineering*, 2004. **193**(17-20): p. 1773-1788.
 39. Frankland, S.J.V., et al., *The stress-strain behavior of polymer-nanotube composites from molecular dynamics simulation*. *Composites Science and Technology*, 2003. **63**(11): p. 1655-1661.
 40. Shi, D.L., et al., *The Effect of Nanotube Waviness and Agglomeration on the Elastic Property of Carbon Nanotube-Reinforced Composites*. *Journal of Engineering Materials and Technology*, 2004. **126**(3): p. 250-257.
 41. Yang, S., et al., *Nonlinear multiscale modeling approach to characterize elastoplastic behavior of CNT/polymer nanocomposites considering the interphase and interfacial imperfection*. *International Journal of Plasticity*, 2013. **41**(0): p. 124-146.
 42. Yang, S., et al., *Multiscale modeling of size-dependent elastic properties of carbon nanotube/polymer nanocomposites with interfacial imperfections*. *Polymer*, 2012. **53**(2): p. 623-633.
 43. Spanos, P.D. and A. Kotsos, *A multiscale Monte Carlo finite element method for determining mechanical properties of polymer nanocomposites*. *Probabilistic Engineering Mechanics*, 2008. **23**(4): p. 456-470.
 44. Liu, W.K., et al., *An introduction to computational nanomechanics and materials*. *Computer Methods in Applied Mechanics and Engineering*, 2004. **193**(17-20): p. 1529-1578.
 45. Liu, W.K., et al., *Bridging scale methods for nanomechanics and materials*. *Computer Methods in Applied Mechanics and Engineering*, 2006. **195**(13-16): p. 1407-1421.
 46. Schrödinger, E., *An Undulatory Theory of the Mechanics of Atoms and Molecules*. *Physical Review*, 1926. **28**(6): p. 1049-1070.
 47. Sun, H., P. Ren, and J.R. Fried, *The COMPASS force field: parameterization and validation for phosphazenes*. *Computational and Theoretical Polymer Science*, 1998. **8**(1-2): p. 229-246.
 48. Sun, H., *COMPASS: An ab Initio Force-Field Optimized for Condensed-Phase Applications Overview with Details on Alkane and Benzene Compounds*. *The Journal of Physical Chemistry B*, 1998. **102**(38): p. 7338-7364.

-
49. Kausala Mylvaganam , L.C. Zhang, *Possible Chemical Bond Formation between a Carbon Nanotube and Alumina Matrix - A Quantum Mechanics Investigation* Key Engineering Materials, 2010. **443**: p. 723-728.
 50. Lopez, C.F., et al., *Computer simulation studies of biomembranes using a coarse grain model*. Computer Physics Communications, 2002. **147**(1–2): p. 1-6.
 51. Chang, T. and H. Gao, *Size-dependent elastic properties of a single-walled carbon nanotube via a molecular mechanics model*. Journal of the Mechanics and Physics of Solids, 2003. **51**(6): p. 1059-1074.
 52. Shokrieh, M.M. and R. Rafiee, *Prediction of mechanical properties of an embedded carbon nanotube in polymer matrix based on developing an equivalent long fiber*. Mechanics Research Communications, 2010. **37**(2): p. 235-240.
 53. Wernik, J.M. and S.A. Meguid, *Multiscale modeling of the nonlinear response of nano-reinforced polymers*. Acta Mechanica, 2010. **217**(1-2): p. 1-16.
 54. Tadmor, E.B., R. Phillips, and M. Ortiz, *Mixed Atomistic and Continuum Models of Deformation in Solids*. Langmuir, 1996. **12**(19): p. 4529-4534.
 55. Odegard Gregory M., et al., *Equivalent-Continuum Modeling of Nano-Structured Materials*. 2002, NASA Langley Technical Report Server.
 56. Seidel, G.D. and D.C. Lagoudas, *Micromechanical analysis of the effective elastic properties of carbon nanotube reinforced composites*. Mechanics of Materials, 2006. **38**(8-10): p. 884-907.
 57. Saber-Samandari , S. and A. Afaghi- Khatibi, *The effect of interphase on the elastic modulus of polymer based nanocomposites*. Key Engineering Materials, 2006. **312**: p. 199-204.
 58. Odegard, G.M., et al., *Constitutive modeling of nanotube-reinforced polymer composites*. Composites Science and Technology, 2003. **63**(11): p. 1671-1687.
 59. Zeng, Q.H., A.B. Yu, and G.Q. Lu, *Multiscale modeling and simulation of polymer nanocomposites*. Progress in Polymer Science, 2008. **33**(2): p. 191-269.
 60. Rudd, R.E. and J.Q. Broughton, *Concurrent Coupling of Length Scales in Solid State Systems*. physica status solidi (b), 2000. **217**(1): p. 251-291.
 61. Shokrieh, M.M. and R. Rafiee, *On the tensile behavior of an embedded carbon nanotube in polymer matrix with non-bonded interphase region*. Composite Structures, 2010. **92**(3): p. 647-652.
 62. Thostenson, E.T., Z. Ren, and T.-W. Chou, *Advances in the science and technology of carbon nanotubes and their composites: a review*. Composites Science and Technology, 2001. **61**(13): p. 1899-1912.
 63. Saito, R., et al., *Electronic structure of chiral graphene tubules*. Applied Physics Letters, 1992. **60**(18): p. 2204-2206.
 64. Al-Haik, M., M.Y. Hussaini, and H. Garmestani, *Adhesion energy in carbon nanotube-polyethylene composite: Effect of chirality*. Journal of Applied Physics, 2005. **97**(7): p. 074306-5.

-
65. Chang, T., J. Geng, and X. Guo, *Prediction of Chirality- and Size-Dependent Elastic Properties of Single-Walled Carbon Nanotubes via a Molecular Mechanics Model*. Proceedings: Mathematical, Physical and Engineering Sciences, 2006. **462**(2072): p. 2523-2540.
 66. Veedu, V.P., D. Askari, and M.N. Ghasemi-Nejhad, *Chirality Dependence of Carbon Single-Walled Nanotube Material Properties: Axial Young's Modulus*. Journal of Nanoscience and Nanotechnology, 2006. **6**: p. 2159-2166.
 67. Zheng, Q., et al., *Influence of chirality on the interfacial bonding characteristics of carbon nanotube polymer composites*. Journal of Applied Physics, 2008. **103**(4): p. 044302-4.
 68. Imtani, A.N. and V.K. Jindal, *Structure of chiral single-walled carbon nanotubes under hydrostatic pressure*. Computational Materials Science, 2009. **46**(2): p. 297-302.
 69. Goldstein, R.V., *Description of mechanical properties of carbon nanotubes. Tube wall thickness problem. Size effect. part 2*. 2001.
 70. Vodenitcharova, T. and L.C. Zhang, *Effective wall thickness of a single-walled carbon nanotube*. Physical Review B, 2003. **68**(16): p. 165401.
 71. Huang, Y., J. Wu, and K.C. Hwang, *Thickness of graphene and single-wall carbon nanotubes*. Physical Review B, 2006. **74**(24): p. 245413.
 72. Wang, C.Y. and L.C. Zhang, *A critical assessment of the elastic properties and effective wall thickness of single-walled carbon nanotubes*. Nanotechnology, 2008. **19**(7): p. 075705.
 73. Heisenberg, W., *Über den anschaulichen Inhalt der quantentheoretischen Kinematik und Mechanik*. Zeitschrift für Physik, 1927. **43**(3-4): p. 172-198.
 74. Lu, J.P., *Elastic Properties of Carbon Nanotubes and Nanoropes*. Physical Review Letters, 1997. **79**(7): p. 1297-1300.
 75. Hernández, E., et al., *Elastic Properties of C and BxCyNz Composite Nanotubes*. Physical Review Letters, 1998. **80**(20): p. 4502-4505.
 76. Li, C. and T.W. Chou, *A structural mechanics approach for the analysis of carbon nanotubes*. International Journal of Solids and Structures, 2003. **40**(10): p. 2487-2499.
 77. Jin, Y. and F.G. Yuan, *Simulation of elastic properties of single-walled carbon nanotubes*. Composites Science and Technology, 2003. **63**(11): p. 1507-1515.
 78. Yakobson, B.I., C.J. Brabec, and J. Bernholc, *Nanomechanics of Carbon Tubes: Instabilities beyond Linear Response*. Physical Review Letters, 1996. **76**(14): p. 2511.
 79. Xin, Z., Z. Jianjun, and O.-Y. Zhong-can, *Strain energy and Young's modulus of single-wall carbon nanotubes calculated from electronic energy-band theory*. Physical Review B, 2000. **62**(20): p. 13692-13696.
 80. Kudin, K.N., G.E. Scuseria, and B.I. Yakobson, *C2F, BN, and C nanoshell elasticity from ab initio computations*. Physical Review B, 2001. **64**(23): p. 235406.
 81. Tu, Z.C. and Z.C. Ou-Yang, *Single-walled and multiwalled carbon nanotubes viewed as elastic tubes with the effective Young's moduli dependent on layer number*. Physical Review B - Condensed Matter and Materials Physics, 2002. **65**(23): p. 2334071-2334074.

-
82. Pantano, A., D. M. Parks, and M.C. Boyce, *Mechanics of deformation of single- and multi-wall carbon nanotubes*. Journal of the Mechanics and Physics of Solids, 2004. **52**(4): p. 789-821.
 83. Wang, L., et al., *Size Dependence of the Thin-Shell Model for Carbon Nanotubes*. Physical Review Letters, 2005. **95**(10): p. 105501.
 84. Fisher, F.T., R.D. Bradshaw, and L.C. Brinson, *Effects of nanotube waviness on the modulus of nanotube-reinforced polymers*. Applied Physics Letters, 2002. **80**(24): p. 4647-4649.
 85. Li, C. and T.W. Chou, *Failure of carbon nanotube/polymer composites and the effect of nanotube waviness*. Composites Part A: Applied Science and Manufacturing, 2009. **40**(10): p. 1580-1586.
 86. Shen, L. and J. Li, *Transversely isotropic elastic properties of multiwalled carbon nanotubes*. Physical Review B, 2005. **71**(3): p. 035412.
 87. Shen, L. and J. Li, *Transversely isotropic elastic properties of single-walled carbon nanotubes*. Physical Review B, 2004. **69**(4): p. 045414.
 88. Li, H. and W. Guo, *Transversely isotropic elastic properties of single-walled carbon nanotubes by a rectangular beam model for the C[Single Bond]C bonds*. Journal of Applied Physics, 2008. **103**(10): p. 103501-11.
 89. Krishnan, A., et al., *Young's modulus of single-walled nanotubes*. Physical Review B, 1998. **58**(20): p. 14013.
 90. Treacy, M.M.J., T.W. Ebbesen, and J.M. Gibson, *Exceptionally high Young's modulus observed for individual carbon nanotubes*. Nature, 1996. **381**(6584): p. 678-680.
 91. Yu, M.-F., et al., *Strength and Breaking Mechanism of Multiwalled Carbon Nanotubes Under Tensile Load*. Science, 2000. **287**(5453): p. 637-640.
 92. Yu, M.-F., et al., *Tensile Loading of Ropes of Single Wall Carbon Nanotubes and their Mechanical Properties*. Physical Review Letters, 2000. **84**(24): p. 5552-5555.
 93. Pan, Z.W., et al., *Tensile tests of ropes of very long aligned multiwall carbon nanotubes*. Applied Physics Letters, 1999. **74**(21): p. 3152-3154.
 94. Salvetat, J.-P., et al., *Elastic and Shear Moduli of Single-Walled Carbon Nanotube Ropes*. Physical Review Letters, 1999. **82**(5): p. 944-947.
 95. Tomblor, T.W., et al., *Reversible electromechanical characteristics of carbon nanotubes under local-probe manipulation*. Nature, 2000. **405**(6788): p. 769-772.
 96. Wong, E.W., P.E. Sheehan, and C.M. Lieber, *Nanobeam Mechanics: Elasticity, Strength, and Toughness of Nanorods and Nanotubes*. Science, 1997. **277**(5334): p. 1971-1975.
 97. Shokrieh, M.M. and R. Rafiee, *A review of the mechanical properties of isolated carbon nanotubes and carbon nanotube composites*. Mechanics of Composite Materials, 2010. **46**(2): p. 155-172.
 98. Robertson, D.H., D.W. Brenner, and J.W. Mintmire, *Energetics of nanoscale graphitic tubules*. Physical Review B, 1992. **45**(21): p. 12592-12595.
 99. Cornwell, C.F. and L.T. Wille, *Elastic properties of single-walled carbon nanotubes in compression*. Solid State Communications, 1997. **101**(8): p. 555-558.

-
100. Halicioglu, T., *Stress calculations for carbon nanotubes*. Thin Solid Films, 1998. **312**(1–2): p. 11-14.
 101. Yao, N. and V. Lordi, *Young's modulus of single-walled carbon nanotubes*. Journal of Applied Physics, 1998. **84**(4): p. 1939-1943.
 102. Prylutsky, Y.I., et al., *Molecular dynamics simulation of mechanical, vibrational and electronic properties of carbon nanotubes*. Computational Materials Science, 2000. **17**(2–4): p. 352-355.
 103. Liew, K.M., X.Q. He, and C.H. Wong, *On the study of elastic and plastic properties of multi-walled carbon nanotubes under axial tension using molecular dynamics simulation*. Acta Materialia, 2004. **52**(9): p. 2521-2527.
 104. Duan, W.H., et al., *Molecular mechanics modeling of carbon nanotube fracture*. Carbon, 2007. **45**(9): p. 1769-1776.
 105. Hernández, E., et al., *Elastic properties of single-wall nanotubes*. Applied Physics A, 1999. **68**(3): p. 287-292.
 106. Van Lier, G., et al., *Ab initio study of the elastic properties of single-walled carbon nanotubes and graphene*. Chemical Physics Letters, 2000. **326**(1–2): p. 181-185.
 107. Chandraseker, K. and S. Mukherjee, *Atomistic-continuum and ab initio estimation of the elastic moduli of single-walled carbon nanotubes*. Computational Materials Science, 2007. **40**(1): p. 147-158.
 108. Sánchez-Portal, D., et al., *Ab initio structural, elastic, and vibrational properties of carbon nanotubes*. Physical Review B, 1999. **59**(19): p. 12678-12688.
 109. Wilson, N.R. and J.V. Macpherson, *Carbon nanotube tips for atomic force microscopy*. Nat Nano, 2009. **4**(8): p. 483-491.
 110. Thess, A., et al., *Crystalline Ropes of Metallic Carbon Nanotubes*. Science, 1996. **273**(5274): p. 483-7.
 111. Shang, Y., et al., *Super-stretchable spring-like carbon nanotube ropes*. Adv Mater, 2012. **24**(21): p. 2896-900.
 112. Lee, N.S., et al., *Application of carbon nanotubes to field emission displays*. Diamond and Related Materials, 2001. **10**(2): p. 265-270.
 113. Candelaria, S.L., et al., *Nanostructured carbon for energy storage and conversion*. Nano Energy, 2012. **1**(2): p. 195-220.
 114. Kim, T., et al., *In situ fabrication of freestanding single-walled carbon nanotube rope interconnection*. physica status solidi (a), 2012. **209**(11): p. 2179-2185.
 115. Tersoff, J. and R.S. Ruoff, *Structural Properties of a Carbon-Nanotube Crystal*. Physical Review Letters, 1994. **73**(5): p. 676-679.
 116. Saether, E., S.J.V. Frankland, and R.B. Pipes, *Transverse mechanical properties of single-walled carbon nanotube crystals. Part I: determination of elastic moduli*. Composites Science and Technology, 2003. **63**(11): p. 1543-1550.

-
117. Chengxiang, L., et al., *Interfacial shear strengths between carbon nanotubes*. Nanotechnology, 2010. **21**(11): p. 115704.
 118. Popov, V.N., V.E. Van-Doren, and M. Balkanski, *Elastic properties of crystals of single-walled carbon nanotubes*. Solid State Communications, 2000. **114**(7): p. 395-399.
 119. Liu, J.Z., et al., *Mechanical properties of single-walled carbon nanotube bundles as bulk materials*. Journal of the Mechanics and Physics of Solids, 2005. **53**(1): p. 123-142.
 120. Talukdar, K. and A.K. Mitra, *Changes in Mechanical Properties and Fracture Behavior of Single Wall Carbon Nanotubes on Bundle Formation*. Journal of Computational and Theoretical Nanoscience, 2011. **8**(9): p. 1882-1887.
 121. Mylvaganam, K. and L.C. Zhang, *Nano-Friction of Some Carbon Allotropes*. Journal of Computational and Theoretical Nanoscience, 2010. **7**(10): p. 2199-2202.
 122. Popov, V.N., V.E. Van Doren, and M. Balkanski, *Lattice dynamics of single-walled carbon nanotubes*. Physical Review B, 1999. **59**(13): p. 8355-8358.
 123. Loa, I., *Raman spectroscopy on carbon nanotubes at high pressure*. Journal of Raman Spectroscopy, 2003. **34**(7-8): p. 611-627.
 124. Aguiar, A.L., et al., *Pressure-Induced Collapse in Double-Walled Carbon Nanotubes: Chemical and Mechanical Screening Effects*. The Journal of Physical Chemistry C, 2011. **115**(13): p. 5378-5384.
 125. Peters, M.J., et al., *Structural phase transition in carbon nanotube bundles under pressure*. Physical Review B, 2000. **61**(9): p. 5939-5944.
 126. Sluiter, M.H.F., V. Kumar, and Y. Kawazoe, *Symmetry-driven phase transformations in single-wall carbon-nanotube bundles under hydrostatic pressure*. Physical Review B, 2002. **65**(16): p. 161402.
 127. Yang, X., G. Wu, and J. Dong, *Structural transformations of double-walled carbon nanotube bundle under hydrostatic pressure*. Applied Physics Letters, 2006. **89**(11): p. 113101-3.
 128. Reich, S., C. Thomsen, and P. Ordejón, *Elastic properties of carbon nanotubes under hydrostatic pressure*. Physical Review B, 2002. **65**(15): p. 153407.
 129. Peacock, A.J., *Handbook of Polyethylene- Structures , properties and applications*. 2002, New York: Marcel Dekker.
 130. Wang, T.T., *Morphology and mechanical properties of crystalline polymers. I. Transcrystalline polyethylene*. Journal of Applied Physics, 1973. **44**(5): p. 2218-2224.
 131. Ward, I.M. and J. Sweeney, *An Introduction to the Mechanical Properties of Solid Polymers*, ed. 2nd. 2004: John Wiley & Sons Ltd.
 132. Herasati, S., H.H. Ruan, and L.C. Zhang, *Effect of chain morphology and carbon-nanotube additives on the glass transition temperature of polyethylene*. Journal of Nano Research, 2013. **23**: p. 16-23.
 133. Anand, S., et al., *Molecular dynamics simulation based evaluation of glass transition temperatures of polystyrene in the presence of carbon dioxide*. Modelling and Simulation in Materials Science and Engineering, 2010. **18**(6): p. 065003.

-
134. Han, J., R.H. Gee, and R.H. Boyd, *Glass Transition Temperatures of Polymers from Molecular Dynamics Simulations*. *Macromolecules*, 1994. **27**(26): p. 7781-7784.
135. Theodorou, D.N. and U.W. Suter, *Atomistic modeling of mechanical properties of polymeric glasses*. *Macromolecules*, 1986. **19**(1): p. 139-154.
136. Richard H, B., *Relaxation processes in crystalline polymers: experimental behaviour — a review*. *Polymer*, 1985. **26**(3): p. 323-347.
137. Graff, M.S. and R.H. Boyd, *A dielectric study of molecular relaxation in linear polyethylene*. *Polymer*, 1994. **35**(9): p. 1797-1801.
138. Stehling, F.C. and L. Mandelkern, *The Glass Temperature of Linear Polyethylene*. *Macromolecules*, 1970. **3**(2): p. 242-252.
139. Woodward, A.E., et al., *The dynamic mechanical behavior of some nylons*. *Journal of Colloid Science*, 1957. **12**(4): p. 363-377.
140. Koyama, A., et al., *Molecular dynamics studies on local ordering in amorphous polyethylene*. *The Journal of Chemical Physics*, 2001. **115**(1): p. 560-566.
141. Reynaud, E., C. Gauthier, and J. Perez, *Nanophases in polymers*. *Revue de Metallurgie. Cahiers D'Informations Techniques*, 1999. **96**(2): p. 169-176.
142. Odegard, G.M., T.C. Clancy, and T.S. Gates, *Modeling of the mechanical properties of nanoparticle/polymer composites*. *Polymer*, 2005. **46**(2): p. 553-562.
143. Herasati, S., L.C. Zhang, and H.H. Ruan, *A new method for characterizing the interphase regions of carbon nanotube composites*. *International Journal of Solids and Structures*, 2014. **51**(9): p. 1781-1791.
144. Hu, N., et al., *Prediction of elastic properties of carbon nanotube reinforced composites*. *Proceedings of the Royal Society A: Mathematical, Physical and Engineering Science*, 2005. **461**(2058): p. 1685-1710.
145. Wang, H.W., et al., *Nanoreinforced polymer composites: 3D FEM modeling with effective interface concept*. *Composites Science and Technology*, 2011. **71**(7): p. 980-988.
146. Rafiee, R., et al., *Challenges of the Modeling Methods for Investigating the Interaction between the CNT and the Surrounding Polymer*. *Advances in Materials Science and Engineering*, 2013. **2013**: p. 1-10.
147. Salviato, M., M. Zappalorto, and M. Quaresimin, *Nanoparticle debonding strength: A comprehensive study on interfacial effects*. *International Journal of Solids and Structures*, 2013. **50**(20-21): p. 3225-3232.
148. Boutaleb, S., et al., *Micromechanics-based modelling of stiffness and yield stress for silica/polymer nanocomposites*. *International Journal of Solids and Structures*, 2009. **46**(7-8): p. 1716-1726.
149. Paliwal, B. and M. Cherkaoui, *Estimation of anisotropic elastic properties of nanocomposites using atomistic-continuum interphase model*. *International Journal of Solids and Structures*, 2012. **49**(18): p. 2424-2438.

-
150. Yu, S., S. Yang, and M. Cho, *Multi-scale modeling of cross-linked epoxy nanocomposites*. Polymer, 2009. **50**(3): p. 945-952.
 151. Papakonstantopoulos, G.J., et al., *Local mechanical properties of polymeric nanocomposites*. Physical Review E, 2005. **72**(3): p. 031801.
 152. Frankland, S.J.V. and T.S. Gates, *Local Elastic Constants For Epoxy-Nanotube Composites From Molecular Dynamics Simulation*. MRS Online Proceedings Library, 2007. **1056**: p. null-null.
 153. Shaffer, M.S.P. and A.H. Windle, *Fabrication and Characterization of Carbon Nanotube/Poly(vinyl alcohol) Composites*. Advanced Materials, 1999. **11**(11): p. 937-941.
 154. Pantano, A. and F. Cappello, *Numerical model for composite material with polymer matrix reinforced by carbon nanotubes*. Meccanica, 2008. **43**(2): p. 263-270.
 155. Bradshaw, R.D., F.T. Fisher, and L.C. Brinson, *Fiber waviness in nanotube-reinforced polymer composites--II: modeling via numerical approximation of the dilute strain concentration tensor*. Composites Science and Technology, 2003. **63**(11): p. 1705-1722.
 156. Shao, L.H., et al., *Prediction of effective moduli of carbon nanotube-reinforced composites with waviness and debonding*. Composite Structures, 2009. **87**(3): p. 274-281.
 157. Pantano, A. and P. Mantione, *A numerical-analytical model for the characterization of composites reinforced by carbon nanotubes*. Applied Physics A: Materials Science & Processing, 2010. **99**(4): p. 895-902.
 158. Shady, E. and Y. Gowayed, *Effect of nanotube geometry on the elastic properties of nanocomposites*. Composites Science and Technology, 2010. **70**(10): p. 1476-1481.
 159. Nafar Dastgerdi, J., G. Marquis, and M. Salimi, *The effect of nanotubes waviness on mechanical properties of CNT/SMP composites*. Composites Science and Technology, 2013. **86**(0): p. 164-169.
 160. Joshi, U.A., S.C. Sharma, and S.P. Harsha, *Effect of waviness on the mechanical properties of carbon nanotube based composites*. Physica E: Low-dimensional Systems and Nanostructures, 2011. **43**(8): p. 1453-1460.
 161. Clarke, A.R., G. Archenhold, and N.C. Davidson, *A novel technique for determining the 3D spatial distribution of glass fibres in polymer composites*. Composites Science and Technology, 1995. **55**(1): p. 75-91.
 162. Motamedi, M., M. Eskandari, and M. Yeganeh, *Effect of straight and wavy carbon nanotube on the reinforcement modulus in nonlinear elastic matrix nanocomposites*. Materials & Design, 2012. **34**(0): p. 603-608.
 163. Mori, T. and K. Tanaka, *Average stress in matrix and average elastic energy of materials with misfitting inclusions*. Acta Metallurgica, 1973. **21**(5): p. 571-574.
 164. Halpin, J.C., *Effects of environmental factors on composite materials*. AFML-TR-67-423, 1969.
 165. Yeh, M.-K., N.-H. Tai, and J.-H. Liu, *Mechanical behavior of phenolic-based composites reinforced with multi-walled carbon nanotubes*. Carbon, 2006. **44**(1): p. 1-9.

-
166. Anumandla, V. and R.F. Gibson, *A comprehensive closed form micromechanics model for estimating the elastic modulus of nanotube-reinforced composites*. Composites Part A: Applied Science and Manufacturing, 2006. **37**(12): p. 2178-2185.
167. Bhuiyan, M.A., et al., *Understanding the effect of CNT characteristics on the tensile modulus of CNT reinforced polypropylene using finite element analysis*. Computational Materials Science, 2013. **79**(0): p. 368-376.
168. Misiego, C.R. and R.B. Pipes, *Dispersion and its relation to carbon nanotube concentration in polyimide nanocomposites*. Composites Science and Technology, 2013. **85**(0): p. 43-49.
169. Wernik, J.M. and S.A. Meguid, *Recent Developments in Multifunctional Nanocomposites Using Carbon Nanotubes*. Applied Mechanics Reviews, 2010. **63**(5): p. 050801-40.
170. Hu, H., et al., *Characterizing and Modeling Mechanical Properties of Nanocomposites-Review and Evaluation* Journal of Minerals & Materials Characterization and Engineering, 2010. **9**(4): p. 275-319.
171. Gao, X.L. and K. Li, *A shear-lag model for carbon nanotube-reinforced polymer composites*. International Journal of Solids and Structures, 2005. **42**(5-6): p. 1649-1667.
172. Joshi, U.A., S.C. Sharma, and S.P. Harsha, *Effect of carbon nanotube orientation on the mechanical properties of nanocomposites*. Composites Part B: Engineering, 2012. **43**(4): p. 2063-2071.
173. Giannopoulos, G.I., S.K. Georgantzinis, and N.K. Anifantis, *A semi-continuum finite element approach to evaluate the Young's modulus of single-walled carbon nanotube reinforced composites*. Composites Part B: Engineering, 2010. **41**(8): p. 594-601.
174. Mylvaganam, K., L.C. Zhang, and W.C.D. Cheong, *The Effect of Interface Chemical Bonds on the Behaviour of Nanotube-Polyethylene Composites Under Nano-Particle Impacts*. Journal of Computational and Theoretical Nanoscience, 2007. **4**(1): p. 122-126.
175. Hu, N., et al., *Prediction of buckling characteristics of carbon nanotubes*. International Journal of Solids and Structures, 2007. **44**(20): p. 6535-6550.
176. *Materials Studio, Accelrys Inc. User's manual*.
177. Born, M. and J.R. Oppenheimer, *Zur Quantentheorie der Molekeln*. Ann. Phys., 1927. **84**.
178. G. Szefer and D. Jasinska, *Modeling of strains and stresses of material nanostructures*. Bulletin of the Polish Academy of Sciences: Technical Sciences, 2009. **57**(1): p. 41-46.
179. Zimmerman, J.A. and et al., *Calculation of stress in atomistic simulation*. Modelling and Simulation in Materials Science and Engineering, 2004. **12**(4): p. S319.
180. Bin Liu and Xinming Qiu *How to compute the atomic stress objectively?* Journal of Computational and Theoretical Nanoscience, 2009. **6**: p. 1081-1089.
181. Monticelli, L., et al., *The MARTINI Coarse-Grained Force Field: Extension to Proteins*. Journal of Chemical Theory and Computation, 2008. **4**(5): p. 819-834.
182. Kuang, Y.D. and X.Q. He, *Young's moduli of functionalized single-wall carbon nanotubes under tensile loading*. Composites Science and Technology, 2009. **69**(2): p. 169-175.

-
183. Al-Ostaz, A., et al., *Molecular dynamics simulation of SWCNT-polymer nanocomposite and its constituents*. Journal of Materials Science, 2008. **43**(1): p. 164-173.
184. Wang, Q., et al., *Modeling of fracture of carbon nanotubes with vacancy defect*. Physical Review B, 2007. **75**(20): p. 201405.
185. Wu, C. and W. Xu, *Atomistic molecular modelling of crosslinked epoxy resin*. Polymer, 2006. **47**(16): p. 6004-6009.
186. Mashapa, M.G. and S.S. Ray, *Molecular Dynamics Simulation Studies of Structural and Mechanical Properties of Single-Walled Carbon Nanotubes*. Journal of Nanoscience and Nanotechnology, 2010. **10**(12): p. 8083-8087.
187. Wentzcovitch, R.M., *Invariant molecular-dynamics approach to structural phase transitions*. Physical Review B, 1991. **44**(5): p. 2358-2361.
188. Berendsen, H.J.C., et al., *Molecular dynamics with coupling to an external bath*. The Journal of Chemical Physics, 1984. **81**(8): p. 3684-3690.
189. Nosé, S., *A molecular dynamics method for simulations in the canonical ensemble*. Molecular Physics, 1984. **52**(2): p. 255-268.
190. Nosé, S., *A unified formulation of the constant temperature molecular dynamics methods*. The Journal of Chemical Physics, 1984. **81**(1): p. 511-519.
191. Shuichi, N., *Constant Temperature Molecular Dynamics Methods*. Progress of Theoretical Physics Supplement, 1991. **103**: p. 1-46.
192. Chen, W.-F. and D.-J. Han, *Plasticity for Structural Engineers*. 2007: J. Ross Publishing.
193. Zhou, M., *A New Look at the Atomic Level Virial Stress: On Continuum-Molecular System Equivalence*. Proceedings: Mathematical, Physical and Engineering Sciences, 2003. **459**(2037): p. 2347-2392.
194. Allen, M.P. and D.J. Tildesley, *Computer Simulation of Liquids*. 1989: Oxford University Press.
195. Subramaniyan, A.K. and C.T. Sun, *Continuum interpretation of virial stress in molecular simulations*. International Journal of Solids and Structures, 2008. **45**(14-15): p. 4340-4346.
196. Parrinello, M. and A. Rahman, *Polymorphic transitions in single crystals: A new molecular dynamics method*. Journal of Applied Physics, 1981. **52**(12): p. 7182-7190.
197. Andersen, H.C., *Molecular dynamics simulations at constant pressure and/or temperature*. The Journal of Chemical Physics, 1980. **72**(4): p. 2384-2393.
198. Theodorou, D.N. and U.W. Suter, *Detailed molecular structure of a vinyl polymer glass*. Macromolecules, 1985. **18**(7): p. 1467-1478.
199. Ewald, P.P., *Evaluation of optical and electrostatic lattice potentials*. Ann. Phys., 1921. **64**.
200. Tosi, M.P., *Cohesion of Ionic Solids in the Born Model*. Solid State Physics-Advances in Research and Applications, 1964. **16**: p. 1-120.

-
201. Karasawa, N. and W.A. Goddard, *Acceleration of convergence for lattice sums*. The Journal of Physical Chemistry, 1989. **93**(21): p. 7320-7327.
202. Sperling, L.H., *Introduction to Physical Polymer Science*, ed. t. Edition. 2005: John Wiley & Sons, Inc.
203. Wei, C., D. Srivastava, and K. Cho, *Thermal Expansion and Diffusion Coefficients of Carbon Nanotube-Polymer Composites*. Nano Letters, 2002. **2**(6): p. 647-650.
204. Wu, R., et al., *Conformational Transition Behavior of Amorphous Polyethylene across the Glass Transition Temperature*. The Journal of Physical Chemistry B, 2009. **113**(27): p. 9077-9083.
205. Liu, J. and Q. Yang, *Molecular dynamics simulation for mechanical properties of CNT/Polyethylene composites*. Journal of Physics: Conference Series, 2009. **188**(1): p. 012052.
206. Mylvaganam, K. and L.C. Zhang, *Simulation of chemically bonded nanotube-polyethylene composites subjected to mechanical loading*, in *5th Australasian Congress on Applied Mechanics (ACAM 2007)* M. Veidt, et al., Editors. 2007, Engineers Australia Brisbane, Australia p. 5.
207. Meysam Rahmat and Pascal Hubert, *Molecular Dynamics Simulation of Single-Walled Carbon Nanotube – PMMA Interaction*. Journal of Nano Research 2012. **18-19**: p. 117-128.
208. Meirovitch, H., *Computer simulation of self-avoiding walks: Testing the scanning method*. The Journal of Chemical Physics, 1983. **79**(1): p. 502-508.
209. Vasiliev, V.V. and E.V. Morozov, *Mechanics and Analysis of Composite Materials*. 2001: Elsevier Science Ltd.
210. Jones, R.M., *mechanics of composite materials*. 1999, Hemisphere Publishing Corporation: New York
211. Tsai, D.H., *The virial theorem and stress calculation in molecular dynamics*. The Journal of Chemical Physics, 1979. **70**(3): p. 1375-1382.
212. Titow, W.V., *PVC Technology*. 1984: Springer
213. Brown, D., et al., *The preparation of polymer melt samples for computer simulation studies*. The Journal of Chemical Physics, 1994. **100**(8): p. 6011-6018.
214. Dymont, J. and H. Ziebland, *The tensile properties of some plastics at low temperatures*. Journal of Applied Chemistry, 1958. **8**(4): p. 203-206.
215. <http://www2.shimadzu.com/applications/Autograph/MeasurementPoissonsRatioPVC.pdf>.
216. <http://www.goodfellow.com/PDF/TAB301X.pdf>.
217. Popov, M., et al., *Superhard phase composed of single-wall carbon nanotubes*. Physical Review B, 2002. **65**(3): p. 033408.
218. Merlen, A., et al., *High pressure–high temperature synthesis of diamond from single-wall pristine and iodine doped carbon nanotube bundles*. Carbon, 2009. **47**(7): p. 1643-1651.
219. Popov, V.N. and V.E.V. Doren, *Elastic properties of single-walled carbon nanotubes*. Phy. Rev., 2000. **61**(4): p. 3078-3084.

220. Lasjaunias, J.C., et al., *Low-energy vibrational excitations in carbon nanotubes studied by heat capacity*. Nanotechnology, 2003. **14**(9): p. 998.
221. Gings, N.J., W. Chen, and S.K. Sitaraman, *Waviness reduces effective modulus of carbon nanotube forests by several orders of magnitude*. Carbon, 2013(0).
222. Herasati, S. and L.C. Zhang, *Elastic properties of single-walled carbon nanotube clusters: Dependence on hydrostatic pressure*. Computational Materials Science, 2014. **86**(0): p. 93-98.

Appendix

Appendix 1. Stiffness matrix

The stiffness matrix for orthotropic materials, has 9 independent parameters as

$$C = \begin{pmatrix} C_{11} & C_{12} & C_{13} & 0 & 0 & 0 \\ C_{12} & C_{22} & C_{23} & 0 & 0 & 0 \\ C_{13} & C_{23} & C_{33} & 0 & 0 & 0 \\ 0 & 0 & 0 & C_{44} & 0 & 0 \\ 0 & 0 & 0 & 0 & C_{55} & 0 \\ 0 & 0 & 0 & 0 & 0 & C_{66} \end{pmatrix} \cdot \quad \text{Eq. A1. 1}$$

The elastic constants for orthotropic materials, could be obtained from compliance matrix which is the inverse of the stiffness matrix

$$S = C^{-1} = \begin{pmatrix} \frac{1}{E_{xx}} & -\frac{\nu_{yx}}{E_{yy}} & -\frac{\nu_{zx}}{E_{zz}} & 0 & 0 & 0 \\ -\frac{\nu_{xy}}{E_{xx}} & \frac{1}{E_{yy}} & -\frac{\nu_{zy}}{E_{zz}} & 0 & 0 & 0 \\ -\frac{\nu_{yx}}{E_{xx}} & -\frac{\nu_{yz}}{E_{yy}} & \frac{1}{E_{zz}} & 0 & 0 & 0 \\ 0 & 0 & 0 & \frac{1}{G_{yz}} & 0 & 0 \\ 0 & 0 & 0 & 0 & \frac{1}{G_{zx}} & 0 \\ 0 & 0 & 0 & 0 & 0 & \frac{1}{G_{xy}} \end{pmatrix} \cdot \quad \text{Eq. A1. 2}$$

Transversely isotropic materials have five independent parameters as

$$C = \begin{pmatrix} C_{11} & C_{12} & C_{13} & 0 & 0 & 0 \\ C_{12} & C_{11} & C_{13} & 0 & 0 & 0 \\ C_{12} & C_{13} & C_{33} & 0 & 0 & 0 \\ 0 & 0 & 0 & C_{44} & 0 & 0 \\ 0 & 0 & 0 & 0 & C_{44} & 0 \\ 0 & 0 & 0 & 0 & 0 & (C_{11} - C_{12})/2 \end{pmatrix} \cdot \quad \text{Eq. A1. 3}$$

Elastic constants are easily obtained from the compliance matrix includes longitudinal and transverse Young's moduli (E_{zz} , E_{xx}), in-plane and out-off-plane Poisson's ratio (ν_{zx} , ν_{xy})

and out-of-plane shear modulus (G_{zx}). The relation below gives a direct answer for five elastic constants.

$$S = C^{-1} = \begin{pmatrix} \frac{1}{E_{xx}} & -\frac{\nu_{yx}}{E_{xx}} & -\frac{\nu_{zx}}{E_{zz}} & 0 & 0 & 0 \\ -\frac{\nu_{xy}}{E_{xx}} & \frac{1}{E_{xx}} & -\frac{\nu_{zx}}{E_{zz}} & 0 & 0 & 0 \\ \frac{\nu_{yx}}{E_{xx}} & -\frac{\nu_{xz}}{E_{zz}} & \frac{1}{E_{zz}} & 0 & 0 & 0 \\ 0 & 0 & 0 & \frac{1}{G_{yz}} & 0 & 0 \\ 0 & 0 & 0 & 0 & \frac{1}{G_{yz}} & 0 \\ 0 & 0 & 0 & 0 & 0 & \frac{2(1+\nu_{xy})}{E_{xx}} \end{pmatrix}. \quad \text{Eq. A1.4}$$

Finally, the stiffness matrix for isotropic materials has only two independent parameters of Young's modulus E and Poisson's ratio ν ,

$$C = \frac{E}{(1+\nu)(1-2\nu)} \begin{pmatrix} 1-\nu & \nu & \nu & 0 & 0 & 0 \\ \nu & 1-\nu & \nu & 0 & 0 & 0 \\ \nu & \nu & 1-\nu & 0 & 0 & 0 \\ 0 & 0 & 0 & 1-2\nu & 0 & 0 \\ 0 & 0 & 0 & 0 & 1-2\nu & 0 \\ 0 & 0 & 0 & 0 & 0 & 1-2\nu \end{pmatrix}. \quad \text{Eq. A1.5}$$

Appendix 2. Energy terms of COMPASS force field

A general expression of valence energy includes five terms of bond stretching (E_{bond}), valance angle bending (E_{bend}), dihedral angle torsion ($E_{torsion}$), inversion which is also known as out-of-plane interactions (E_{oop}), and Urey-Bradley term representing the interactions between two atoms that are bonded to a common atom (E_{UB}). A schematic diagram of the first four terms of valence energy is shown in Fig. A. 1.

$$E_{valance} = E_{bond} + E_{angle} + E_{bend} + E_{oop} + E_{UB} \quad \text{Eq. A2.1}$$

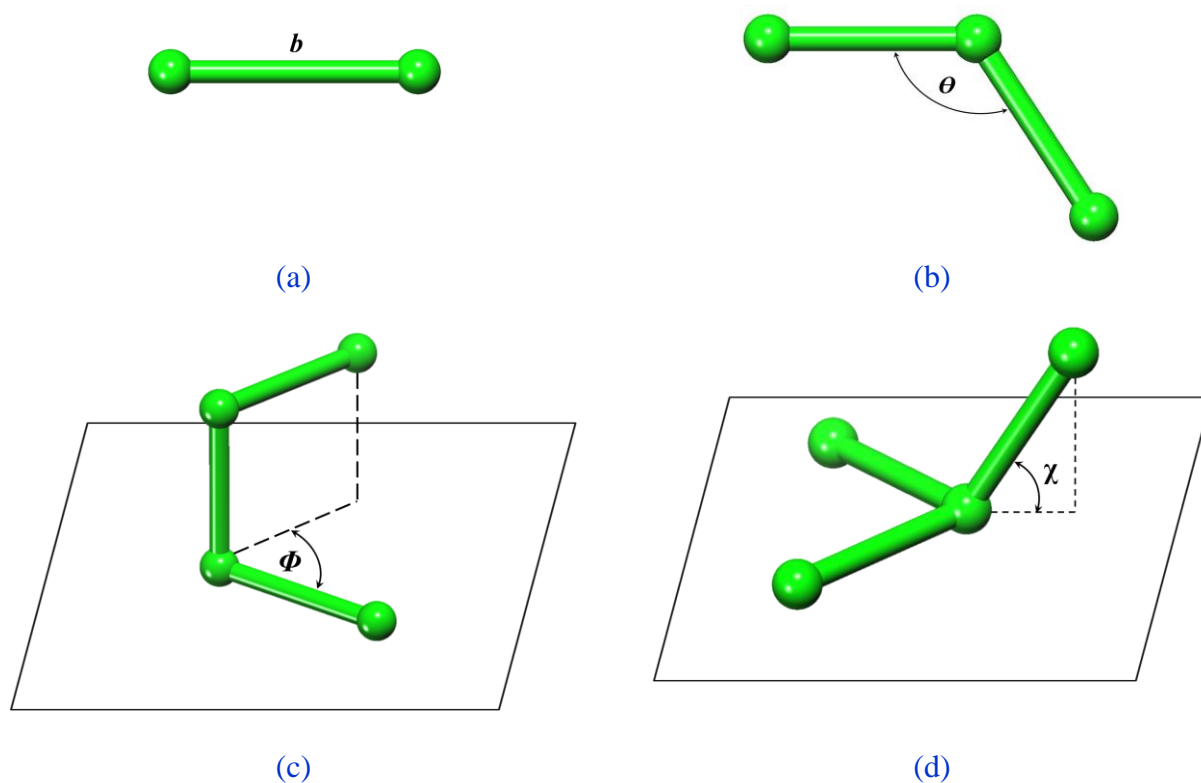


Fig. A. 1 Valence atomic interactions (a) stretching, (b) angle bending, (c) angle torsion, and (d) inversion.

The cross-coupling terms are dependent on the number and connectivity of the atoms that are involved in the functions. Cross-coupling includes the following seven terms: stretch-stretch interaction between two adjacent bonds ($E_{bond-bond}$); stretch-bend ($E_{bond-bend}$); bend-bend interactions ($E_{angle-bend}$); stretch-torsion interactions between a dihedral angle and one of its end bonds ($E_{end-bond-bend}$); and its middle bond ($E_{end-bond-bend}$); bend-torsion interactions between a dihedral angle and one of its valence angles ($E_{angle-bend}$); and bend-bend-torsion interactions between a dihedral angle and its two valence angles ($E_{bend-bend-torsion}$).

$$\begin{aligned}
E_{cross-terms} &= E_{bond-bond} + E_{bend-bend} + E_{bond-bend} \\
&\quad + E_{end_bond-bend} + E_{middle_bond-torsion} \\
&\quad + E_{bend-torsion} + E_{bend-bend-torsion}
\end{aligned}
\tag{Eq. A2. 2}$$

The non-bonded energy involves, van der Waals (E_{vdW}), electrostatic ($E_{Coulomb}$) and hydrogen bonds (E_{H-bond}).

$$E_{non-bond} = E_{vdW} + E_{Coulomb} + E_{H-bond} \tag{Eq. A2. 3}$$

The energy components explained in Eq. A2. 1 to Eq. A2. 3 can be expanded in Eq. A2. 4 to Eq. A2. 16.

$$E_{bond} = \sum_b [K_2(b - b_0)^2 + K_3(b - b_0)^3 + K_4(b - b_0)^4] \tag{Eq. A2. 4}$$

$$E_{angle} = \sum_\theta [H_2(\theta - \theta_0)^2 + H_3(\theta - \theta_0)^3 + H_4(\theta - \theta_0)^4] \tag{Eq. A2. 5}$$

$$\begin{aligned}
E_{torsion} &= \sum_b [V_1[1 - \cos(\phi - \phi_1^0)] + V_2[1 - \cos(2\phi - \phi_2^0)] \\
&\quad + V_3[1 - \cos(3\phi - \phi_3^0)]]
\end{aligned}
\tag{Eq. A2. 6}$$

$$E_{bond} = \sum_x K_x \chi^2 \tag{Eq. A2. 7}$$

$$E_{bond-bond} = \sum_b \sum_{b'} F_{bb'}(b - b_0)(b' - b'_0) \tag{Eq. A2. 8}$$

$$E_{angle-angle} = \sum_\theta \sum_{\theta'} F_{\theta\theta'}(\theta - \theta_0)(\theta' - \theta'_0) \tag{Eq. A2. 9}$$

$$E_{bond-angle} = \sum_b \sum_\theta F_{b\theta}(b - b_0)(\theta - \theta_0) \tag{Eq. A2. 10}$$

$$E_{end_bond_torsion} = \sum_b \sum_{\phi} F_{b\phi} (b - b_0) [V_1 \cos \phi + V_2 \cos 2\phi + V_3 \cos 3\phi] \quad \text{Eq. A2. 11}$$

$$E_{middle_bond_torsion} = \sum_{b'} \sum_{\phi} F_{b'\phi} (b' - b'_0) [F_1 \cos \phi + F_2 \cos 2\phi + F_3 \cos 3\phi] \quad \text{Eq. A2. 12}$$

$$E_{angle_torsion} = \sum_{\theta} \sum_{\phi} F_{\theta\phi} (\theta - \theta_0) [V_1 \cos \phi + V_2 \cos 2\phi + V_3 \cos 3\phi] \quad \text{Eq. A2. 13}$$

$$E_{angle_angle_torsion} = \sum_{\phi} \sum_{\theta} \sum_{\theta'} K_{\phi\theta\theta'} \cos \phi (\theta - \theta_0) (\theta' - \theta'_0) \quad \text{Eq. A2. 14}$$

$$E_{Coulomb} = \sum_{i>j} \frac{q_i q_j}{\epsilon r_{ij}} \quad \text{Eq. A2. 15}$$

$$E_{vdW} = \sum_{i>j} \left[\frac{A_{ij}}{r_{ij}^9} - \frac{B_{ij}}{r_{ij}^6} \right] \quad \text{Eq. A2. 16}$$